Optical spectroscopy of wide gap diluted magnetic semiconductors based on ZnO and GaN

Wojciech Pacuski

To cite this version:

Wojciech Pacuski. Optical spectroscopy of wide gap diluted magnetic semiconductors based on ZnO and GaN. Condensed Matter [cond-mat]. Université Joseph-Fourier - Grenoble I, 2007. English. NNT : . tel-00296634

HAL Id: tel-00296634
https://theses.hal.science/tel-00296634
Submitted on 14 Jul 2008

Uniwersytet Warszwski
Université Joseph Fourier - Grenoble 1

Optical spectroscopy of wide gap diluted magnetic semiconductors based on ZnO and GaN

Spektroskopia optyczna szerokoprzerwowych półprzewodników półmagnetycznych na bazie ZnO i GaN

Spectroscopie optique de semi-conducteurs magnétiques dilués à large bande interdite, à base de ZnO et GaN

THÈSE

présentée et soutenue publiquement le 10 décembre 2007

pour l'obtenir les titres

de docteur de l'Université Joseph Fourier - Grenoble 1
et de docteur de l'Université de Varsovie
(spécialité physique)

par

Wojciech Pacuski

Composition du jury

Rapporteurs :	R. Stępniewski C. Testelin
Examinateurs :	W. Bardyszewski D. Scalbert
Directeurs de thèse :	J. Cibert D. Ferrand P. Kossacki

Wydział Fizyki, Zakład Fizyki Ciała Stałego
Institut Néel, équipe CNRS-CEA-UJF "Nanophysique et semiconducteurs"

Mis en page avec la classe thloria.

Acknowledgments

I would like to express my gratitude to my supervisors in Poland : Piotr Kossacki and Jan Gaj, and to my supervisors in France : David Ferrand and Joël Cibert. Their interactions and collaboration made my study pleasant and fruitful. I am grateful for their understanding, patience, continuous support, and encouragement during this work.

This research would not have been possible without the work of all the people involved in the growth of the high quality crystals studied in this work : Christiane Deparis, Christian Morhain, Eirini Sarigiannidou, Henri Mariette, Ekaterina Chikoidze, Yves Dumont, Matthias Wegscheider, Andrea Navarro-Quezada, and Alberta Bonanni.

I thank Pascal Sati, Anatoli Stepanov, Agnieszka Wołoś, and Wolfgang Jantsch for valuable data obtained by the EPR technique and for helpful discussions. I would like to thank also Jean-Michel Chauveau, Marguerite Laügt, and Philippe Vennègués for the structural characterization of the samples.

The work performed in Grenoble was carried out in the CNRS-CEA-UJF-Institut Néel joined group "Nanophysique et semiconducteurs" (NPSC). I thank the members of the group, in particular Le Si Dang, Lucien Besombes, Jean-Philippe Poizat, Serge Tatarenko, and all of the PhD students for providing the friendly atmosphere. Particularly, I would like to thank Stephane Marcet for our good cooperation.

The work performed in Warsaw was carried out in the Division of Solid State Physics, in the Institute of Experimental Physics, Warsaw University. I would like to give my special thanks to members of the DMS group : Michał Nawrocki, Andrzej Golnik, Katarzyna Kowalik, Wiktor Maślana, Jan Suffczyński, Artur Trajnerowicz, and many others.

I wish to acknowledge helpful discussions with Witold Bardyszewski, Tomasz Dietl, Perła Kacman, and Roman Stępniewski, who gave me many hints concerning theoretical aspects of my work.

My warmest acknowledgments go to my wife, Maria, without whose love, encouragement and editing assistance, I would not have finished this thesis.

I should also mention that my studies were partially supported by grant of the French Ministry of Foreign Affairs (program thèse en cotutelle), by the Polish Ministry of Science and Higher Education (project N202 006 31/0153), and by the Foundation For Polish Science (program START).

Warsaw
October 10, 2007

Contents

Chapter 1

Introduction

Diluted magnetic semiconductors (DMS) fascinate researchers by linking properties of semiconductors and magnetic materials. Semiconductors offer the possibility to control properties related to the charge of electrons. They also induce the development of modern electronics. Magnetic ions introduce the challenge of manipulating the spin momentum of electrons. Magnetic ions diluted in semiconductors offer also phenomena such as carrier mediated ferromagnetism. This unique, switchable magnetic ordering has great potential applications in *spintronics* - future electronics based on the spin of carriers not only on their charge.

Carrier mediated ferromagnetism has been demonstrated for several DMS systems : $In_{1-x}Mn_xAs$,[1] $Ga_{1-x}Mn_xAs$,[2] $Zn_{1-x}Mn_xTe$,[3] and $Cd_{1-x}Mn_xTe$ quantum wells.[4] It can be controlled by electric field,[5] light,[6] and strain[7,8] but the problem is that this systems exhibit ferromagnetic properties only at low temperatures. If one wants to use ferromagnetic semiconductors in computers, mobile phones, and in other present or future electronic devices, one needs them working at least at room temperature (RT). Last years, theoretical predictions[9–13] suggested that ZnO and GaN based DMS could exhibit room temperature ferromagnetism under special conditions. This has motivated many groups to study $Ga_{1-x}Mn_xN$, $Zn_{1-x}Mn_xO$, $Zn_{1-x}Co_xO$, and other wide gap DMS. In fact, several reports of room temperature ferromagnetism has been published recently,[14–23] but the nature of magnetic properties remains very controversial. There are strong indications, that the observed ferromagnetism is related to secondary phases rather than to uniform DMS crystal and free carriers.[24–26] Thus technological applications of such materials are still quite far. Doubts are so strong, that at 125 anniversary of Science magazine,[27] editors have joined a related question to list of 125 top questions of present science : *Is it possible to create magnetic semiconductors that work at room temperature ?*

In our opinion, the answer to the question about RT ferromagnetism cannot be given by a simple search for samples showing some kind of magnetic ordering. This was a first try of many experimental groups, but even if room temperature ferromagnetism is found, it is difficult to be convinced, that it is really driven by free carriers, and to exclude phase segregation. Reliable answer cannot be also given by theory. It needs precise parameters, which are not available yet, to meet real experimental situation. The only choice seems to do a systematic, fundamental study, which takes into account broad aspects of physical phenomena and explains basic properties of main candidates for RT ferromagnetism. In particular, it is important to understand the interaction between carriers and magnetic ions.

A crucial contribution to an explanation of the basic properties of DMS materials is given by magnetooptical spectroscopy. It brings information on *s*-*d* and *p*-*d* (or shortly : *s*,*p*-*d*) exchange interactions, which are fundamental for any DMS. *s*,*p*-*d* is a coupling between the *s*-like function in the conduction band, the *p*-like function in the valence band and the *d*-shell of magnetic ions. These interactions are at the origin of carrier mediated ferromagnetism, and magnetooptical phenomena like the excitonic giant Zeeman splitting or giant Faraday rotation. These magnetooptical phenomena can be described[28] using the molecular field (MFA[29]) and virtual crystal approximations (VCA[30]) : an ordering of the magnetic ions induces the exchange splitting of the conduction and valence bands ; the splitting is proportional to the magnetization and to *s*,*p*-*d* exchange integrals. In ferromagnetic DMS, we can also observe this interaction acting in the opposite direction : polarized carriers are able to induce a magnetic ordering.

Thanks to exchange splitting, magnetooptical spectroscopy allows us to study the intrinsic magnetism and to discriminate any signal related to secondary phases. Moreover, if a direct observation of excitons is possible, the excitonic giant Zeeman splitting allows us to estimate the strength of ion-carrier interactions. This has been successfully realized for many II-VI DMSs, where magnetic ions are electrically neutral, so that excitons are not perturbed by a high concentration of free carriers. Usually, in III-V DMSs, magnetic ions introduce free carriers, and consequently the interpretation of magnetooptical spectra is much more difficult.

A determination of the effect of *p*-*d* coupling allows one to conclude about the conditions supporting carrier mediated ferromagnetism. Therefore, it is natural that wide gap DMSs - a main candidates for RT ferromagnetism - should be carefully examined using magnetooptical methods. This is the main motivation of this work. Additionally, we will show that specific properties of the wide gap DMSs make them worth to be studied even if those materials cannot really serve in spintronics applications.

Several properties of wide gap diluted magnetic semiconductors, (DMSs based on ZnO and GaN) differ from typical II-VI or III-V materials. First, the large width of the band gap shifts excitonic optical transitions to the UV region of the spectra, but also affects the *p*-*d* interaction and the charge state of the magnetic ions. It is possible to introduce magnetic ions into GaN as neutral centers substituting Ga cations, although GaN is a III-V compound. We will show, that this makes $\mathrm{Ga}_{1-x}\mathrm{Mn}_x\mathrm{N}$ more similar to II-VI compounds, than to $\mathrm{Ga}_{1-x}\mathrm{Mn}_x\mathrm{As}$ (a typical III-V DMS). For example, a direct observation of the excitonic giant Zeeman splitting, like in II-VI, is possible in $\mathrm{Ga}_{1-x}\mathrm{Mn}_x\mathrm{N}$, but it is very difficult in $\mathrm{Ga}_{1-x}\mathrm{Mn}_x\mathrm{As}$. Second, the small lattice parameters of wide gap materials are expected to strongly increase the hybridization energy. In consequence, one expects also an increase of the strength of the *p*-*d* exchange interaction. This increase was seen as an origin of RT ferromagnetism in this materials, but it could also lead to very new phenomena in the valence band. In particular, it is not evident if the model based on the virtual crystal approximation, developed for the description of the giant Zeeman splitting in the valence band of typical II-VI DMS, can be directly applied to the valence band of wide gap DMS.[9] VCA already breaks in the description of $Cd_{1-x}Mn_xS$,[31–33] which has a smaller lattice parameter when compared to $Cd_{1-x}Mn_xTe$ (a typical II-VI DMS). Wide gap DMSs have a lattice parameter much smaller than both of these materials. Moreover, a strong electron-hole interaction and a weak spin-orbit coupling lead to significant excitonic effects, which were negligible in DMSs with a narrow gap. Finally, wide gap DMSs exhibit a large magnetic and optical anisotropy due to the trigonal crystal field. All these reasons show that a magneto-optical study of wide gap DMSs can make an interesting contribution to the physics of DMS materials.

Additionally, introducing magnetic ions into ZnO and GaN is interesting for the spectroscopy of wide gap semiconductors. The direct influence of a magnetic field on excitons in ZnO and GaN is very weak, but introducing magnetic ions increases the excitonic g-factors by several orders of magnitude. This means, that the splitting observed so far only at very high magnetic field, can be studied using a standard magnetooptical setup. It brings a hope of understating fundamental properties of excitons in ZnO, such as the valence band symmetry and excitonic mixing.

This thesis presents the results of a low-temperature magnetooptical study conducted on a set of $Zn_{1-x}Co_xO$, $Zn_{1-x}Mn_xO$, $Ga_{1-x}Mn_xN$, and $Ga_{1-x}Fe_xN$ layers with various concentrations of magnetic ions x. For each material, we have found samples which feature well resolved excitonic lines, so that we can measure the exchange Zeeman splitting.[34–40] Our work fills the gap existing between magneto-absorption studies of layers with a high magnetic ion content ($Zn_{1-x}Co_xO$,[21,24,41–45] $Zn_{1-x}Mn_xO$,[41] and $Ga_{1-x}Mn_xN$[46,47]), where large linewidths prevent a direct observation of the exchange Zeeman splitting, and studies of very diluted samples where authors focus on intra-ionic transitions in the infrared ($Zn_{1-x}Co_xO$,[48–51] $Ga_{1-x}Mn_xN$,[47,52] and $Ga_{1-x}Fe_xN$[53,54]). Probably, in this study excitonic splitting was too small to be observed, due to a low concentration of magnetic ions. In the case of $Zn_{1-x}Co_xO$, previous optical studies of the intra-ionic d-d transitions have been done without applied magnetic field. As a result, the opportunity to report on the behavior of Co^{2+} in ZnO at high magnetic fields has been left for us.

During the preparation of this work (years 2002-2007), many groups were studying our samples or other samples of wide gap DMS by magnetometry, EPR, and x-ray spectroscopy. This allows us to compare and discuss various results.

In my opinion, there are two important outputs from this work. First, it gives a detailed description of the complex magnetooptical phenomena characteristic for wide gap DMS. Second, our optical experiments lead to surprising conclusions verifying main stream theories. In wide gap DMS, the effect of s,p-d exchange interactions on excitons and carriers is strongly reduced instead of being enhanced. Moreover, sign of the splitting cannot be explained using standard description of DMS. This suggests that p-d coupling in wide gap DMS is in a strong coupling regime.[55] Therefore models based on effective medium[9,11,12,56] cannot be used any more for the simulation of high temperature ferromagnetism in DMS. On the other hand, our results confirm very recent non-perturbative approaches[55,57,58] describing ferromagnetic DMS.

Chapter 2

Samples and experimental setups

This chapter presents the growth and characterization of our samples, and technical details of our experimental setups. We start by a description of the basics of epitaxy. Next, we present the structure of a typical sample and detailed information on the growth and characterization of 5 sets of samples. Finally, we show the experimental setups used for measurements of reflectivity, transmission, photoluminescence, and magnetic circular dichroism signals.

Dans ce chapitre, la croissance, la caractérisation des échantillons et les détails techniques des montages expérimentaux sont présentés. Premièrement, nous expliquons l'essentiel de l'épitaxie. Deuxièmement, nous présentons la structure d'un échantillon typique. Des informations plus détaillées sur la croissance et sur la caractérisation de 5 séries d'échantillons sont également présentées. Finalement, nous présentons les montages expérimentaux employés afin de mesurer la réflectivité, la transmission, la photoluminescence et les signaux de dichroïsme magnétique circulaire.

2.1 Growth

The growth of our samples has been realized using epitaxial techniques, MBE and MOVPE (or MOCVD). The term epitaxy originates from Greek : *epi* means "above" and *taxis* means "in an ordered manner". The word **epitaxy** is used to describe an ordered crystalline growth on a monocrystalline substrate. **MBE (molecular beam epitaxy)** is a technique of growth which takes place in high vacuum (pressure below 10^{-7} torr) or ultra high vacuum (about 10^{-11} torr), with a very slow deposition rate.[59] In our case, the rate is about 0.5 μm per hour. High vacuum is required to avoid the reaction of molecules of the beam with the gases in the growth chamber, and to keep low contaminant concentrations in the layer. **Metalorganic vapour phase epitaxy (MOVPE)** is a chemical vapour deposition method of epitaxial growth from the surface reaction of organic compounds or metalorganics and metal hydrides containing the required chemical elements. An alternative name for this process is metalorganic chemical vapour deposition (MOCVD).[59] Nevertheless, we use names suggested by growers of samples. In MOVPE or MOCVD, the formation of the epitaxial layer occurs by final pyrolysis of the metalorganic precursors at the substrate surface. In contrast to MBE, the growth of crystals is by chemical reaction and not a physical deposition. This takes place not in the vacuum, but from the gas phase at moderate pressures (typically at about 1 torr).

All our samples are thin layers grown on sapphire substrates. The thickness of our layers varies from 0.1 μm up to 2 μm. Layers are wide gap semiconductors : ZnO (zinc oxide) or GaN (gallium nitride), with a part of cations replaced by magnetic ions : Mn (manganese), Fe (iron), or Co (cobalt). Such a material is called a DMS (diluted magnetic semiconductor). Between the main layer and the sapphire substrate, a buffer layer was formed, which does not contain any magnetic ions. This buffer layer was not interesting for us, but it affects optical spectra of the sample. Therefore, we used as thin as possible buffer layers, or buffer layers transparent in spectral region of excitons in ZnO and GaN. The sapphire substrate is oriented along the (0001) direction, which induces a growth of ZnO and GaN with the crystallographic c-axis parallel to the growth direction. The scheme of a typical sample is shown in Fig. 2.1.

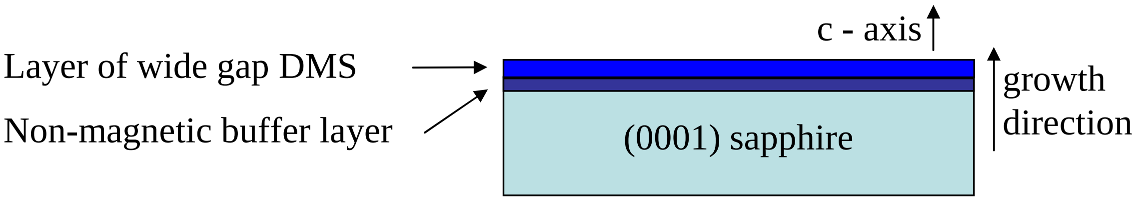

Figure 2.1: Scheme of the samples investigated in this work. From bottom to top, there is a sapphire substrate oriented along the (0001) direction, then a buffer layer made from wide gap semiconductor without magnetic ions (ZnO, GaN or AlN), and then main layer of wide gap DMS : $Zn_{1-x}Co_xO$, $Zn_{1-x}Mn_xO$, $Ga_{1-x}Mn_xN$, or $Ga_{1-x}Fe_xN$. The c-axis of the wurtzite crystal is parallel to the growth direction.

2.2 Characterization

Structural properties

Introducing magnetic ions into ZnO and GaN leads to a significant lowering of the crystal quality. Several characterization techniques were helpful in choosing optimal growth conditions and for selection of samples for a magnetooptical study. *In situ* monitoring of the growth surface was possible during the MBE process thanks to **RHEED (reflection high-energy electron diffraction)**. A typical RHEED system contains an electron gun producing about 10 keV beam aimed at a very large angle of incidence to the substrate surface.[59] The reflected electron diffraction pattern is displayed on a phosphor screen. Post-growth characterization of the surface and cleavage plane was realized using various types of microscopy : standard optical microscopy, scanning electron microscopy (SEM), atomic force microscopy (AFM), scanning tunneling microscopy (STM), transmission electron microscopy (TEM).

Particularly helpful was SEM, which allows our coworkers to perform a very precise determination of the sample thickness, when they studied the image of a cleavage plane. AFM and TEM have been employed in order to study the surface morphology and to detect very small inhomogeneities. The presence of larger secondary phases, homogeneity and changes of lattice constants were studied using **XRD (X-ray diffraction)**

Concentration of magnetic ions

The following techniques were used in order to get the concentration of magnetic ions : SIMS, EDX, infrared absorption, EPR, and SQUID. Below, we introduce them shortly.

SIMS means **secondary ion mass spectrometry**. In this technique, atoms from a high energy primary ion beam are impinging the sample and a secondary beam of particles is ejected from the sample and analyzed by a mass spectrometer. This technique is very sensitive even for very low concentrations of magnetic ions (ppb-range). Moreover, it allows to measure the distribution of magnetic ion concentration in depth, which is not accessible for other commonly used techniques. It brings also information about the thickness of the sample. Unfortunately, SIMS destroys a small part of the sample, so it should be used rather after, than before optical measurements. A risk of using SIMS is related to the small spot tested by this technique. Thus, if the sample has an inhomogeneous surface, one can measure a point with a concentration of magnetic ions very different from average. In order to avoid this problem, we took photographs of samples, and then we tried to use SIMS exactly at the point which was studied by reflectivity or PL.

EDX or **EDS** means **energy dispersive x-ray analysis (or spectroscopy)**. This technique is nondestructive and it is commonly accessible in growth laboratories. Comparing to SIMS, its sensitivity is lower and it is usually limited to $x > 0.5\%$.

An important property of EDX and SIMS is that they bring information on the total concentration of interesting element. They do not distinguish between magnetic ions with different charge states or ions in pairs or complexes. In order to determine the concentration of magnetic ions with a particular charge state, we used other techniques. Co^{2+} and Mn^{3+} exhibit sharp absorption lines in the infrared. We will show in Chapter 3, how we do conclude about the concentration of Co^{2+} and Mn^{3+} by measuring the intensity of intra-ionic absorption lines. **EPR** (**electron paramagnetic resonance**) is also sensitive to a particular configuration of magnetic ions : in our case, it is d^5 or d^7, so it can be used to observe Mn^{2+}, Fe^{3+}, and Co^{2+}.

Finally, **SQUID** (**superconducting quantum interference device**) brings another important information : magnetization, which can be translated into an effective concentration of magnetic ions x_{eff}. This value is smaller than x, because x_{eff} does not take into account ions with magnetic moments canceled due to antiferromagnetic interactions.The quantity x_{eff} will be discussed in Sec. 3.6.2. SQUID measurements were the most important in studies of many DMS, but in our case they are very difficult to use. It is because our DMS layers are diluted and thin (order of 1 μm), and because they are placed on thick (about 0.5 mm) substrates. Therefore the total signal of the DMS layer is weak comparing to other contributions. Using the temperature and magnetic field dependence, we can eventually distinguish between the diamagnetic signal of the substrate and the signal of the DMS layer, but we cannot distinguish between our paramagnetic ions in DMS layer and non-intentionally doped paramagnetic impurities in the substrate. Because of the ratio between the thickness of the substrate and DMS layer, even if concentration of paramagnetic impurities is 10^3 lower than the concentration of magnetic ions in DMS layer, both magnetic contribution are comparable.

2.3 Materials

Magnetooptical study described in this work was performed on 5 sets of samples : MBE $Zn_{1-x}Co_xO$, MBE $Zn_{1-x}Mn_xO$, MOCVD $Zn_{1-x}Mn_xO$, MBE $Ga_{1-x}Mn_xN$, and MOVPE $Ga_{1-x}Fe_xN$. In this section, we present the information, received from the different laboratories, where our samples have been grown.

2.3.1 MBE $Zn_{1-x}Co_xO$

About 1μm-thick layers were grown by Christiane Deparis and Christian Morhain from Centre de Recherches sur l'Hétéroépitaxie et ses Applications in Valbonne, France. They used plasma-assisted molecular beam epitaxy. Two dimensional growth was achieved for a growth temperature of 560°C (i.e., 50°C higher than the optimal growth temperature used for ZnO), resulting in streaky RHEED patterns. The Co content of several layers was measured by energy dispersive x-ray analysis (EDX). For low Co contents ($x < 1\%$), the full widths at half maximum of the x-ray rocking curves are in the range of $\omega \sim 0.15°$ along (002), ($\bar{1}05$), and (105). The low, identical values of ω measured both for ($\bar{1}05$) and (105), indicate a large column diameter, close to 1μm (up to $x = 15\%$). While the column diameters remain large, ω values are found to increase slightly and gradually with the Co concentration. For $x = 15\%$, measured ω values are 0.32°, 0.22°, and 0.66° along (002), ($\bar{1}05$), and (101) respectively. For all compositions, the c-axis of the wurtzite structure is perpendicular to the film plane. No other orientation or column rotation were detected. The conductivity of the films is n-type, with residual carrier concentrations $n_e < 1.10^{18}$ cm^{-3}, below Mott transition. The thickness of the layer was checked on the electron microscope image of a cleavage plane. The thickness of the ZnO buffer layer was in the range 20-50 nm.

2.3.2 MBE $Zn_{1-x}Mn_xO$

Growth of $Zn_{1-x}Mn_xO$ layers is a continuation of the work of C. Deparis and C. Morhain described above (Sec. 2.3.1). We have no detailed information on complementary characterization of the new set of samples, except of SIMS results, which brought information about Mn concentration. We will show in Chapter. 5, that at least optical spectra of MBE $Zn_{1-x}Mn_xO$ samples are very similar to those of $Zn_{1-x}Co_xO$. A small increase of the optical quality of the crystal was observed in case of $Zn_{1-x}Mn_xO$.

2.3.3 MOCVD $Zn_{1-x}Mn_xO$

This set of $Zn_{1-x}Mn_xO$ layers were grown by Ekaterina Chikoidze and Yves Dumont from Groupe d'Etude de la Matière Condensée, Meudon, Fance. The growth has been preformed[60] in a vertical geometry MOCVD reactor, with RF heater and thermalized walls (20°C). The chemical composition of the samples (Zn and Mn content) were determined by energy dispersive x-ray spectroscopy on the K and L lines and by SIMS. The surface morphology and the thickness of the grown layers have been assessed by scanning electron microscopy (SEM). The purity of the phase was checked with a standard x-ray diffractometer, while the crystal orientation and the crystallinity of the films deposited on *c*-sapphire were investigated by high resolution x-ray diffractometer (HRXRD). This set of samples, has been grown without any buffer layer. Fig. 2.2 presents the dependence of the cation-cation distance d_c on the Mn concentration x. The linear dependence up to $x = 0.4$ indicates a proper incorporation of Mn ions in the Zn sublattice.

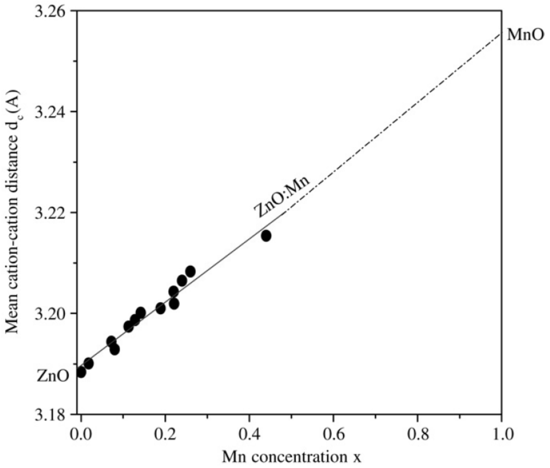

Figure 2.2: Chikoidze *et al.*, Ref. 60. Mean cation-cation distance d as function of Mn mole fraction x for $Zn_{1-x}Mn_xO$. The line is guide for the eyes. The interpolation to a hypothetical MnO wurtzite compound is shown in dashed lines.

2.3.4 MBE $Ga_{1-x}Mn_xN$

$Ga_{1-x}Mn_xN$ layers of about 400 nm thick were grown by Eirini Sarigiannidou and Henri Mariette from our group in Grenoble, France. They used two kinds of buffer layers : GaN and AlN. Details on the growth can be found in Ref. 61. Layers grown with a GaN buffer allowed Marcet *et al.*[47] to study quantitatively the infrared absorption identified in quasi-bulk crystals as due to Mn^{3+} (d^4 ion configuration).[52] These layers exhibit[47] magnetic circular dichroism (MCD) at the band gap energy,[46] ascribed to the ion-carrier coupling. Layers with a higher Mn content evidence a ferromagnetic behavior at low temperature.[61]

The present $Ga_{1\text{-}x}Mn_xN$ layers have been grown on a buffer layer made of thin AlN (few nm), which has a large energy gap (E_g over 6 eV), so that the excitonic spectra of $Ga_{1\text{-}x}Mn_xN$ (E_g about 3.5 eV) are not entangled with those of the buffer layer. However, layers with the AlN buffer have a significant lattice mismatch, which introduces strain and disorder, and consequently increases the excitonic linewidth. As disorder increases also with the Mn content, we focused our study onto rather dilute samples ($x < 1.2\%$) exhibiting well-resolved excitons.

The concentration of Mn^{3+} has been determined using SIMS and confirmed using infrared spectroscopy. We observe sharp absorption lines previously reported[47,52] as intra-ionic ${}^5T_2 \rightarrow {}^5E$ transitions of Mn^{3+}. We will show this absorption in Sec. 3.3. Furthermore, three of the most important samples were characterized using EPR, by P. Sati and A. Stepanov from Laboratoire Matériaux et Microélectronique de Provence, Marseille, France. From the absence of characteristic lines in EPR spectra, our coworkers deduced that the Mn^{2+} concentration is lower than 0.01%.

2.3.5 MOVPE $Ga_{1-x}Fe_xN$

The $Ga_{1\text{-}x}Fe_xN$ samples were grown by Andrea Navarro-Quezada, Matthias Wegsheider, and Alberta Bonnani from Institute for Semiconductor and Solid State Physics, Johannes Kepler University, Linz, Austria. They used metalorganic vapor phase epitaxy (MOVPE). Details of growth are given in Ref. 62. The 0.7 μm thick layers of $Ga_{1\text{-}x}Fe_xN$ were grown on [0001] sapphire substrates with a 1 μm thick, wide-band gap $Ga_{1-x}Al_xN$ buffer layer, which is transparent in the free exciton region of $Ga_{1\text{-}x}Fe_xN$. The Fe flow rate was adjusted to keep the Fe content well below 0.4%, which is the solubility limit of Fe in GaN under our growth conditions. According to detailed luminescence, electron paramagnetic resonance, and magnetic susceptibility studies,[62] in this range the Fe ions take mostly the expected Fe^{3+} charge state corresponding to the d^5 configuration, for which the spin polarization as a function of temperature T and magnetic field B is determined by the Brillouin function $\mathrm{B}_S(T, B)$ with spin $S = 5/2$ and Landé factor $g_{Fe^{3+}} = 2.0$. This is confirmed by our magnetooptical data to be shown in Sec. 5.5.2 (Fig. 5.32), which scale with $\mathrm{B}_{5/2}(T, B)$.

The concentration of Fe^{3+} was determined from magnetization measurements by Michał Kiecana and Maciej Sawicki from Institute of Physics, Polish Academy of Sciences, Warsaw, Poland. This determination was possible, although the signal of the magnetic layer was one order of magnitude weaker than the diamagnetic signal from the substrate. They overcame this problem using the temperature dependence, which is very strong for paramagnetic Fe^{3+}, but it is negligible for the diamagnetic substrate and eventual ferromagnetic precipitates. Magnetization curves were measured for $T = 1.8$ K and $T = 5$ K. The difference between these two signals is well described using the difference between Brillouin functions calculated at 1.8 and 5 K. As a result of fitting, our coworkers obtained one parameter for each sample - the concentration of paramagnetic Fe^{3+}. Experimental data and fitted curves are shown in Fig. 2.3.

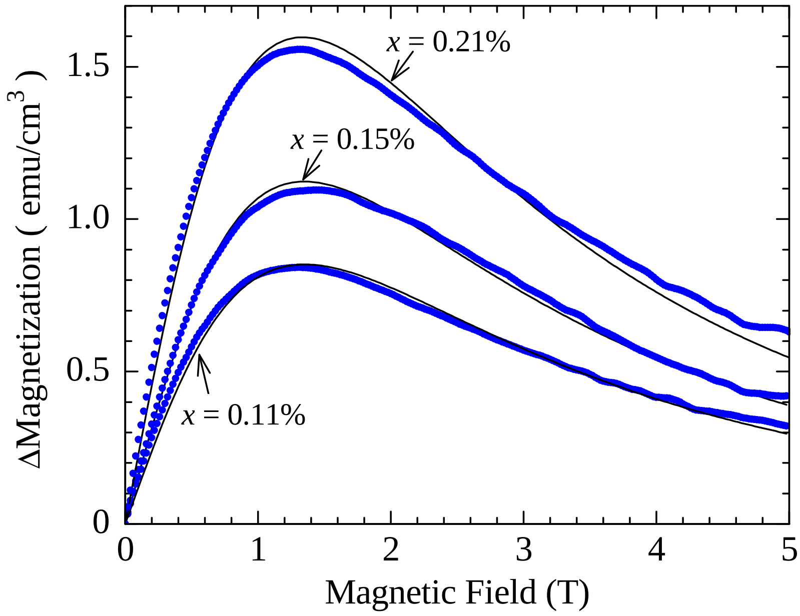

Figure 2.3: Experimental data of M. Kiecana and M. Sawicki, Ref. 36. Difference between magnetization at 1.8 K and 5 K (points) and theoretical difference between Brillouin function calculated for 1.8 K and 5 K. There is only one fitting parameter for each curve - effective concentration of Fe. Samples : ♯588 ($x = 0.11\%$), ♯647 ($x = 0.15\%$), and ♯589 ($x = 0.21\%$).

2.4 Experimental setups

We used two almost equivalent optical experimental setups : in Grenoble, at Joseph Fourier University, and in Warsaw, at Faculty of Physics Warsaw University. The main difference was related to the fact that the cryostat in Warsaw has four optical windows and split-coil magnet, which allowed measurements in various configurations. The magnetic field up to 7 T was applied in horizontal direction. Cryostat in Grenoble had only one window, but magnetic field could be applied up to 11 T. The optical axis and the direction of magnetic field in this cryostat were vertical. A mirror below the cryostat made this configuration very similar to the configuration in horizontal plane. We were able to control the temperature in range 1.5 K (superfluid helium) - 300 K (gas helium). The temperature was measured using calibrated resistor placed near the sample.

2.4.1 Reflectivity in Faraday configuration

Fig. 2.4 shows the experimental setup for reflectivity measurements in the Faraday configuration. Reflectivity was measured with normal incidence. The detection was resolved in circular polarizations. In Warsaw, we used an achromatic quarter waveplate (IR, VIS, UV range), in Grenoble we used a Babinet-Soleil compensator. They were followed by calcite Glan-Taylor linear polarizer. The σ^+ and σ^- circular polarizations were defined with respect to the direction of a positive applied field. We reversed the sign of the circular polarization sweeping the magnetic field from positive to negative values, or rotating the waveplate by angle of 90 degree. We calibrated sign of circular polarization by measuring giant Zeeman effect in $Cd_{1-x}Mn_xTe$, where heavy hole exciton shifts to low energy in σ^+ circular polarization.[28,63] Reliable calibration of the helicity was crucial for this work, because it allowed us to determine sign of exchange integrals. We used a high pressure Xe arc lamp. A blue filter just behind the lamp is important for the protection of the rest of experimental setup from heating by light in the IR and VIS range of the spectra. In Warsaw we used an aqueous solution of copper sulphide as a blue filter, in Grenoble light was guided by an optical fiber optimized for transmission of blue and UV range of spectrum.

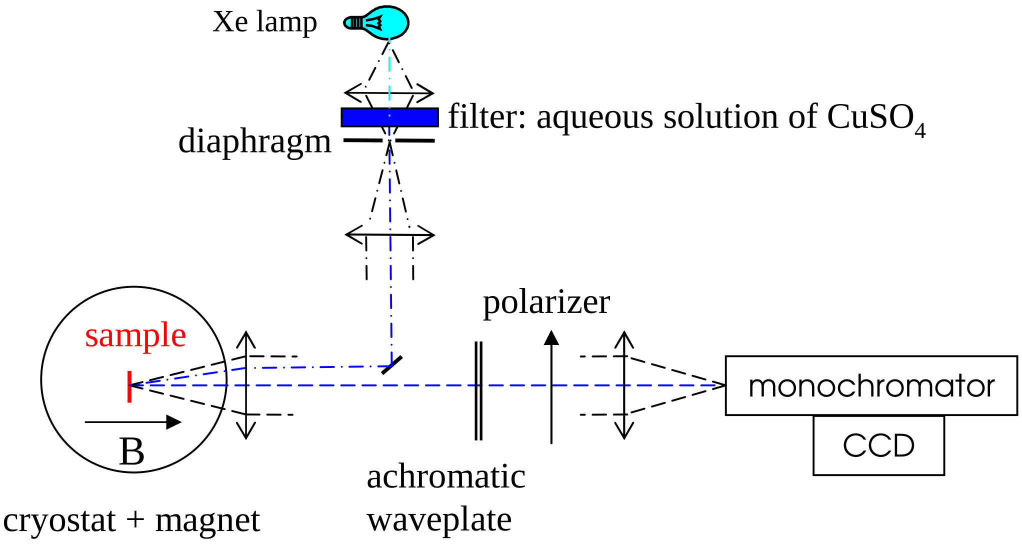

Figure 2.4: Experimental setup for reflectivity measurements with normal incidence.

2.4.2 Reflectivity with 45 degree incidence

Fig. 2.5 shows the experimental setup for reflectivity measurements with an incidence of 45 degree. The detection is resolved in linear polarizations. Vertical polarization brings almost the same information as reflectivity with normal incidence, because $E \perp c$-axis (σ polarization). More interesting is the horizontal linear polarization, which is a mixture of π ($E \parallel c$-axis) and σ. We do not apply a magnetic field, because it would be very difficult to interpret the data obtained in this configuration. This configuration was used only in Warsaw.

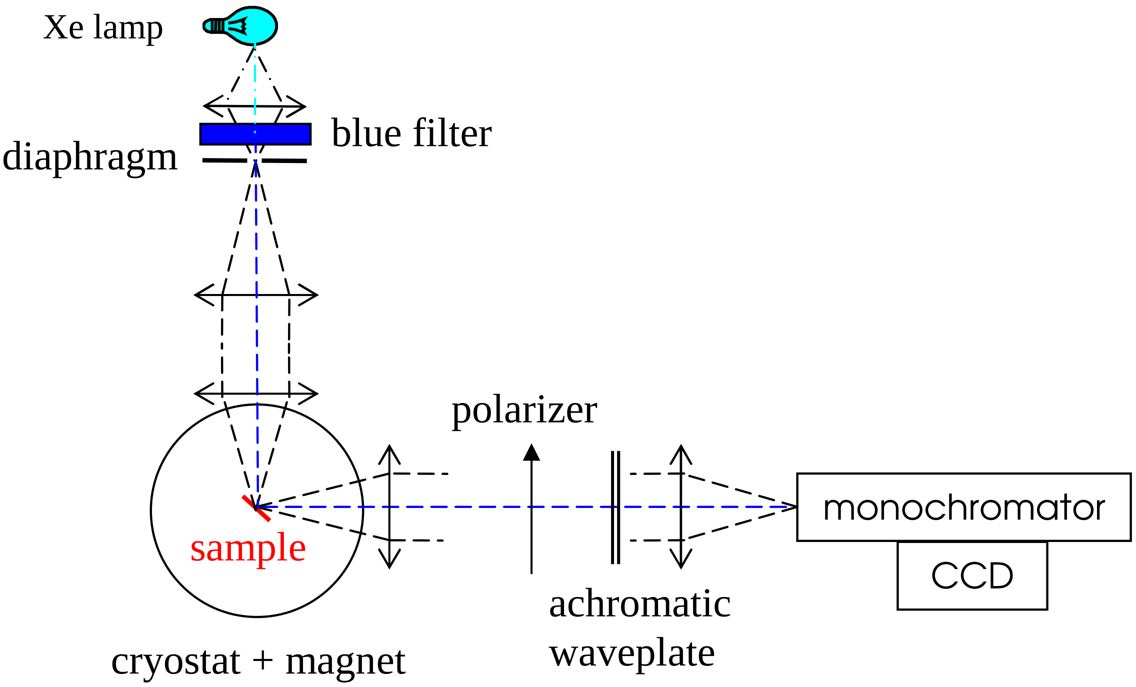

Figure 2.5: Experimental setup for reflectivity measurements with 45 degree incidence. There is zero magnetic field. Linear polarizations : vertical and horizontal are measured.

2.4.3 Photoluminescence in Faraday configuration

The configuration for photoluminescence measurements (Fig. 2.6) was very similar to that for reflectivity. In order to eliminate fluorescence lines from the laser, a fused silica prism and about 3 m distant diaphragm was often used. PL measurements were realized in two spectral ranges : UV and IR. Both : achromatic waveplate (in Warsaw) and Babinet-Soleil (in Grenoble) allow a quick change of the spectral range.

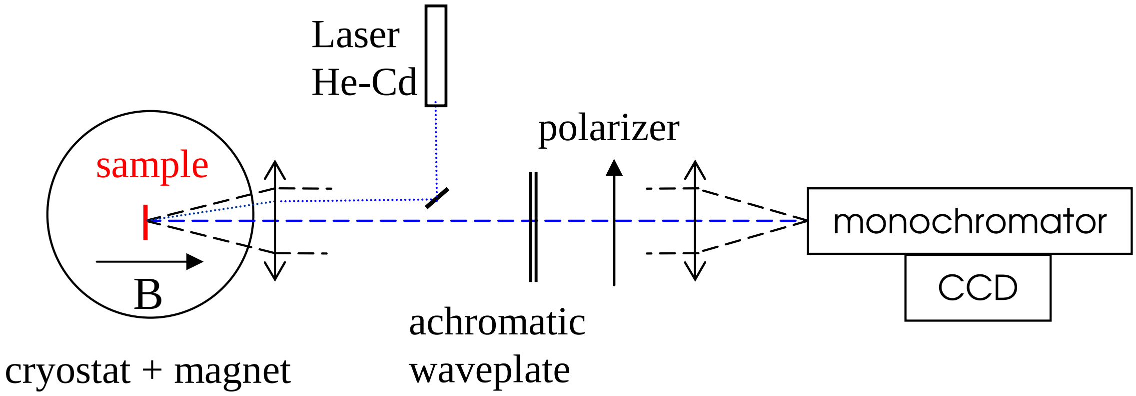

Figure 2.6: Experimental setup for photoluminescence measurements.

2.4.4 Transmission in Faraday configuration

The experimental setup for transmission measurements in the Faraday configuration was very similar to the one used for reflectivity. Fig. 2.7 shows the scheme of the practical realization in Warsaw. In Grenoble, the light from a lamp was guided to the sample by an optical fiber, as it is shown in case of configuration for MCD measurements. Two kinds of lamps were used in transmission : high pressure Xe lamp for UV, and halogen lamp for VIS/IR. Just behind the high pressure Xe lamp, we used a blue filter. Behind the halogen lamp, we used a filter absorbing IR, e.g., water.

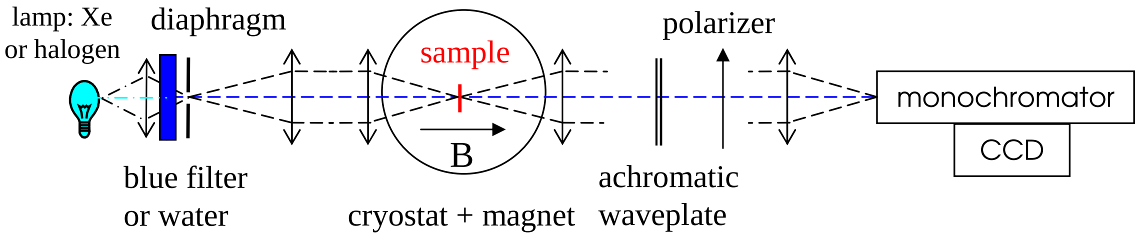

Figure 2.7: Experimental setup for transmission measurements.

2.4.5 Magnetic Circular Dichroism

We used a photo-elastic modulator, a photo-multiplier and synchronized detection in order to measure very weak differences between absorption in σ^+ and σ^- circular polarizations. We used this experimental setup only in Grenoble, in the configuration shown in Fig. 2.8. Despite the vertical magnetic field, this is a classical Faraday configuration. We used either Xe lamp either halogen lamp, depending on spectral range of interest.

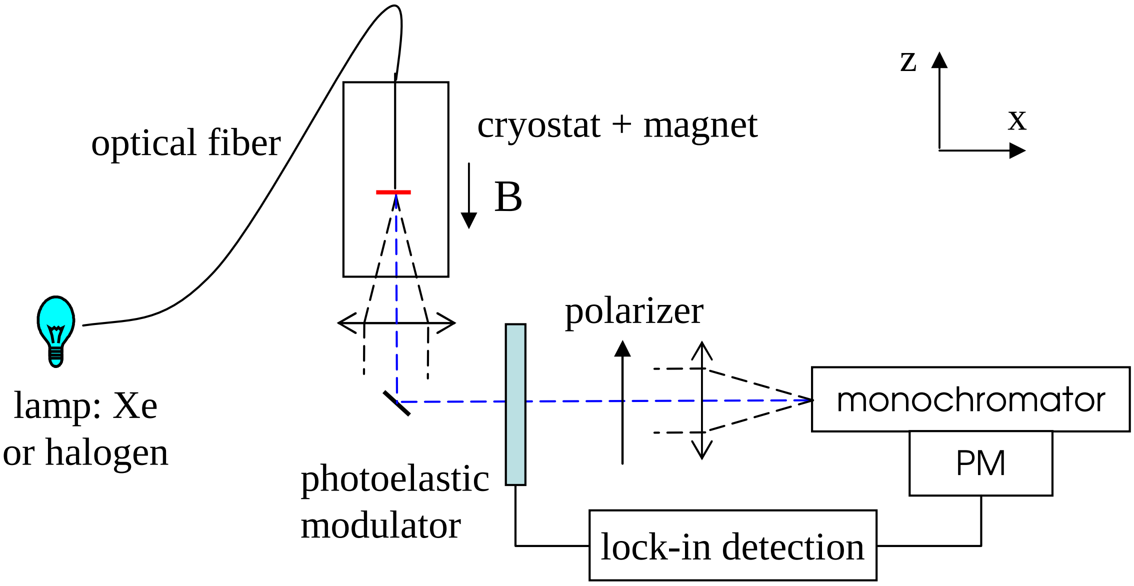

Figure 2.8: Experimental setup for measurements of magnetic circular dichroism.

Chapter 3

Optical transitions of magnetic ions

This chapter presents the infrared spectroscopy involving optical transitions within the d-shell of the magnetic ions. We present a detailed analysis of magneto-photoluminescence and magneto-absorption of Co^{2+}*. We present also the absorption of* Mn^{2+} *in ZnO and* Mn^{3+} *in GaN, and photoluminescence of* Mn^{3+} *and* Fe^{3+} *in GaN. Optical spectroscopy together with reported EPR measurements are used to describe the Zeeman effect of magnetic ions and to calculate magnetization curves.*

Dans ce chapitre, nous présentons la spectroscopie infrarouge associée aux transitions optiques liées a l'excitation de la couche d des ions magnétiques. Nous montrons une analyse détaillée de la photoluminescence et de l'absorption sous champ magnétique des ions Co^{2+}*. Nous analysons ensuite l'absorption de* Mn^{3+} *dans ZnO, de* Mn^{3+} *dans GaN et la luminescence de* Mn^{3+} *et de* Fe^{3+} *dans GaN. Les paramètres déduits de cette étude de spectroscopie optique sont en accord avec les résultats des études de RPE ; nous les employons pour calculer l'effet Zeeman des ions magnétiques et les courbes d'aimantation.*

3.1 Introduction

Since wide gap semiconductors are almost transparent in the infrared and visible range, they are excellent hosts for optical study of the electronic structure of transition metals. Intra-ionic optical transitions of Co, Ni, Cu or Fe embedded in ZnO matrix has been studied since the sixties,[48–50,64,65] so well before year 2000, when theoretical predictions of room temperature ferromagnetism[10–13] focused the interest on ZnO and GaN as hosts materials for diluted magnetic semiconductors. Nowadays, we are particularly interested in magnetism and ion-carrier coupling in wide gap DMS. Thus, we extended the zero-field study[48–51] of Co^{2+} in ZnO to magneto-absorption and magneto-photoluminescence, which allows us to quantify the magnetic anisotropy of isolated Co^{2+} in our samples. Similarly, we extended the zero-field photoluminescence[47] of Mn^{3+} to magneto-photoluminescence. Magneto-absorption of Mn^{3+} has been recently reported.[47,52] Infrared spectroscopy helps us also to determine the charge state and concentration of magnetic ions in our samples.

The zero-field splitting and the resulting anisotropy of magnetic ions have been observed and described for many wurtzite (e.g. $Cd_{1-x}Co_xSe$[66–68]) and zinc blende (e.g. $Cd_{1-x}Fe_xTe$[69,70]) II-VI DMS. We will show that these effects are particularly important for understanding of the magnetization in wide gap DMS. From the studies of classical II-VI DMS, we learned also that one should distinguish the properties of single magnetic ions, and ions, which have one or more neighboring magnetic ion.[71] It is because of antiferromagnetic ion-ion (d-d) interactions. At the end of the present chapter, we will discuss the magnetic properties of various electronic configurations of magnetic ions in semiconductors with wurtzite structure. There, we will show that the number of electrons on the d shell of magnetic ion is crucial for the magnetic properties.

3.2 Absorption and photoluminescence of Co^{2+} in ZnO

We measured the characteristic absorption lines and bands in every studied $Zn_{1-x}Co_xO$ sample from the most diluted one ($x = 0.1\%$) up to the most concentrated one ($x = 35\%$). Examples are given in Figs 3.1(a) and 3.2(a) for the spectral range of interest. These lines and bands have been already identified as intra-ionic d-d transitions of cobalt in bulk samples by Koidl.[48] For substitutional Co ions, the different eigenstates associated to the $3d^7$ configuration are labeled using the notation of Macfarlane.[64,72]

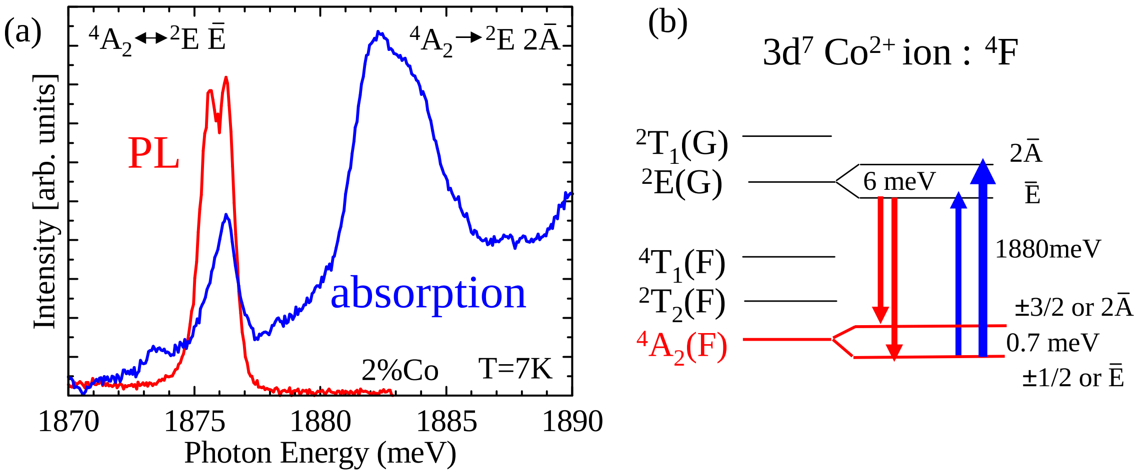

Figure 3.1: (a) Absorption and photoluminescence (PL) associated with the intra-ionic transition between the $^4A_2$ ground state and ^2E excited state in a $Zn_{1-x}Co_xO$ epilayer with 2% Co. (b) Schematic energy levels of the Co^{2+} ions after the perturbation of the crystal field and of the spin orbit coupling. The fine structure indicated for the $^4A_2$ and ^2E states are in well agreement with the experimental spectra shown in (a). Sample ♯Z219c.

We will particularly study the transitions between the $^4A_2$ ground state and the ^2E excited state (see Fig. 3.1(b)) arising from the cubic part of the crystal field.

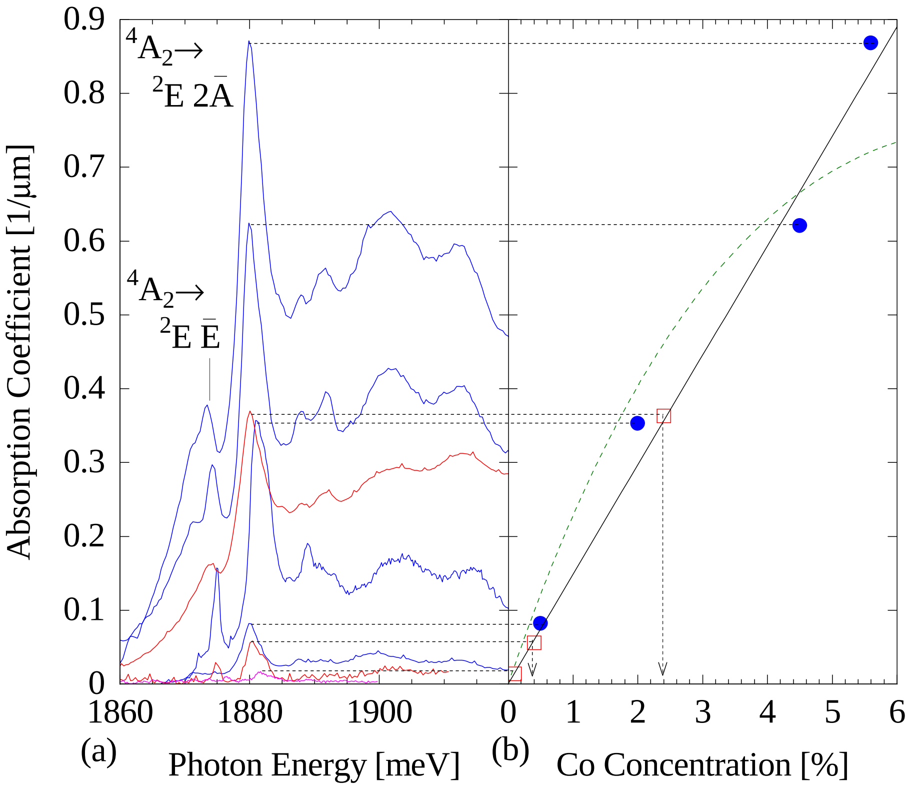

Figure 3.2: (a) Absorption spectra of Co^{2+} in Zn$_{1-x}$Co$_x$O samples with various cobalt concentration x, at $T = 1.6$ K. Two zero-phonon intra-ionic transitions are identified : $^4A_2 \rightarrow {}^2E\ \bar{E}$ (at 1875 meV) and $^4A_2 \rightarrow {}^2E\ 2\bar{A}$ (at 1880 meV). The absorption coefficient of the $^4A_2 \rightarrow {}^2E\ 2\bar{A}$ transition is shown by a dotted horizontal line pointing to the right figure. (b) The absorption coefficient at 1880 meV, as a function of the Co concentration determined by EDX (full circles). The observed linear dependence allows us to determine also the Co concentration in very diluted samples (open squares and vertical arrows), where the EDX technique is not sensitive enough. The dashed curve represents hypothetical dependence of absorption on the concentration of isolated Co ions $x(1-x)^{12}$. This curve does not describe properly experimental data.

Both quadruplets are further split into two components (two Kramers doublets), $2\bar{A}$ and $\bar{E}$, by the spin-orbit coupling and the trigonal component of the crystal field. For the $^4A_2$ ground states, we label $|\pm\frac{1}{2}\rangle$ the two spin sublevels of $\bar{E}$ and $|\pm\frac{3}{2}\rangle$ the two spin sublevels of $2\bar{A}$. The $\bar{E} - 2\bar{A}$ splitting of the $^4A_2$ ground states is well resolved in photoluminescence spectra in Fig. 3.1(a), while that of the ^2E excited state is clearly visible in the absorption spectra of Fig. 3.1(a).

Other lines which can be seen at higher energy in Fig. 3.2(a) have been attributed by Koidl[48] to transitions to other excited levels and to phonon assisted transitions. They are broader, and hence more difficult to study quantitatively in thin layers since transmission spectra are plagued by interferences between the surface of the layer and the interface with the substrate.

In this section we use the $^4A_2 \leftrightarrow {}^2E$ transition to (i) estimate the Co content in samples which have not been characterized by EDX (particularly at low Co content),

(ii) confirm the parameters describing the ground state and the excited state (anisotropy and g-factors), and the oscillator strengths of transitions and (iii) confirm the population distribution in the ground level from a complete description of the intensities of the absorption lines. Thus, we are able to deduce the magnetization of the system of localized spins.

3.2.1 Calibration of Co^{2+} concentration

In a set of samples, where the cobalt concentration was determined by EDX, the absorption coefficient of the ${}^4A_2 \rightarrow {}^2E\ 2\bar{A}$ line [at 1880meV, Fig. 3.2(a)] increases linearly with the increase of the Co concentration up to 6% [full circles in Fig. 3.2(b)]. The calibration curve obtained with these samples was used to determine the cobalt concentration in other samples [open squares in Fig. 3.2(b)].

The linear behavior indicates that the absorption coefficient is sensitive to the total concentration of Co^{2+} ions substituting Zn in the wurtzite lattice. Actually, it is a surprising behavior, because it does not discriminate the different nearest neighbor configurations : isolated ions, antiferromagnetic or ferromagnetic cobalt pairs, triplets, or other complexes. In the cation sublattice of the wurtzite structure, every cation has 12 nearest neighbors : 6 neighbors in the same layer, and 3 neighbors in the next layer on each side, at almost the same distance. These 12 neighbors are usually considered as equivalent (see e.g., the study of $Zn_{1-x}Mn_xO$[73]). Assuming a random distribution of Co ions, the probability to find an isolated cobalt ion (without any cobalt ion in a nearest neighbor position) is given by $x = (1-x)^{12}$. For a total concentration $x = 5.6\%$, half of the Co ions have at least one Co ion as a nearest neighbor. That means that the concentration of isolated Co ions, $x_s = x(1-x)^{12}$, significantly deviates from the straight line drawn in Fig. 3.2(b)].

According to *Sati et al.*,[74] the nearest neighbor exchange coupling for Co in ZnO is $-2J\overrightarrow{S}_1 \cdot \overrightarrow{S}_2$ with $J \leqslant -10$ K. The antiferromagnetic pair thus has an energy shift of $J[S_{tot}(S_{tot}+1) - S_1(S_1+1) - S_2(S_2+1)]$ with $S_{tot} = 0$ and $S_1 = S_2 = 3/2$, hence the shift is around 10 meV, which is significant when compared to the linewidth. Either this shift is compensated by similar shift in the excited state (quite unlikely), either the relative decrease of intensity of the sharp line is compensated - by chance - by a corresponding rise of the background.

3.2.2 Magnetospectroscopy

We combine PL and absorption data involving the ${}^4A_2 \leftrightarrow {}^2E\ \bar{E}$ intra-ionic transitions in order to check the parameters governing the evolution under magnetic field of the ${}^4A_2$ ground state. Fig. 3.3(a) shows the spectra at energy range corresponding to the zero phonon PL lines near 1875 meV. Two PL lines with equal intensities are observed in zero magnetic field. They have been identified[48] as transitions from the excited state ${}^2E\ \bar{E}$ to the two components of the ground state ($|\pm\frac{1}{2}\rangle$ and $|\pm\frac{3}{2}\rangle$). In the presence of a magnetic field parallel to the c-axis, we observe six PL lines [see Fig. 3.3(a)], which we identified as transitions between the different spin sublevels of the ground and excited states split by the Zeeman effect. The optical selection of

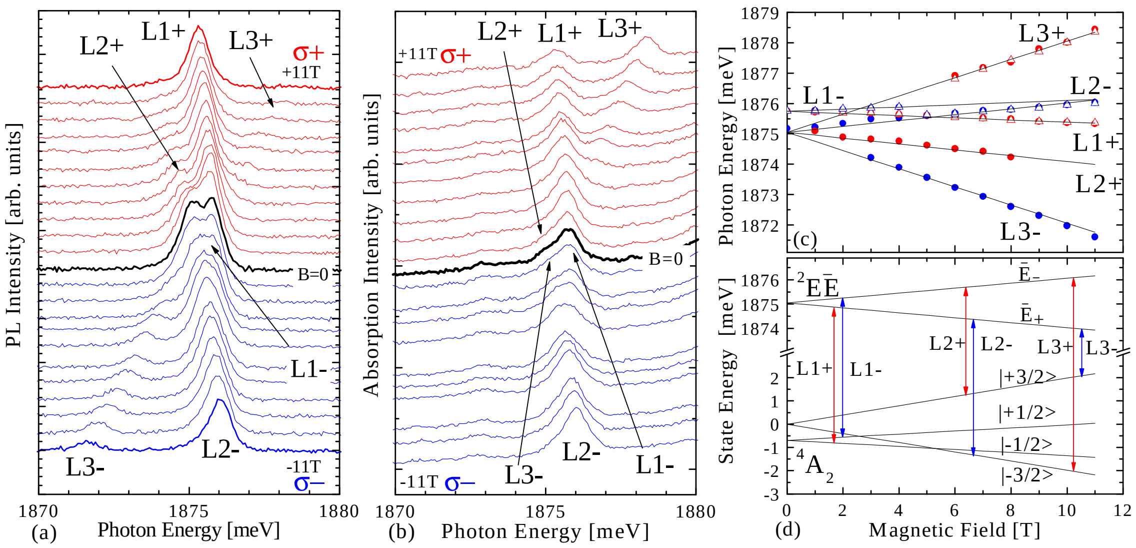

Figure 3.3: Magneto-optical spectroscopy of the $^4A_2 \leftrightarrow {}^2E\ \bar{E}$ transition in a $Zn_{0.98}Co_{0.02}O$ at $T = 7$ K, in σ^+ (top) and σ^- (bottom) circular polarizations. The magnetic field up to 11 T is parallel to the c-axis and to the propagation of light (Faraday configuration). (a) PL spectra. (b) Absorption spectra. (c) Position in energy of the observed PL (full circles) and absorption (triangles) lines, and (solid lines) values calculated using the parameters of Table 3.2. (d) Energy level diagram, as a function of the applied field, and transitions. The spin levels of the ground level quadruplet are marked. Sample ♯Z219c.

such transitions in trigonal symmetry has been described by Macfarlane.[72] They are given in Table 3.1. According to these selection rules, for light propagating along the c-axis, two transitions are forbidden in σ polarization, three lines are observed in σ^+ polarization and three in σ^- polarization. It is what we observe experimentally, as it is shown in Fig. 3.3(a).

	$\lvert+\frac{1}{2}\rangle$	$\lvert-\frac{1}{2}\rangle$	$\lvert+\frac{3}{2}\rangle$	$\lvert-\frac{3}{2}\rangle$
	$^4A_2\ \bar{E}_+$	$^4A_2\ \bar{E}_-$	$^4A_2\ \bar{A}$	$^4A_2\ \bar{A}$
$^2E\ \bar{E}_+\ (\lvert+\frac{1}{2}\rangle)$	π	σ^+	σ^-	σ^-
$^2E\ \bar{E}_-\ (\lvert-\frac{1}{2}\rangle)$	σ^-	π	σ^+	σ^+

Table 3.1: Optical selection rules for dipole transitions in trigonal symmetry (see Macfarlane[72]). These selection rules directly reflect the conservation of total momentum, modulo 3. The π polarization corresponds to the active field of the light parallel to the c-axis of the wurtzite crystal and cannot be observed when light propagates along the c-axis ; the σ polarization corresponds to the active field perpendicular to the c-axis, and is observed with both helicities when light propagates along c.

The transitions observed in PL are also visible in absorption [Fig. 3.3(b)]. Fig. 3.3(c) shows the position of the PL and absorption lines as a function of the intensity of

	Parameter	This work	Literature	Reference
$^2E\ \bar{E}$	$g'_{\|\|}$	-3.52	-3.358	Theory, Macfarlane, Ref. 72
$^4A_2$	$g_{\|\|}$	2.28	2.2384	EPR, Jedrecy *et al.*, Ref. 75
			2.238	EPR, Sati *et al.*, Ref. 76
$\|\pm\frac{1}{2}\rangle \leftrightarrow \|\pm\frac{3}{2}\rangle$	$2D$	0.69 meV	0.682 meV	EPR, Jedrecy *et al.*, Ref. 75
			0.684 meV	EPR, Sati *et al.*, Ref. 76
$\|\pm\frac{3}{2}\rangle \leftrightarrow {}^2E\ \bar{E}$	energy	1875 meV	1877 meV	Absorption, Koidl, Ref. 48

Table 3.2: Parameters describing the spin splitting of the $^4A_2$ ground state quadruplet and the $^4A_2 \leftrightarrow {}^2E\ \bar{E}$ transition. The values were derived from PL and absorption measurements of $Zn_{1-x}Co_xO$ with 2% Co shown in Fig. 3.3.

the magnetic field up to 11T. The solid lines are calculated using 4 fitting parameters : values of the Landé factors $g_{||} = 2.28$ for the ground state and $g'_{||} = -3.52$ for the excited state, a zero-field splitting of the ground state $2D = 0.69$ meV, and an energy of the zero field transition between $|\pm\frac{3}{2}\rangle$ and $^2E\ \bar{E}$ equal to 1875 meV. These parameters, obtained for a (strained) layer with 2% Co, are in good agreement with the values obtained theoretically or from other experimental techniques (see Table 3.2). The corresponding energy diagram and the scheme of transitions are shown in Fig. 3.3(d).

Since we are interested in the magnetic properties of the Co system, it is important to note that in zero magnetic field, the $|\pm\frac{1}{2}\rangle$ states are at lower energy than the $|\pm\frac{3}{2}\rangle$ states. This ordering induces a spin anisotropy with an easy axis perpendicular to the c-axis. Due to the three times larger Zeeman splitting of the $|\pm\frac{3}{2}\rangle$ states,[72] if the field is applied along the c-axis, we expect a crossing of $|-\frac{3}{2}\rangle$ with $|-\frac{1}{2}\rangle$ at 5.2 T [See Fig. 3.3(d)].

3.2.3 Populations of the spin sublevels and magnetization

The magnetization of the Co system is determined by the population of the different spin sublevels of the ground state. We now check these populations using the absorption intensities. Then we calculate the expected magnetization.

For a better accuracy, we used the magneto-absorption spectra of a sample with a higher Co content, 4.5% [Fig. 3.4(a)]. Absorption lines are stronger in this sample, than in more diluted samples, and lines are still well resolved. As absorption intensity of each line is proportional to the population of the initial state, we observe only four $^4A_2 \rightarrow {}^2E\ \bar{E}$ transitions, which are labeled as in Fig. 3.3.

Using the parameters determined from the previous PL and absorption data (Table 3.2), and assuming Gaussian line shapes with a linewidth equal to 1.44 meV, we were able to fit the whole set of spectra with the intensity of each line as adjustable parameters. The resulting intensities are shown by symbols in Fig. 3.4(b). At low

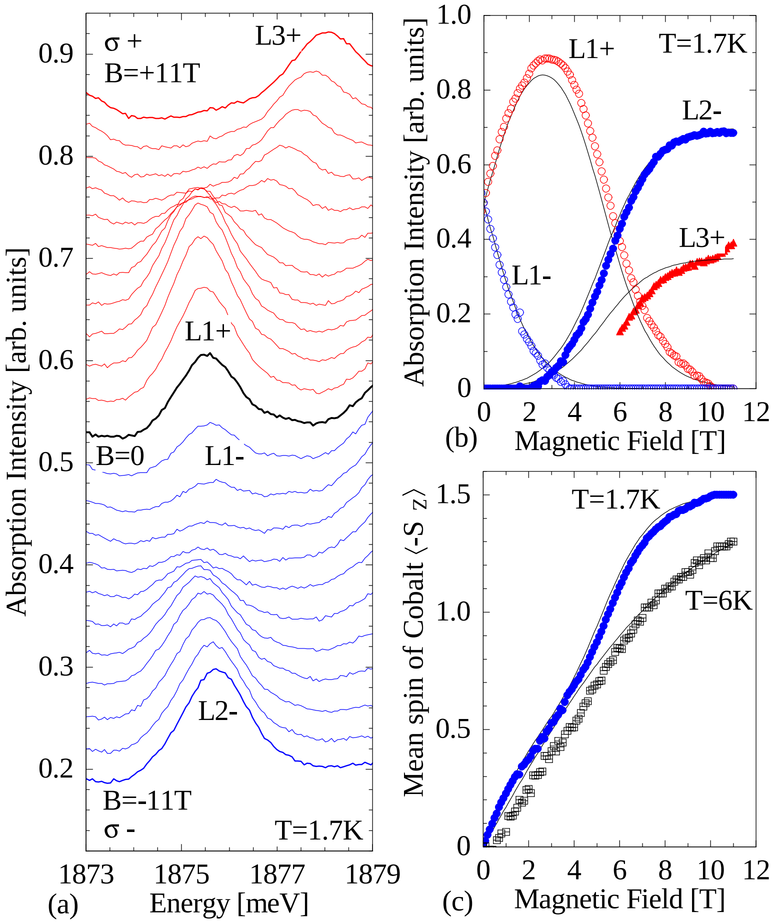

Figure 3.4: (a) Absorption spectra of Zn$_{0.955}$Co$_{0.045}$O measured in the Faraday configuration, at 1.7 K, in a magnetic field up to 11 T, in σ^+ and σ^- circular polarizations. The four transitions observed are labeled according to Fig. 3.3(d). (b) Absorption intensity measured at $T = 1.7$ K (symbols) and calculated using Maxwell-Boltzmann statistics (lines). (c) Mean spin of Co calculated from the absorption intensities (symbols) or from Maxwell-Boltzmann statistics and parameters of Table 3.2 (lines). Sample ♯Z217.

temperature ($T = 1.7$ K), two transitions (L2+ and L3−) remain invisible for any magnetic field.

The integrated intensity of each absorption line is proportional to the occupancy of the initial state and to the oscillator strength of the transition. Relative oscillator strengths are easily determined from extreme cases where only one level is populated. At $T = 1.7$ K and $B = 11$ T only transitions L2− and L3+ are visible [Fig. 3.4 (a) and (b)] because only the $|\text{-}\frac{3}{2}\rangle$ state is occupied. Similarly, in zero magnetic field only the $|\text{-}\frac{1}{2}\rangle$ and $|\text{+}\frac{1}{2}\rangle$ states are occupied so that only L1+ and L1− are observed. Measuring the relative intensities in zero magnetic field and with $B = 11$ T leads to the conclusion that the relative oscillator strengths of L1+, L2−, L3+ are 1 : 0.7 : 0.35 [see Fig. 3.4(b)]. We expect that the pairs of lines (L1+ and L1−), (L2+ and L2−), and (L3+ and L3−), have equal oscillator strengths because of time reversal symmetry in zero field. Independently, the relative oscillator strength of L1+, L2− and L3− can be estimated from the intensity of PL lines in $B = 11$ T, when only the lower component ($\bar{E}_+$) of ${}^2E\bar{E}$ excited state is occupied during the lifetime [Fig. 3.3(a)]. The oscillator strengths are summarized in Table 3.3.

The occupancy of the different spin sublevels can be calculated using the parameters of Table 3.2 and assuming a Maxwell-Boltzmann distribution. The solid

Transition	L1+	L1−	L2+	L2−	L3+	L3−
Excited state	$\bar{E}_+$	$\bar{E}_-$	$\bar{E}_-$	$\bar{E}_+$	$\bar{E}_-$	$\bar{E}_+$
Ground state	$\lvert\text{-}\frac{1}{2}\rangle$	$\lvert\text{+}\frac{1}{2}\rangle$	$\lvert\text{+}\frac{3}{2}\rangle$	$\lvert\text{-}\frac{3}{2}\rangle$	$\lvert\text{-}\frac{3}{2}\rangle$	$\lvert\text{+}\frac{3}{2}\rangle$
Relative OS (from abs.)	1	1	0.7[a]	0.7	0.35[b]	
Relative OS (from PL)	1			0.8		0.15[b]

[a] From time reversal symmetry.
[b] Not very accurate, see Fig. 3.4(b).

Table 3.3: Ratio of the oscillator strengths (OS) of the spin split components of the $^4A_2 \leftrightarrow {}^2E\ 2\bar{A}$ transition in σ polarization. OS equal to 1 corresponds to a peak intensity of $0.14/\mu$m with a linewidth of 1.44 meV measured on a sample with 4.5% Co.

lines in Fig. 3.4(b) show the corresponding intensity calculated for each line using the relative oscillator strengths of Table 3.3. Experimental data for L1+, L1−, and L2− are in good agreement with the simulation. A significant discrepancy appears for L3+. For this line, the determination of the integrated intensity was difficult because of its overlap with L1+. This discrepancy could be also attributed to magnetic field dependence of the oscillator strength.

The experimental absorption intensities divided by the relative oscillator strengths give us a direct information about the expected cobalt mean spin, which can be calculated using

$$\langle\text{-}S_z\rangle_{\text{spectro}} = \frac{\frac{1}{2}(I_{1+} - I_{1-}) + \frac{3}{2}(I_{2-} - I_{2+})/r_{2,1}}{\frac{1}{2}(I_{1+} + I_{1-}) + \frac{3}{2}(I_{2-} + I_{2+})/r_{2,1}}, \tag{3.1}$$

where I_N denotes the experimental intensity of absorption line L_N, and $r_{2,1}$ denotes the oscillator strength ratio of lines L2± and L1± (it is equal to 0.7, see Table 3.3). We do not use L3± since its experimental intensity is doubtful. The resulting value is shown by symbols in Fig. 3.4(c), as a function of the magnetic field along the c-axis, for two temperatures : 1.7 K and 6 K. It clearly deviates from an isotropic Brillouin function, which will be discussed in Sec. 3.6.1.

Here again, assuming a Maxwell-Boltzmann distribution and using the parameters of Table 3.2, we can calculate the mean spin of an isolated cobalt ion, as a function of temperature T and magnetic field B_z along the c-axis,

$$\langle\text{-}S_z\rangle = \frac{\frac{1}{2}\sinh(\frac{1}{2}\delta) + \frac{3}{2}e^{-\frac{2D}{k_BT}}\sinh(\frac{3}{2}\delta)}{\cosh(\frac{1}{2}\delta) + e^{-\frac{2D}{k_BT}}\cosh(\frac{3}{2}\delta)}, \tag{3.2a}$$

$$\delta = \frac{g_{||}\mu_B B_z}{k_BT}, \tag{3.2b}$$

where k_B denotes the Boltzmann constant and μ_B the Bohr magneton. Parameters $g_{||}$ and $2D$ are given in Table 3.2. The results of simulation are shown as solid lines in Fig. 3.4(c). They are in good agreement with the mean spin of magnetic ion determined from absorption intensities of lines split by Zeeman effect.

It is important to note, that particularly for very low temperatures, the field dependence of the magnetization deviates from the Brillouin function $B_{3/2}$ characteristic for an isotropic spin. A step is visible at 5 T, as an effect of the crossing between $|-\frac{3}{2}\rangle$ and $|-\frac{1}{2}\rangle$ [Fig. 3.3(d)]. Also, if we plot the inverse of the low-field susceptibility as a function of temperature, we observe a clear deviation from a Curie law.[77] These two effects should not be misinterpreted as magnetization steps and Curie-Weiss law due to spin-spin interactions as in the case of DMSs containing the isotropic Mn spin ; here they are simply due to the single-ion anisotropy of the Co spin, not to coupling between neighbor spins.

Concluding this section, we observe Co in 2+ state as expected for II-VI DMS, such as ZnO. Moreover, we determine magnetic properties of Co^{2+} using optical spectroscopy : absorption and photoluminescence under magnetic field.

3.3 Absorption of Mn^{2+} in ZnO

Mn^{2+} exhibits broad intra-ionic absorption band above 2.2 eV. It is well known from the optical study of Mn based II-VI DMS such as wurtzite $Zn_{1-x}Mn_xSe$. In ZnO, the energy gap is wide enough to observe quite a large range of this absorption band. The example spectra are given in Fig. 3.5. As it was usually in case of Mn^{2+} in II-VI DMS, we are not able to resolve sharp lines. The energies of various d levels are known from calculation based on photoemission measurements. Following Ref. 78, we give in Table 3.4 the energies of d levels in $Zn_{1-x}Mn_xO$ and $Zn_{1-x}Mn_xTe$ relatively to the ground state.

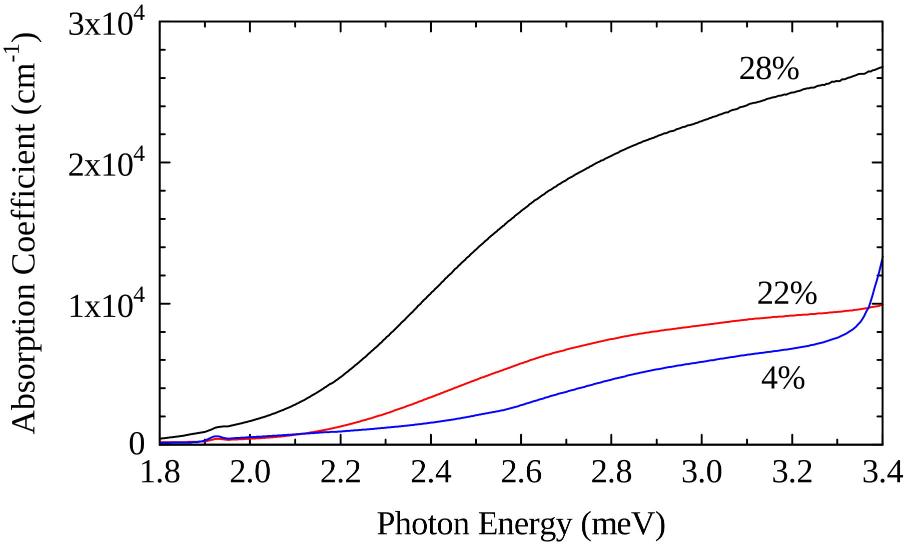

Figure 3.5: Absorption spectra of $Zn_{1-x}Mn_xO$ with $x = 4\%$, 22%, and 28%. Spectra were measured by Katrina Chikoidze, the grower of the sample.

	$^4T_1$	$^4T_2$	^4E	$4A_1$
$Zn_{1-x}Mn_xO$	2.55	2.85	2.97	2.99
$Zn_{1-x}Mn_xTe$	2.22	2.41	2.51	2.61

Table 3.4: After *Mizokawa et al.*, Ref. 78. Calculated energy levels of $^4T_1$, $^4T_2$, ^4E, and $^4A_1$ with respect to the $^6A_1$ ground state of Mn^{2+} impurities in ZnO and ZnTe (in eV).

The comparison of the energies from Tab. 3.4 with absorption and cathodoluminescence spectra has been already done by Jin *et al.*[79] for $Zn_{1-x}Mn_xO$. They found an agreement of various results. However, according to Tab. 3.4, the energy of the first excited state of Mn^{2+} in ZnO is 2.55 eV. The comparison of this value with the absorption threshold (about 2.2 eV in Fig. 3.5) leads to the conclusion that the energies determined in Ref. 78 can be overestimated. Moreover, the absorption intensity of spin forbidden transitions is surprisingly large. Absorption coefficient at 2.6 eV is order of magnitude of 10^4 cm^{-1}, when the absorption of Mn^{2+} in $Zn_{1-x}Mn_xSe$ is 10^2 cm^{-1} at the same energy in sample with comparable concentration of magnetic ions ($x = 23\%$).

Another interpretation has been proposed by Norberg *et al.*[80,81] Using the absorption and MCD of $Zn_{1-x}Mn_xO$ nanocrystalities, they concluded that absorption spectra are strongly affected by charge transfer transitions. Such transitions strongly depend on growth conditions and on the energy position of Fermi level. Anyway, such a very broad absorption can be related to various different effects. Therefore, it is not useful for a determination of the concentration of Mn^{2+}.

Concluding this section, we do not observe sharp lines related to any particular charge state of Mn. It is not surprising for 2+ state of Mn expected for II-VI DMS, such as ZnO. In the next section, we will see that Mn^{3+} in GaN exhibits sharp absorption lines, so we conclude that Mn in ZnO is not in 3+ state. The hypothesis of Mn^{2+} configuration is supported by other characterization results such us concentration of electrons in $Zn_{1-x}Mn_xO$ independent on concentration of Mn, characteristic lines of EPR and magnetic behavior in agreement with a Brillouin function.[60] The magnetooptical effects presented in Chapter 5 confirm also that Mn is in 2+ state in ZnO.

3.4 Absorption and photoluminescence of Mn^{3+} in GaN

Absorption and magnetoabsorption of Mn^{3+} in GaN were studied in details by Wołoś *et al.*[52] and by Marcet *et al.*[47] We used well know absorption lines in order to compare the Mn concentrations in various $Ga_{1-x}Mn_xN$ samples. Fig. 3.6 shows zero-phonon absorption line near 1413 meV measured for samples which exhibit giant Zeeman effect near the energy gap, and which were characterized by SIMS. The integrated absorption increases with the Mn concentration. The inset of Fig. 3.6

shows that the dependence is slightly nonlinear. One sample ($x = 0.1\%$ according to SIMS) shows a surprisingly strong Mn absorption for such Mn concentration. The linewidth is also surprisingly large for a diluted sample (compare to $x = 0.45\%$). This suggest that the sample with $x = 0.1\%$ according to SIMS, has in fact a high Mn concentration, but it is nonhomogeneous. In such sample, SIMS measurements can give different results depending on the position of the spot. This hypothesis is in agreement with nonhomogeneity noticed visually in samples with high Mn concentration.

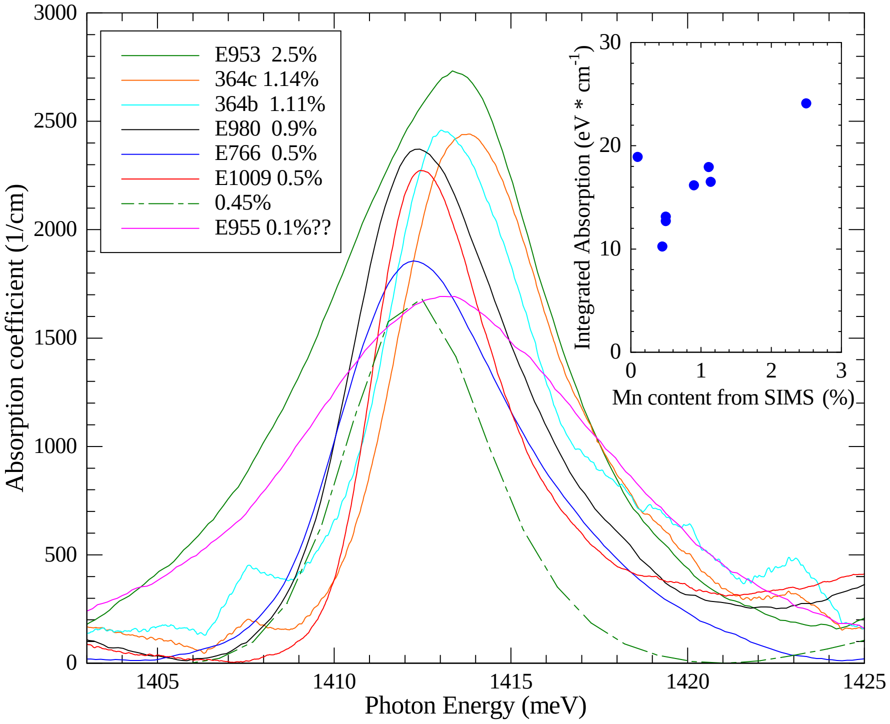

Figure 3.6: (a) Absorption spectra of Mn^{3+} in $Ga_{1-x}Mn_xN$ samples with various manganese concentration x, at helium temperature. We think, that the sample with $x = 0.1\%$ according to SIMS, has in fact much higher Mn concentration, but it is nonhomogeneous. (b) The integrated absorption as a function of the Mn concentration determined by SIMS.

Fig. 3.7 (a) gives examples of magnetoabsorption spectra, which are very similar to spectra already described by Marcet *et al.*,[47] who determined parameters given in Table 3.5.

So far, the photoluminescence of Mn^{3+} was to weak to be observed in the cryostat equipped with magnet. Marcet *et al.* observed only cathodoluminescence in zero field.[47] We have an opportunity to measure in Warsaw and Grenoble the PL lines of Mn^{3+} thanks to the collaboration with Jan Zenneck from Georg-August Universität Göttingen, Germany. Zenneck *et al.*[82] observed zero-field PL in diluted MOCVD grown $Ga_{1-x}Mn_xN$. Using this high quality sample, we have measured with Jan Zenneck a magneto-PL shown in Fig. 3.7(b). It was measured for the same sample and in the same experimental conditions as transmission in 3.7(a). One can expect that measurement of the PL should give much more information than zero-field

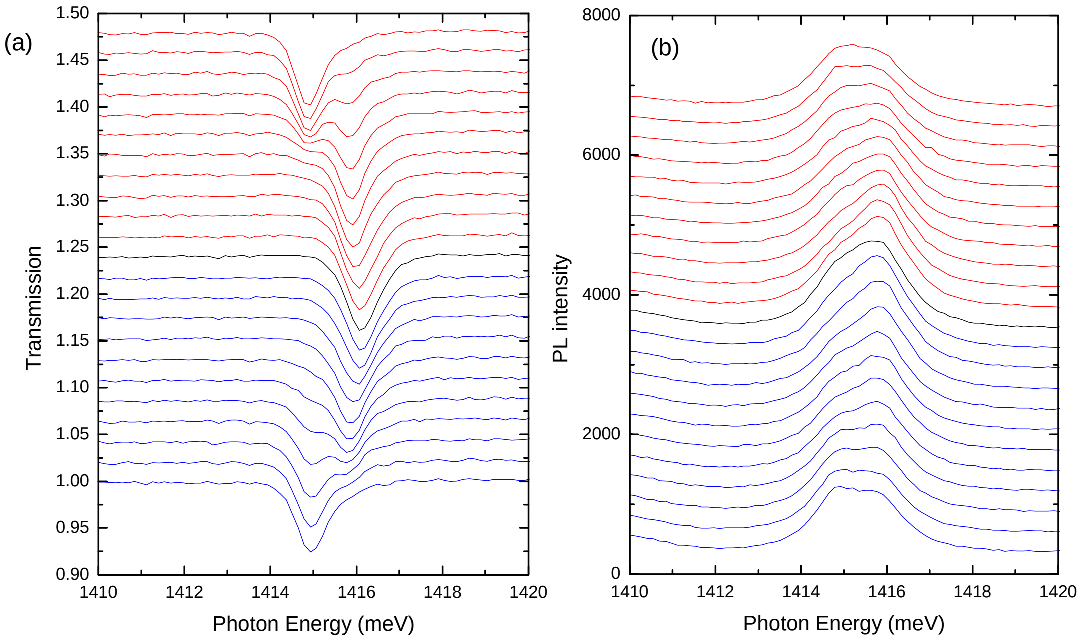

Figure 3.7: Transmission (a) and PL (b) spectra of Mn^{3+} in diluted $Ga_{1-x}Mn_xN$ grown in Göttingen using MOCVD technique. The temperature for both measurements : PL and transmission is 1.7 K. Sample ♯G0117.

spectrum, as it was the case for Co^{2+}, where the PL line splits into 6 lines under magnetic field (see Fig. 3.3). Fig. 3.7 shows that Mn^{3+} line in GaN is different. Despite of very sharp lines (compare to Ref. 47), we cannot resolve more under magnetic fields than in zerofield. We relate the difference between the Mn^{3+} and Co^{2+} to the different strength of the Jahn-Teller effect, which affects optical selection rules and g-factors. Wołoś *et al.*[52] and Marcet et al.[47] show that Jahn-Teller effect is important for Mn^{3+} in GaN, and Koidl shows that this effect is weak for Co^{2+} in ZnO.

Concluding this section, we observed Mn in 3+ state. It was not evident in III-V DMS, such as GaN. Our conclusion is in agreement with the absence of characteristic EPR lines of Mn^{2+} noticed by Sati and Stepanov[83] in our $Ga_{1-x}Mn_xN$. The magnetic behavior studied using spectroscopy of excitons (Chapter 5) confirm also that Mn is in 3+ state.

3.5 Photoluminescence of Fe^{3+} in GaN

The sharp photoluminescence lines of Fe^{3+} are much easier to be observed than sharp absorption lines. This is a different behavior in comparison to the observed one for Mn^{3+}. We measured PL spectra of $Ga_{1-x}Fe_xN$ at two temperatures. The spectra are shown in Fig. 3.8. There are more visible lines at T = 15 K than at T = 1.6 K. This demonstrates the presence of various excited states separated by a small energy, about 2 meV. The properties of these PL lines have been studied in detail by Heitz *et al.*[84] The study included a measurement of the Zeeman effect.

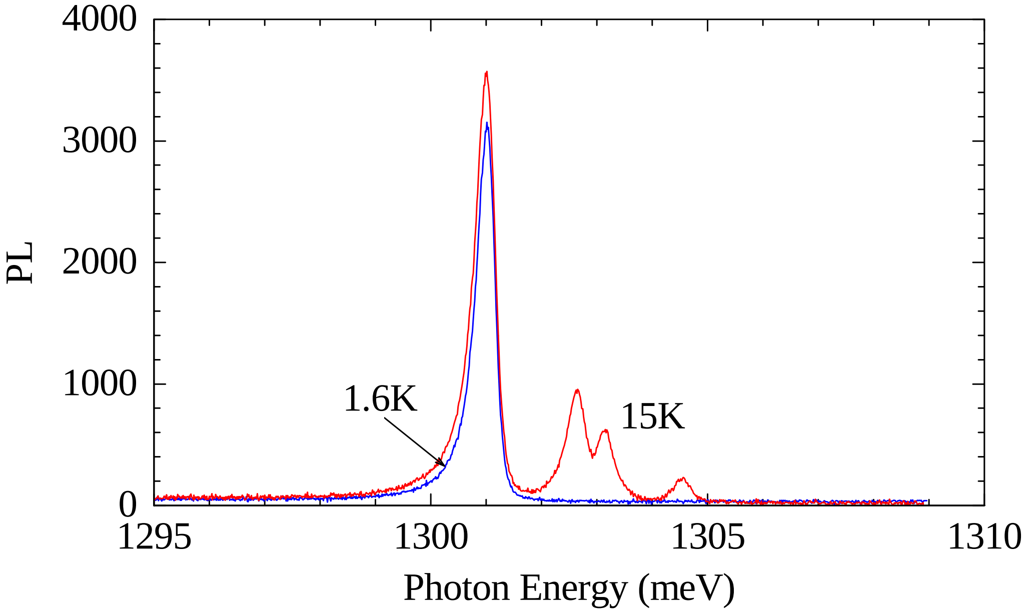

Figure 3.8: PL spectra of Fe^{3+} in diluted $\mathrm{Ga}_{1-x}\mathrm{Fe}_x\mathrm{N}$, measured at $T = 1.6$ K and $T = 16$ K.

The results were well explained using parameters obtained by EPR (see Table. 3.5).

Basing on the spectra of Fig. 3.8, we may conclude that the observed charge state is Fe^{3+}. Thus, the Fermi level is low enough to allow existence of Fe^{3+} in our $\mathrm{Ga}_{1-x}\mathrm{Fe}_x\mathrm{N}$ samples. EPR signal (studied by Wołoś and Jantsch) and magnetic behavior (studied by Kiecana and Sawicki) suggest that Fe is mostly in 3+ configuration in our samples. This is confirmed also by magnetooptical study of excitons, which evidences magnetization following Brillouin function characteristic for $S = 5/2$ (Fe^{3+}). In any characterization we do not find any trace of Fe^{2+}

3.6 Discussion : comparison of the magnetic behavior of Co^{2+}, Mn^{2+}, Mn^{3+}, and Fe^{3+}

The nature of magnetism in wide gap DMS is quite complex and it is not our purpose to discuss here all related aspects. Moreover, there are still effects, which are a matter of controversy, e.g. the origin of room temperature ferromagnetism. In this section, we present only the most important effects needed to understand the temperature and magnetic field dependence of the giant Zeeman splitting in diluted samples. The giant Zeeman splitting is described in Chapter 5. We did measurements used for determination of the giant Zeeman effect at high magnetic field, B<11T, and at low temperature, 1.5K <T<30K. In the first place (Sec. 3.6.1), we present the description of isolated ions. This assumption is accurate for very low concentrations of magnetic ions. In Sec. 3.6.2, we take into account effect of *d*-*d* interaction between magnetic ions, simply by using an effective concentration.

The magnetization of ion system $\langle M_z \rangle$ is directly related to the mean spin value

$\langle S_z \rangle$:

$$\langle M_z \rangle = -g\ \mu_B\ N_0\ x\ \langle S_z \rangle \tag{3.3}$$

where g is g-factor, μ_B is the Bohr magneton, N_0 is cation density, x is magnetic ions content. Both quantities $\langle M_z \rangle$ and $\langle S_z \rangle$ have the same temperature and magnetic field dependence, so we will discuss them at the same time. Note that $\langle S_z \rangle < 0$ when $\langle M_z \rangle > 0$. Therefore we will rather use in our discussion the positive quantity $\langle$-$S_z \rangle$.

3.6.1 Magnetization of the system of isolated ions

Brillouin function

The magnetic behavior of isotropic ions with spins S is governed by the Brillouin function[85] :

$$B_S(\xi) = \frac{2S+1}{2S} \coth\left(\frac{2S+1}{2S}\xi\right) - \frac{1}{2S} \coth\left(\frac{1}{2S}\xi\right), \tag{3.4}$$

which allow us to calculate the magnetization or the mean spin of the system of noninteracting spins :

$$\langle\text{-}S\rangle = S B_S\left(\frac{g\mu_B S B}{k_B T}\right), \tag{3.5}$$

where k_B denotes the Boltzmann constant.

The Brillouin function is appropriate for the description of the magnetization in case of ions with negligible zero field splitting of the fundamental state (isotropic ions), which is the case for Mn and Co based DMS with the zinc blende structure. This function does not take into account any interactions between magnetic ions.

Magnetization of strongly anisotropic ions

In the wurtzite structure, and particularly in wide gap DMS, the trigonal crystal field combined with spin-orbit interaction induce a strong magnetic anisotropy, which can be described by a zero-field splitting of the fundamental state and by an anisotropic effective g-factor. We will show, that only the magnetic ions with zero orbital momentum, such as Mn^{2+} or Fe^{3+} ($S = 5/2$), can be approximately described using a Brillouin function (3.4). For other spin configurations, the effect of spin orbit coupling within the magnetic ion must be taken into account. Then, the ground state of isolated magnetic ion under magnetic field can be described by spin hamiltonian[86] :

$$H_\mathrm{s} = \mu_B g_\parallel B_z S_z + \mu_B g_\perp (B_x S_x + B_y S_y) + D S_z^2, \tag{3.6}$$

where S is the spin and D describes the zero field splitting. $g_\parallel$ and $g_\perp$ are the effective g-factors for directions of magnetic filed parallel and perpendicular to the

Ion	Host	Spin	D (meV)	$g_{\parallel}$	$g_{\perp}$	References
Co^{2+}	ZnO	3/2	0.341	2.2384	2.2768	Jedrecy *et al.*, Ref. 75
Co^{2+}	ZnO	3/2	0.342	2.238	2.2755	Sati *et al.*, Ref. 76
Co^{2+}	ZnO	3/2	0.345	2.28		this work, Ref. 34
Co^{2+}	CdSe	3/2		2.295	2.303	Hoshina, Ref. 66
Co^{2+}	CdSe	3/2	0.062			Lewicki *et al.*, Ref. 67
Co^{2+}	CdS	3/2	0.084			Lewicki *et al.*, Ref. 67
Mn^{3+}	GaN	2	0.27	1.91	1.98	Marcet *et al.*, Ref. 47
Fe^{3+}	ZnO	5/2	-0.0074	2.0062	2.0062	Heitz *et al.*, Ref. 65
Mn^{2+}	ZnO	5/2	-0.0027	2.0016	2.0016	Chikoidze *et al.*, Ref. 73
Fe^{3+}	GaN	5/2	-0.0093	1.990	1.997	Heitz *et al.*, Ref. 84
Fe^{3+}	GaN	5/2		2.009	2.005	Bonanni *et al.*, Ref. 62

Table 3.5: Parameters describing the anisotropy of selected magnetic ions in wurtzite semiconductors. Note that particularly significant anisotropy can be observed for ions with spin other than 5/2 in wide gap DMS.

c-axis, respectively. This Hamiltonian contains only terms, which are the most important for the calculation of the magnetization. A more advanced description links the phenomenological parameters of (3.6) with more general properties of the crystal and magnetic ions (see Refs 48 and 74). For instance, they include hyperfine interactions[75] or Jahn Teller effect.[47,53,84]

Parameters of the hamiltonian (3.6) are given in Table 3.5 for selected magnetic ions in wurtzite semiconductors. The Zeeman splitting calculated for various spin configurations is shown in Fig. 3.9, for $B||c$-axis. Magnetic ions with $S = 5/2$ have two orders of magnitude smaller zerofield splitting than other spin configurations. The g-factors for $S = 5/2$ spin configuration are also almost independent on the direction of magnetic field, and the values of both $g_{\parallel}$ and $g_{\perp}$ are close to 2. Ions with $S = 5/2$ have 5 electrons on d shell, so orbital momentum is equal to zero. Since the main contribution to the anisotropy results from spin-orbit interaction, ions with $S = 5/2$ remain almost isotropic even in the strongly anisotropic wurtzite structure. Consequently, the magnetization of a $S = 5/2$ spin can be well described by a Brillouin function. It is different in the case of $S = 3/2$ or $S = 2$, for which the zero field splitting is comparable to k_BT under typical experimental conditions. For example : liquid helium has temperature $T = 4.2$ K, and it corresponds to $k_BT = 0.36$ meV. The zero field splitting for $S = 3/2$ is equal to $2D$, so it is equal to 0.69 meV for Co^{2+} in ZnO. Hence, the zero field splitting is twice larger than k_BT. Similar situation is for Mn^{3+} in GaN. Therefore, the anisotropy is crucial for the magnetization of $S = 3/2$ and $S = 2$ spin configurations in wide gap DMS. In CdSe and CdS, zero field splitting are about 4 times smaller, and $2D$ values correspond to k_BT at superfluid helium temperature.

Below we give analytic expressions describing magnetization curves for magnetic field parallel to the c-axis (B_z). We calculated them by combining hamiltonian 3.6 and Maxwell-Boltzman distribution. The projection of the mean spin for magnetic ion with $S = 2$ (e. g. Mn^{3+}, Cr^{2+}, Fe^{2+}, Co^{3+}) is given by :

$$\langle\text{-}S_z\rangle = \frac{e^{-d}\sinh(\delta) + 2e^{-4d}\sinh(2\delta)}{\frac{1}{2} + e^{-d}\cosh(\delta) + e^{-4d}\cosh(2\delta)}, \tag{3.7}$$

for ions with $S = 3/2$ (e. g. Cr^{3+}, Co^{2+}, V^{2+}) :

$$\langle\text{-}S_z\rangle = \frac{\frac{1}{2}\sinh(\frac{1}{2}\delta) + \frac{3}{2}e^{-2d}\sinh(\frac{3}{2}\delta)}{\cosh(\frac{1}{2}\delta) + e^{-2d}\cosh(\frac{3}{2}\delta)}, \tag{3.8}$$

for ions with $S = 1$ (e. g. Co^{+}) :

$$\langle\text{-}S_z\rangle = \frac{e^{-d}\sinh(\delta)}{\frac{1}{2} + e^{-d}\cosh(\delta),} \tag{3.9}$$

where

$$d = \frac{D}{k_B T}, \tag{3.10}$$

$$\delta = \frac{g_{||}\mu_B B_z}{k_B T}. \tag{3.11}$$

Using the same notation, the magnetization for $S = 5/2$ (e. g. Mn^{2+}, Fe^{3+}), can be expressed by :

$$\langle\text{-}S_z\rangle = \frac{\frac{1}{2}\sinh(\frac{1}{2}\delta) + \frac{3}{2}e^{-2d}\sinh(\frac{3}{2}\delta) + \frac{5}{2}e^{-6d}\sinh(\frac{5}{2}\delta)}{\cosh(\frac{1}{2}\delta) + e^{-2d}\cosh(\frac{3}{2}\delta) + e^{-6d}\cosh(\frac{5}{2}\delta)}, \tag{3.12}$$

however the anisotropy of magnetic ions with $S = 5/2$ is negligible at $T > 1$ K. Thus the Brillouin function (3.4) could be efficiently used instead of the above equation. Fig. 3.9 shows that anisotropy cannot be neglected for low temperature magnetization of Co^{2+} in ZnO and Mn^{3+} in GaN, when the magnetic field is along the hard magnetization axis (c-axis). For the easy magnetization plane (perpendicular to c-axis), the deviation from Brillouin function is much weaker.

3.6.2 Magnetization of the system of interacting ions

The magnetic properties of isolated ions and ions possessing nearest neighbors are expected to be very different at low temperature due to the exchange ion-ion interaction (d-d interaction). Since d-d interaction is antiferromagnetic, the nearest-neighbor pairs are blocked antiparallel. In many DMS, this gives rise to a series of steps and plateaux observed in the high field part of the magnetization cycles (e.g. tens of T) measured at very low temperature (order of mK). Such steps on magnetization curve has been already observed for wide gap DMS : $Zn_{1-x}Mn_xO$,[87]

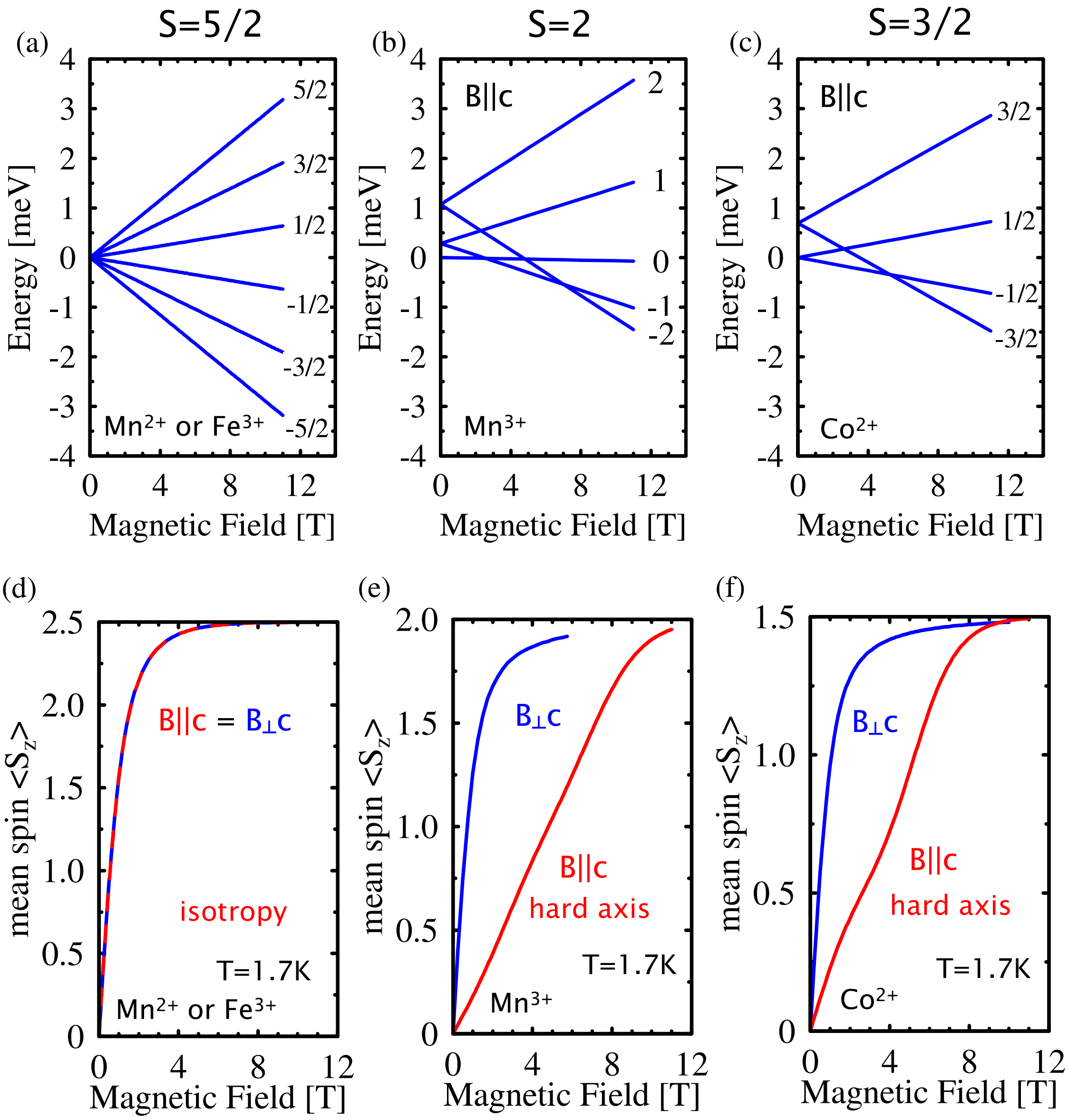

Figure 3.9: (a,b,c) Zeeman splitting of the fundamental state of various magnetic ions in wide gap DMS. Magnetic field is parallel to the c-axis. (d,e,f) Calculated mean spin of magnetic ions. It is calculated for two directions of magnetic field.

at temperature 20 mK. At higher temperatures (e.g. $T > 1$ K) and lower magnetic fields these steps are not visible any more, but the magnetization is expected to deviates from the curve describing isolated magnetic ions. In the next paragraph, we will show the phenomenological approach to this problem.

Effective concentration

The most important effect of the antiferromagnetic interactions between magnetic ions is a decrease of the total magnetic moment. At low temperature, small magnetic field, and low concentration of magnetic ions, the reduced magnetization can be phenomenologically taken into account if one replaces the total concentration of magnetic ions x by an effective concentration x_{eff}. The effective concentration x_{eff} describes concentration of magnetic ions contributing to the total magnetization. An approximation of x_{eff} can be calculated assuming that only isolated magnetic ions contribute to the magnetization : pairs are antiferromagnetically block, and the magnetic contribution of other complexes is negligible. Then, the probability, that any of 12 nearest neighboring places is occupied by other magnetic ions, is equal to $(1-x)^{12}$ (see Ref. 71). Hence effective concentration as a function of concentration can be estimated by :

$$x_{eff} = x(1-x)^{12} \tag{3.13}$$

This approximation works properly for low concentration of magnetic ions, where concentration of various complexes $x - x(1-x)^{12}$ is much smaller than x_{eff}.

Effective temperature

For higher concentration of magnetic ions the phenomenological parameter x_{eff} can be not sufficient to approximate the effect of *d-d* interactions on magnetization. It has been shown for Mn based II-VI DMS, that additional phenomenological parameter, an effective temperature $T + T_0$, can give reasonable description of the magnetization. Using this approach the magnetization of isotropic ions is given by :[88]

$$\langle M_z \rangle = g\mu_B N_0 x_{eff} S_0 B_S \left(\frac{g\mu_B S B}{k_B(T+T_0)} \right), \tag{3.14}$$

where T_0 depend on the magnetic ions concentration (it increases with x). We will show in Chapter 5, that we do not have a reason to introduce an effective temperature in our calculations for wide gap DMS. A more advance description of ion-ion interactions has been given in Ref. 87 for $\mathrm{Zn}_{1-x}\mathrm{Mn}_x\mathrm{O}$ and in Ref. 74 for $\mathrm{Zn}_{1-x}\mathrm{Co}_x\mathrm{O}$.

Chapter 4

Giant Zeeman effect in wide gap DMS (model)

In this chapter, we summarize basic properties of hexagonal diluted magnetic semiconductor. Step by step, several effects are introduced. We describe the conduction band and the valence band of the semiconductor with wurtzite structure. We discuss the standard description of the giant Zeeman splitting of bands induced by the coupling with magnetic ions. Splitting of bands and selection rules allow us to describe model of band-to-band transition. In this simple approach excitonic effects are neglected. This model has been used so far in wurtzite DMS based on CdS and CdSe. In the next section, electron-hole exchange interaction is taken into account within the exciton and a complete description of excitonic giant Zeeman splitting is given. Finally, we describe interaction between excitons and photons, which leads to polaritonic effects. We discuss importance of described effects for wide gap DMS.

Ce chapitre récapitule les principes de la physique des semi-conducteurs magnétiques dilués à structure wurtzite. D'abord, nous décrivons la structure de la bande de conduction et de la bande de valence de ces semi-conducteurs. Nous discutons de manière usuelle l'effet Zeeman géant induit par le couplage avec les ions magnétiques. Dans cette approche simplifiée, les effets excitoniques sont négligés. Ce modèle était déjà employé dans les semiconducteurs magnétiques dilués wurtzites à base de CdS et CdSe. Nous nous penchons finalement sur l'interaction de l'échange électron-trou, et nous exposons une description complete de l'effet Zeeman géant tenant compte des effets excitoniques. Pour finir, nous nous montrons que l'interaction entre les excitons et les photons mène à la formation de polaritons et nous discuterons l'importance des effets présentés ici pour les semi-conducteurs magnétiques dilués à large bande interdite.

4.1 Introduction

Spectroscopy of excitons in diluted magnetic semiconductors has long tradition : starting from seventies, giant Zeeman effect of excitons has been observed and described for more than 20 DMSs based on II-VI compounds. One could expect that nothing new, except maybe material parameters, should be needed to describe giant Zeeman effect in new DMSs based on ZnO and GaN. This is only partially true, because the new material parameters can determine importance of new effects. Novelty of wide gap DMSs is related to strong electron-hole exchange interaction, which make classical description based on band-to-band optical transitions oversimplified. Moreover, the observed giant Zeeman splittings are very small, and one cannot limit analysis of excitonic shifts to the cases where various exciton lines do not overlap in the optical spectra. Therefore, we needed a model which describe precisely optical spectra with many exciton lines. Such a model required taking into account also interaction between photons and excitons, which results in formation of quasi particles called polaritons.

4.2 Band structure of wurtzite semiconductor

ZnO, GaN, and diluted magnetic semiconductors based on them crystallize naturally in the wurtzite structure. The energy of hole in the Γ point of the valence band, in quasi-cubic approximation is given by :[89]

$$H_{\mathrm{v}} = -\tilde{\Delta}_1(l_z^2\text{-}1) - 2\Delta_2 l_z s_z - 2\Delta_3(l_x s_x + l_y s_y), \tag{4.1}$$

where $\tilde{\Delta}_1 = \Delta_1 + \delta_1$ describes the effect of the trigonal components of crystal field (Δ_1) and biaxial strain in epitaxial leyer (δ_1). Since result presented in this work are obtained on samples grown on (0001) direction, we do not expect uniaxial strain[89, 90] in our samples, and we neglected such strain in hamiltonian (4.1). Δ_2 and Δ_3 are parameters of the anisotropic spin-orbit interaction : $\Delta_2 = \Delta_{SO_\parallel}/3$, $\Delta_3 = \Delta_{SO_\perp}/3$, where Δ_{SO} is a value of spin orbit coupling in cubic approximation.[91] l_α and s_α are the projections of the orbital and spin momenta, respectively. The z direction is parallel to the c-axis. Further, we will use the following basis to describe effect of above hamiltonian : $|p^+\uparrow\rangle$ and $|p^-\downarrow\rangle$ (which form $\Gamma_{9(5)}$ state), $|p^+\downarrow\rangle$ and $|p^-\uparrow\rangle$ (which contribute mainly to $\Gamma_{7(5)}$ state), $|p^z\downarrow\rangle$ and $|p^z\uparrow\rangle$ (which contribute mainly to $\Gamma_{7(1)}$ state). Here, the arrows denote sign of spin projection ($s_z = \pm\frac{1}{2}$). We note p^+, p^-, and p^z for the hole states with orbital momenta $l_z = +1$, -1, and 0, respectively. Γ_9 and Γ_7 denote symmetry of valence states when spin-orbit coupling is taken into account. The number in parenthesis (5 and 1 in $\Gamma_{9(5)}$, $\Gamma_{7(5)}$, $\Gamma_{7(1)}$) indicates the parent state without spin-orbit coupling, as it is shown in Fig. 4.1. State $\Gamma_{7(1)}$ is build mainly from function with orbital momentum $l = 0$. State $\Gamma_{7(5)}$ is build mainly from function with orbital momentum $l = \pm 1$ with spins antiparallel to orbital momentum. State $\Gamma_{9(5)}$ is build mainly from function with orbital momentum $l = \pm 1$ with spins parallel to orbital momentum.

States $\Gamma_{9(5)}$, $\Gamma_{7(5)}$, $\Gamma_{7(1)}$ described by hamiltonian (4.1) form three valence band edges. Their splitting is a result of the combined effect of the trigonal crystal field (described by Δ_1) and the anisotropic spin-orbit coupling (two parameters, Δ_2 and Δ_3). In ZnO the spin-orbit coupling is much smaller than the trigonal crystal field (more precisely, Δ_3 is much smaller than Δ_1-Δ_2). Hence the trigonal field splits

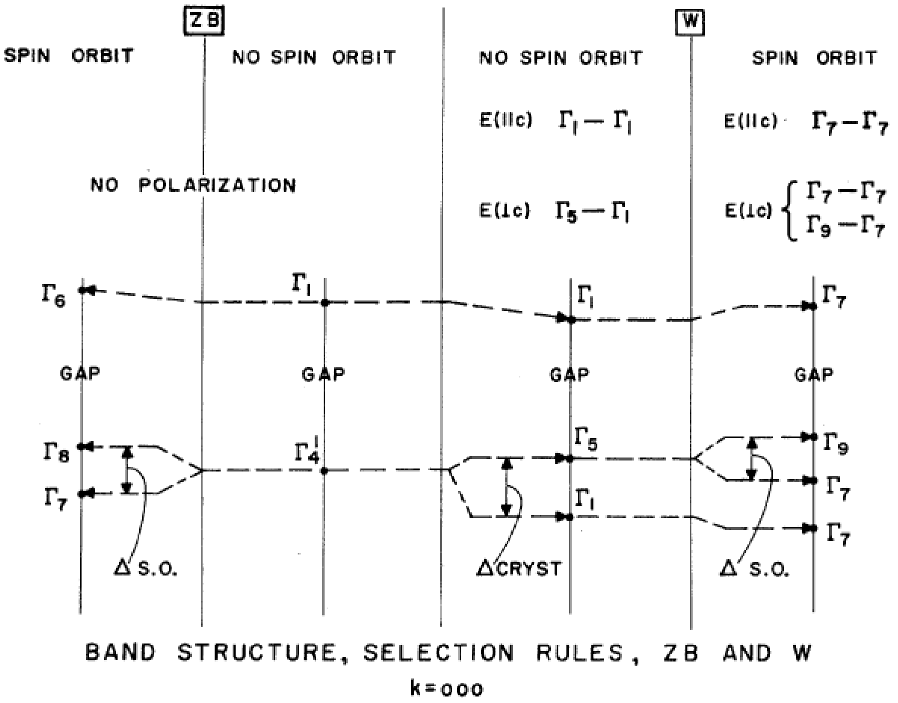

Figure 4.1: After J. Birman, Ref. 92. Band structure of Zinc Blende (left half) and Wurtzite (right half) semiconductor. Impact of spin-orbit interaction on symmetry is shown by arrows.

the *p*-like states which form the bottom of the valence band into a doublet (Γ_5 in-plane *p*-states) and a singlet (Γ_1 out-of-plane *p*-states). As a result of the spin-orbit coupling, the orbital doublet is split into two (orbit+spin) doublets ($\Gamma_{7(5)}$, $\Gamma_{9(5)}$), and the orbital singlet forms a $\Gamma_{7(1)}$ doublet with a very small admixture of the $\Gamma_{7(5)}$ states. In bulk GaN the mixing between valence states $\Gamma_{7(1)}$ and $\Gamma_{7(5)}$ is much stronger. However, for epitaxial layers compressive biaxial strain usually decreases this mixing by the increase of $\Gamma_{7(1)} - \Gamma_{7(5)}$ splitting. Fig. 4.1 compares band structure of zinc blende and wurtzite semiconductor. The most important difference lays in strong optical anisotropy induced by crystal field in wurtzite structure.

In order to understand principal effect of the hamiltonian (4.1), we can assume for a while that spin-orbit interaction is much weaker than crystal field and strain (good approximation for ZnO). Therefore, the Δ_3 parameter is much smaller than ($\Delta_1 - \Delta_2$), and consequently we obtain the approximate splitting energies of hole states : $E_{\Gamma_{7(5)}} - E_{\Gamma_{9(5)}} = 2\Delta_2$, $E_{\Gamma_{7(1)}} - E_{\Gamma_{9(5)}} = \Delta_1 + \Delta_2$, and $E_{\Gamma_{7(1)}} - E_{\Gamma_{7(5)}} = \Delta_1 - \Delta_2$.

It is used to labeled the three valence band edges phenomenologically : *A* (the lowest hole energy), *B* (the middle), and *C* (the highest hole energy), independently on their symmetry. In GaN, the problem of the symmetry of valence bands has been definitely solved.[93] Valence band ordering is the same as in the Fig. 4.1, and as majority of wurtzite semiconductors ($\Gamma_{9(5)}$, $\Gamma_{7(5)}$, $\Gamma_{7(1)}$). However the position and the symmetry of the valence edges are still a mater of controversy in ZnO, even in bulk crystals.[91,94] If a positive spin-orbit coupling (Δ_2) is assumed for ZnO,[95–98] the

Semiconductor	Δ_1 (meV)	Δ_2 (meV)	Δ_3 (meV)	γ (meV)	References
CdSe	68.8	138	150.7	0.4	[95]
CdS	28.4	20.9	20.7	2.5	[95]
ZnO	36.3	1.9	7.4	5.6	[95]
GaN	10	6.2	5.5	0.6	[89, 104]

Table 4.1: Band parameters and the energy of electron-hole exchange in selected wurtzite semiconductors. For values of this parameters determined in the presence of magnetic ions see Refs 34, 68, 101–103.

valence band ordering is the same as in GaN. If a negative spin-orbit coupling is assumed,[91, 99, 100] the ordering is : $\Gamma_{7(5)}$, $\Gamma_{9(5)}$, $\Gamma_{7(1)}$, so it is a different case from the one shown in the Fig. 4.1, and different from GaN.

Other wurtzite crystals, which have been already used as a host materials for diluted magnetic semiconductors are CdS and CdSe.[68, 101–103] They could be described using the same formulas as ZnO or GaN based DMS, however material parameters are significantly different for different materials (see Table 4.1). In particular, the spin orbit coupling (Δ_2 and Δ_3) is strongly reduced in wide gap semiconductors. Also electron-hole exchange interaction (γ) (to be described in Sec. 4.5.1) is particularly strong in ZnO. We will show that this leads to significant differences between the giant Zeeman splitting of bands and excitons.

4.3 Giant Zeeman splitting of bands

In diluted magnetic semiconductors, the presence of the s, p-d exchange interactions leads to large magneto-optical effects such as giant Zeeman splitting and giant Faraday rotation. These effects have been studied in detail in several wurtzite II-VI DMSs like $Cd_{1-x}Mn_xSe$,[101, 105] $Cd_{1-x}Co_xSe$,[68, 106] $Cd_{1-x}Fe_xSe$,[107] $Zn_{1-x}Mn_xSe$,[108] and $Cd_{1-x}Cr_xS$.[102]

The effective hamiltonian describing the giant Zeeman effect in virtual crystal and mean field approximations is following :

$$H_{s-d} = -N_0 \alpha x_{eff} \langle \vec{\mathbf{S}} \rangle \cdot \vec{s}_e, \tag{4.2}$$

for the conduction band electron, and

$$H_{p-d} = -N_0 \beta x_{eff} \langle \vec{\mathbf{S}} \rangle \cdot \vec{s}_h, \tag{4.3}$$

for the valence band hole, where N_0 denotes the number of cations per unit volume, x_{eff} the free magnetic ion content, α the exchange constant for the conduction band, β the exchange constant for the valence band, $\langle \vec{\mathbf{S}} \rangle$ the mean spin of the free magnetic ions and $\vec{s}_e$ and $\vec{s}_h$ are the spin of the electron and hole, respectively. The mean value of the isolated spin $\langle S_z \rangle$ has been already discussed in Sec. 3.6.

The conduction band at the center of Brillouin zone is doubly degenerate, so *s-d* exchange interaction (4.2) induces a simple splitting, independent of the direction of magnetic field (or more precisely, direction of the magnetization). Neglecting the contribution of the weak Zeeman effect of the host semiconductor (see. 4.6), the energy of the conduction band is given by :

$$E = E_0 \pm G_e, \tag{4.4}$$

where E_0 denotes band gap energy, and $G_e = \frac{1}{2} N_0 \alpha x_{eff} \langle\text{-}S_z\rangle$. The sign of $\pm G_e$ corresponds to the electron spin projection $s_e = \pm\frac{1}{2}$, and to the conduction band wavefunction $|s\uparrow\rangle$ and $|s\downarrow\rangle$, respectively. Here, the arrows denote sign of the electron spin.

In order to calculate the effect of the *p-d* Hamiltonian (4.3), we have to take into account the anisotropic structure of the valence band described by equation (4.1). Consequently, the exchange splitting is different for magnetic field parallel and perpendicular to the *c*-axis. We can express explicitly the energy of the valence band hole for magnetic field parallel to the *c*-axis. The energy of hole containing contribution of $p^\pm$ wavefunction is given by :[68, 101, 102, 105–108]

$$E^{p^\pm}_{\Gamma_{9(5)}} = -\Delta_2 \pm G_h, \tag{4.5}$$

$$E^{p^\pm}_{\Gamma_{7(5)}} = \frac{\tilde{\Delta}_1 + \Delta_2}{2} - E_\pm, \tag{4.6}$$

$$E^{p^\pm}_{\Gamma_{7(1)}} = \frac{\tilde{\Delta}_1 + \Delta_2}{2} + E_\mp, \tag{4.7}$$

where

$$G_h = \frac{1}{2} N_0 \beta x_{eff} \langle\text{-}S_z\rangle \tag{4.8}$$

$$E_\pm = \sqrt{\left(\frac{\tilde{\Delta}_1 - \Delta_2}{2} \pm G_h\right)^2 + 2\Delta_3^2}, \tag{4.9}$$

The equations are relatively simple because the state $\Gamma_{9(5)}$ does not interact with states $\Gamma_{7(5)}$ and $\Gamma_{7(1)}$. For magnetic field perpendicular to *c*-axis, all valence band states are mixed. The matrix 6×6 describing giant Zeeman splitting of valence band for $B \perp c$-axis is given in Ref. 105. The direct influence of the magnetic field due to classical Zeeman effect and diamagnetic shift is usually small enough to be safely neglected. Following Ref. 93 we will introduce those effects in section 4.6.

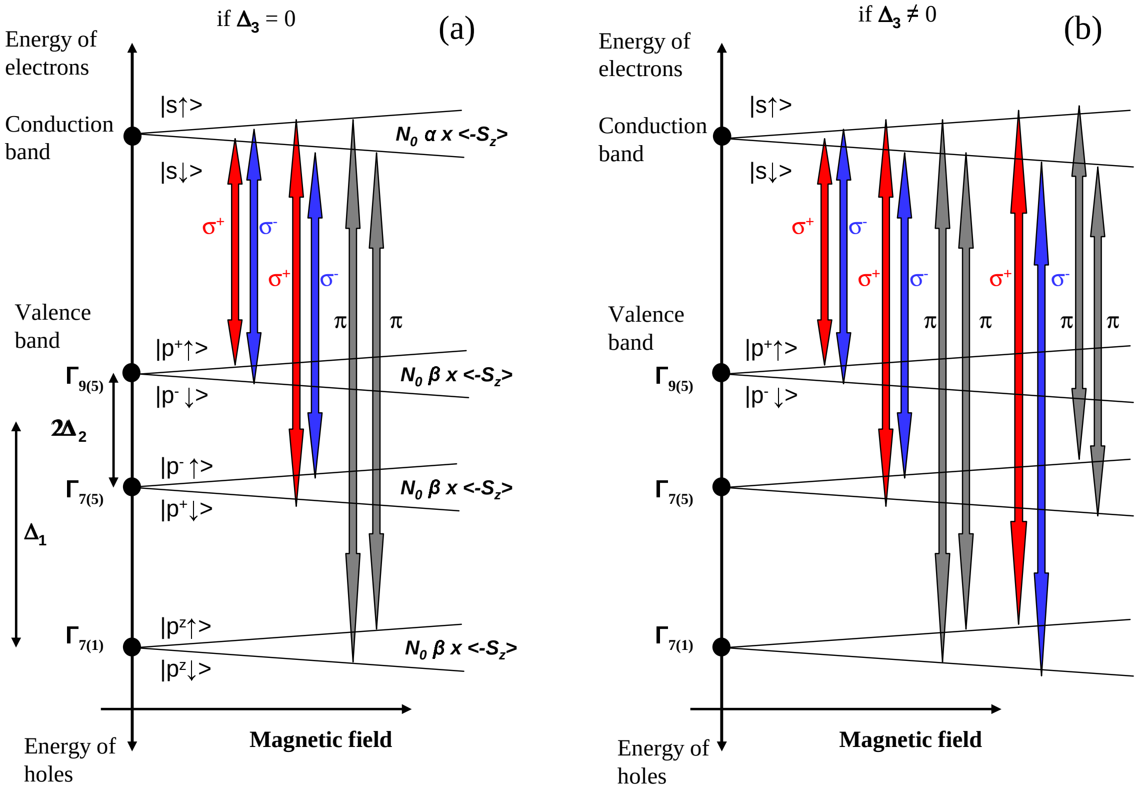

Figure 4.2: Scheme of splittings, wavefunctions, and allowed transitions in magnetic field parallel to c-axis, calculated using hamiltonians : (4.1), (4.2), and (4.3). Usual in wurtzite DMS sign of interactions is assumed : $\alpha > 0$, $\beta < 0$, $\tilde{\Delta}_1 > 0$, $\Delta_2 > 0$. (a) Scheme with simplification, $\Delta_3 = 0$. (b) Without simplification, so $\Delta_3 \neq 0$. Excitonic effects, which strongly affects energy and oscillator strength of optical transitions are not included here.

4.4 Band-to-band model of the Giant Zeeman splitting

Neglecting excitonic effects, one can calculate energy of optical transition by taking a simple sum of energy of the electron in the conduction bands (4.4) and energy of hole in the valence band [For $B \parallel c$: (4.5), (4.6) or (4.7)]. In this simplified model oscillator strength of transition depends on the wavefunctions in the valence and conduction bands and on the polarization of the photon. The corresponding selection rules are given in Table 4.2. They are illustrated in Fig. 4.2 for the case of magnetic field parallel to c-axis.

Wavefunction of the valence band is strongly anisotropic. Transitions involving $\Gamma_{9(5)}$ and $\Gamma_{7(5)}$ (A and B) states are polarized perpendicularly to c-axis ($E \perp c$), and transitions involving $\Gamma_{7(1)}$ (C) state are linearly polarized parallel to c-axis ($E \parallel c$). Mixing between $\Gamma_{7(5)}$ and $\Gamma_{7(1)}$ relaxes this selection rule. This is shown in the Fig. 4.2. There are six strong transitions in Fig. 4.2(a), and 4 additional, weaker transitions, which are allowed only if $\Delta_3 \neq 0$ (Fig. 4.2b). In CdS and CdSe, interband mixing is much stronger than in ZnO and GaN (see Δ_3 in Tab. 4.1) and consequently

	$\vert p^+\uparrow\rangle$	$\vert p^-\downarrow\rangle$	$\vert p^+\downarrow\rangle$	$\vert p^-\uparrow\rangle$	$\vert p^z\uparrow\rangle$	$\vert p^z\downarrow\rangle$
$\vert s\uparrow\rangle$	0	σ^-	σ^+	0	π	0
$\vert s\downarrow\rangle$	σ^+	0	0	σ^-	0	π

Table 4.2: Optical selection rules for transitions from the valence band to the conduction band in Γ point of wurtzite DMS. In the first row, there are basis wavefunctions for valence band. In the first column there are basis wavefunctions in the conduction band. Table elements show the polarization of the allow transition between given states. Zero means that the transition has zero oscillator strength because of spin conservation.

all 10 transitions shown in Fig. 4.2(b) have comparable oscillator strengths.

4.5 Giant Zeeman splitting of excitons

In wide gap DMS, giant Zeeman splitting of bands cannot be directly translated to the giant Zeeman splitting of excitons, as it usually done for CdS and CdSe based DMS.[68, 102, 105–108] Excitonic effects related to electron-hole exchange interactions have to be taken into account in calculation of the transition energy. It is particularly important for ZnO based DMS.

4.5.1 Electron-hole correlations

Excitons are bound complexes of electron and hole. Since there is only one electron subband, we will label excitons by the same labels as the valence band holes involved in the exciton (A, B, or C) independently on their symmetry. Electron-hole interaction within the exciton might be described by an effective spin hamiltonian :

$$H_{\mathrm{e-h}} = -R^* + 2\gamma\ \vec{\mathbf{s}}_e\vec{\mathbf{s}_h}, \tag{4.10}$$

where R^* is the binding energy, $\vec{\mathbf{s}}_e$ is the electron spin and $\vec{\mathbf{s}_h}$ the hole spin, and the electron-hole exchange[89, 93] is introduced by an exchange integral γ.

Both parameters, binding energy R^* and exchange integral γ, depend on the excitonic wavefunctions. However, a possible differences in the binding energies of the three excitons A, B and C are difficult to be distinguished from a change in the values of $\tilde{\Delta}_1$ or Δ_2 in Eq. (4.1). R^* is a binding energy of fundamental state, 1S exciton. Binding energy of excited states in hydrogen approximation decreases like $1/n^2$.

Electron hole exchange interaction mixes excitons and consequently affects both energy and oscillator strength of optical transitions. This effect is particularly important, if separation energy of two excitonic transitions is comparable to the energy of electron-hole exchange.

4.5.2 Excitonic hamiltonian

Finally, excitonic hamiltonian takes the following form :

$$H = E_0 + H_{\mathrm{v}} + H_{\mathrm{e-h}} + H_{sp-d}, \tag{4.11}$$

where E_0 is the band gap energy, H_{v} is hamiltonian of the hole in the valence band (4.1), $H_{\mathrm{e-h}}$ describes energy of electron-hole interaction within the exciton (4.10), and $H_{sp-d} = H_{p-d} + H_{s-d}$ describes exchange splitting due to s,p-d interactions (4.2) and (4.3) . In general, a basis of twelve excitons resulting from six hole states and two electron states has to be taken into account.

4.5.3 Giant Zeeman effect in Faraday configuration, $B \parallel k \parallel c$

We can limit ourselves to Γ_5 excitons optically active in σ polarization, if magnetic field is parallel to the c-axis and light incident along the same direction. In this configuration, we have no possibility to observe other 6 excitons (Γ_1, Γ_2, Γ_6), which are not optically active in σ polarization.

The hamiltonian (4.11) separates into two operators acting in two subspaces corresponding respectively to excitons active in the σ^+ and σ^- circular polarizations. For σ^+ we use the following basis wavefunctions : $|s \downarrow\ p^+ \uparrow\rangle$ and $|s \uparrow\ p^+ \downarrow\rangle$ (which are identically active in σ^+ polarization and will give the main contribution to excitons A and B), and $|s \uparrow\ p^z \uparrow\rangle$ (which is optically inactive since it is spin-forbidden, but will give the main contribution to exciton C in σ polarization). The same matrices, with opposite giant Zeeman terms, apply in σ^- polarization with the basis $|s \uparrow\ p^- \downarrow\rangle$, $|s \downarrow\ p^- \uparrow\rangle$, and $|s \downarrow\ p^z \downarrow\rangle$. In this basis the hamiltonian (4.11) can be written using following matrices :

$$H_v = \begin{pmatrix} -\Delta_2 & 0 & 0 \\ 0 & \Delta_2 & -\sqrt{2}\Delta_3 \\ 0 & -\sqrt{2}\Delta_3 & \tilde{\Delta}_1 \end{pmatrix}, \tag{4.12}$$

$$H_{e-h} = -R^* + \frac{\gamma}{2}\begin{pmatrix} -1 & 2 & 0 \\ 2 & -1 & 0 \\ 0 & 0 & 1 \end{pmatrix}, \tag{4.13}$$

$$H_{sp-d}^{\sigma\pm} = \pm\frac{1}{2} N_0\, x\langle -S_z\rangle \begin{pmatrix} \beta-\alpha & 0 & 0 \\ 0 & \alpha-\beta & 0 \\ 0 & 0 & \alpha+\beta \end{pmatrix}. \tag{4.14}$$

Diagonalizing the Hamiltonian gives the energy of the three excitons A, B and C in each circular polarization, as it is shown in Fig. 4.3(a). The corresponding oscillator strength marked by bars is deduced from the projection of the corresponding eigenvector, $|\psi\rangle$, onto the relevant subspace active in circular polarization : it is proportional to $|\langle s \downarrow p^{\pm} \uparrow |\psi\rangle + \langle s \downarrow p^{\pm} \uparrow |\psi\rangle|^2$, for $\sigma^{\pm}$ circular polarization, respectively.

In zero field, the relative position of the excitons is determined mainly by the trigonal component of the crystal field including strain $\tilde{\Delta}_1$ and the parallel spin-orbit interaction Δ_2. The giant Zeeman shift of the exciton is induced by s,p-d interactions. The electron-hole exchange interaction γ governs the mixing of the A and B excitons. It strongly alters the excitonic oscillator strength. The perpendicular spin orbit interaction (Δ_3) is responsible for the mixing between the B and C excitons.

As shown in Figs. 4.3(a,b), excitons A and B shift in opposite directions. They became more separate in σ^+ polarization in $\mathrm{Zn}_{1-x}\mathrm{Co}_x\mathrm{O}$ and in σ^- polarization in $\mathrm{Ga}_{1-x}\mathrm{Mn}_x\mathrm{N}$, whereas in the opposite polarizations they approach each other. For higher magnetization, exciton B interacts with exciton C due to the spin-orbit coupling (term Δ_3). In ZnO, the separation energy between excitons B and C is large and the experimental observation of the mixing between B and C excitons is difficult.

In $\mathrm{Zn}_{1-x}\mathrm{Co}_x\mathrm{O}$, A and B excitons anticross in σ^- circular polarization due to electron-hole exchange interaction. This anticrossing significantly decreases the giant Zeeman shift of excitons A and B. The same coupling in $\mathrm{Ga}_{1-x}\mathrm{Mn}_x\mathrm{N}$ is observed in σ^+ circular polarization and is significantly weaker. We should note that the corresponding A and B hole subbands cross freely [see Figs. 4.3(c,d)]. In $\mathrm{Zn}_{1-x}\mathrm{Co}_x\mathrm{O}$, the giant Zeeman shift of excitons A and B was found to be twice smaller than giant Zeeman shift of bands, $N_0(\alpha-\beta)\ x\langle -S_z\rangle$. The bars on the curves in Figs. 4.3 (a,b) are proportional to the oscillator strengths. In $\mathrm{Ga}_{1-x}\mathrm{Mn}_x\mathrm{N}$, the oscillator strengths of excitons A and B are almost equal at zero field. Exciton C is much weaker. In σ^- circular polarization, the coupling between excitons B and C increases and we observe a transfer of oscillator strength from exciton B to exciton C. Close to the anticrossing between excitons A and B, the upper excitonic line forms a bright exciton (with a large oscillator strength) and the lower one forms a dark exciton (with a small oscillator strength). Note that in all cases the total oscillator strength of A, B, and C remains constant.

Electron-hole exchange interaction is crucial in analyzing the results obtained for $\mathrm{Zn}_{1-x}\mathrm{Co}_x\mathrm{O}$. The oscillator strength is strongly affected by this interaction even in zero field. The observation of exciton C is rather difficult because of its very small oscillator strength.

Plotting Fig 4.3(a) we assumed a usual valence band ordering (Γ_9, Γ_7, Γ_7; $\Delta_2 > 0$) for ZnO, but a similar plot can be obtained using an unusual valence band ordering (Γ_7, Γ_9, Γ_7) by changing the sign of $N_0(\alpha-\beta)$. The C exciton is significantly affected by the sign of exchange integrals but its weak oscillator strength does not allow us to distinguish experimentally between the two possibilities.

An important result of above analysis is finding that the excitonic giant Zeeman splitting (A, B, or C) is not proportional to the magnetization, as it was usually assumed in the study of II-VI DMS. In order to probe the giant Zeeman energy $[N_0(\alpha-\beta)\ x\langle -S_z\rangle]$ in GaN based DMS, one should rather use the redshift of exciton A. It appears to be proportional to the magnetization as shown by the straight line in Fig. 4.3(b). Probing of the giant Zeeman energy in ZnO based DMS requires taking into account excitonic interactions in any case. Otherwise, exchange integrals will be underestimated.

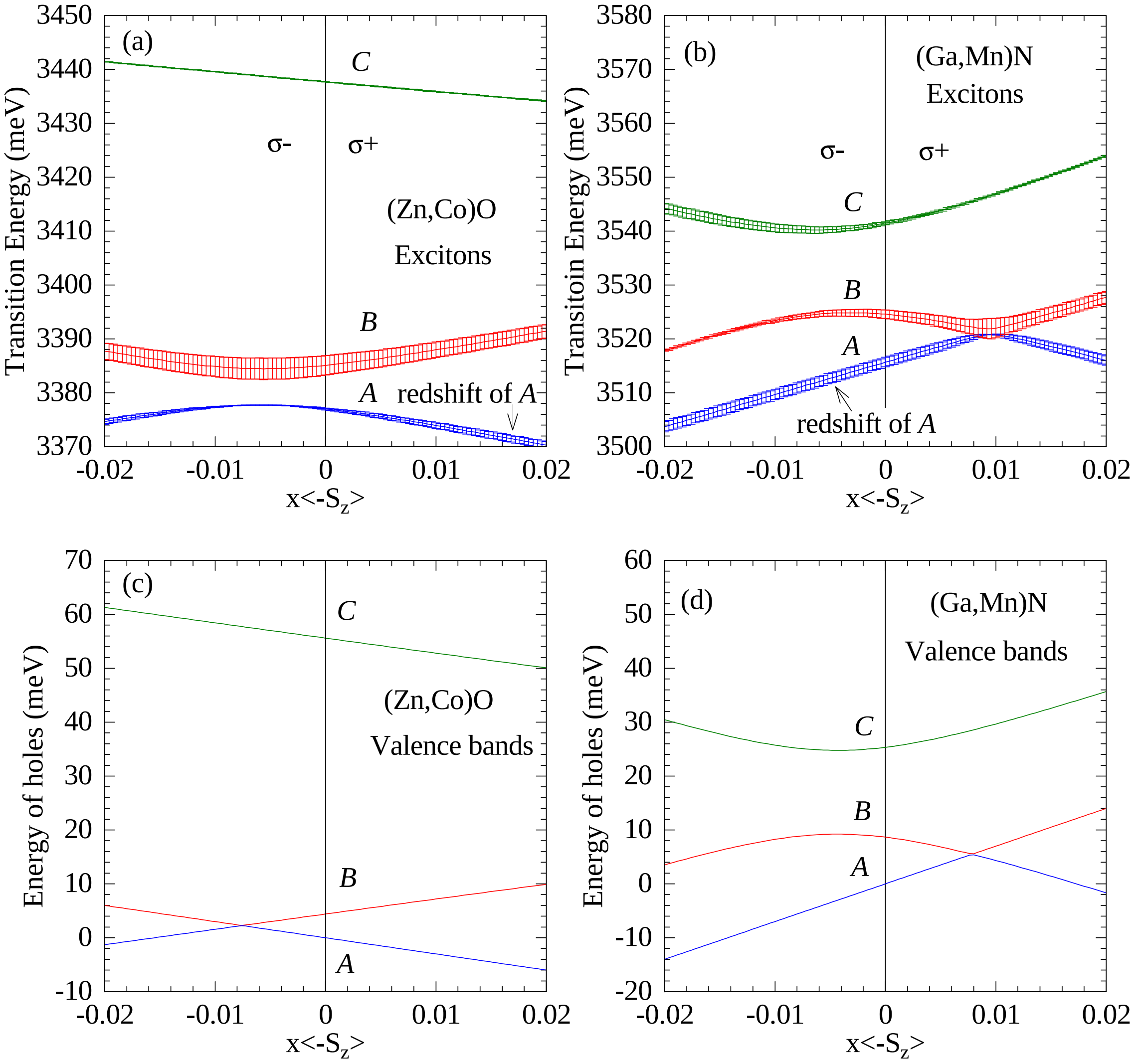

Figure 4.3: Results of calculation : (a,b) Energies of the A, B, and C excitonic transitions versus magnetization $x\langle -S_z \rangle$, for σ^- (left half) and σ^+ (right half) circular polarization. Bars show oscillator strength. (c,d) Energies of the A, B, and C valence band holes. Note that A and B valence bands cross, while an anticrossing occurs for A and B excitons. In this plot, we used a following set of parameters determined from preliminary analysis od our experimental data : $\tilde{\Delta}_1 = 51$ meV, $\Delta_2 = 3$ meV, $\Delta_3 = 6.3$ meV, $\gamma = 3.4$ meV, and $N_0(\beta - \alpha) = -0.8$ eV for $Zn_{1-x}Co_xO$ and $\tilde{\Delta}_1 = 13$ meV, $\Delta_2 = 7$ meV, $\Delta_3 = 5.5$ meV, $\gamma = 0.6$ meV, and $N_0(\beta - \alpha) = 1.2$ eV for $Ga_{1-x}Mn_xN$. We assumed a usual value of $N_0\alpha = 0.2$ eV for both materials.

4.5.4 Other configurations of magnetic field, crystal c-axis, and propagation vector

There are many interesting experimental configurations e.g. :

- $B \parallel c \perp k$ ($E \perp c$ and $E \parallel c$)
- $B \perp c \perp k$ ($E \perp c$ and $E \parallel c$)
- $k \parallel c \perp B$ ($E \perp B$ and $E \parallel B$),
- $B \parallel k \perp c$ (with complex polarization).

In comparison to the usual configuration $B \parallel k \parallel c$ (Sec. 4.5.3), we would need larger matrices in order to describe above configurations. Up to this moment, experiments in these configurations are rarely reported for wide gap DMS. More common experimental configuration is a measurement of polycrystals in Faraday configuration. Calculation of such an excitonic Giant Zeeman effect requires taking in to account that each microcrystal have different orientation. Thus, the angle between c-axis and magnetic field is different in each microcrystal.

4.6 Classical Zeeman splitting and diamagnetic shift

Magnetic field influences carriers and excitons in DMS by several means. Very strong, indirect influence due magnetic ions and s,p-d exchange interactions has been already discussed in sections 4.3 and 4.5. Direct influence of magnetic field due to the Zeeman effect and diamagnetic shift is usually much weaker and it is often neglected in interpretation of magnetooptical phenomena in DMS. However in very diluted materials they might play a significant role. Classical Zeeman splitting and diamagnetic shift do not require magnetic ions, so in principle they should be the same in host semiconductor and in the corresponding DMS e.g. in GaN and in $\mathrm{Ga}_{1-x}\mathrm{Fe}_x\mathrm{N}$.

Zeeman splitting

Following Luttinger[109] and Stępniewski *et al.*,[93] we present standard description of effects linear with magnetic field. The effective hamiltonian describing the Zeeman splitting of the conduction band electron is

$$H^{CB}_{\mathrm{Zeeman}} = g_e \mu_B \vec{\mathbf{B}} \vec{\mathbf{s}}_e, \tag{4.15}$$

and of the valence band hole it is

$$H^{VB}_{\mathrm{Zeeman}} = 2\mu_B \vec{\mathbf{B}} \vec{\mathbf{s}_\mathbf{h}} - \mu_B(3\tilde{\kappa}+1)\vec{\mathbf{B}}\vec{\mathbf{l}}, \tag{4.16}$$

where g_e is effective g factor of the electron, μ_B is Bohr magneton, $\vec{\mathbf{B}}$ is magnetic field, and $\vec{\mathbf{s}}_e$ is spin of the electron, $\vec{\mathbf{s}}$ and $\vec{\mathbf{l}}$ are spin and orbital momentum of the hole, respectively. Effective parameter $\tilde{\kappa}$ describes directly effective Landé g factor of hole in the Γ_9 state of nonmagnetic material. In the magnetic field parallel to the c-axis $6\tilde{\kappa} = g_{\Gamma_9\parallel}$. Calculation of the splittings of Γ_7 bands is more complex. These splittings depend on separation energy between $\Gamma_7(5)$ and $\Gamma_7(1)$, so they depend on all effects, which are changing this energy e.g. strain (see Hamiltonian 4.1). Calculation of the splitting of excitonic transitions requires additionally taking into account electron-hole exchange interactions, which can strongly affects excitonic Zeeman splitting.

Excitonic diamagnetic shift

Magnetic field induces change of the excitonic transition energy, which can be well approximated by simple quadratic dependence on magnetic field and by effective hamiltonian[93] :

$$H^X_{diam} = d\mathbf{B}^2 \tag{4.17}$$

Value of constant d depends not on material but also on the exciton properties. It increases with the exciton radius. Combined effect of the Zeeman splitting, diamagnetic shift and hamiltonian (4.11) will be discussed in Sec. 5.5, where these effects will be presented.

4.7 Calculation of reflectivity spectra

Excitons interacting with photons form particles called polaritons. This interaction is particularly important for the interpretation of optical spectra of semiconductors with large excitonic oscillator strength, such as ZnO, where the longitudinal-transverse splitting is equal to several meV.[110] Thus it is larger than excitonic linewidth. However, polaritonic effects have also been reported for high quality crystals with weaker excitonic transitions : CdS,[111,112] ZnTe,[112] and GaN.[113] Generally, a polaritonic model is useful for description of sharp lines which appear in reflectivity spectra near strong optical transitions with weak broadening. In diluted magnetic semiconductors broadening increases with dopant concentration, so in many cases, polariton corrections to the optical spectra can be safely neglected.

4.7.1 Reflectivity spectra with 2 excitons-polaritons

We present here the details of the polariton model used to fit reflectivity spectra of A and B excitons separated by only a few meV in wide gap semiconductors. In the model the strong coupling between excitons and photons is taken into account. The dielectric function and reflectivity spectra near excitonic resonances are described in details by Hopfield and Thomas[112] and by Lagois.[110,111] The dispersion of the polariton branches associated with a propagation of the light parallel to the c-axis was calculated by solving of the following equations (4.18) and (4.19) :

$$\begin{aligned}\epsilon(k,\omega) = \epsilon_\infty &+ \frac{4\pi\alpha_{0A}\omega_A^2}{\omega_A^2 - \omega^2 + (\hbar k^2\omega_A/m^*) - i\omega\Gamma_A} \\ &+ \frac{4\pi\alpha_{0B}\omega_B^2}{\omega_B^2 - \omega^2 + (\hbar k^2\omega_B/m^*) - i\omega\Gamma_B},\end{aligned} \tag{4.18}$$

$$\epsilon(k,\omega) = k^2c^2/\omega^2. \tag{4.19}$$

where ϵ_∞ is the background dielectric constant, $\alpha_{0A,B}$ are the polarizabilities, $\Gamma_{A,B}$ are damping parameters, $\omega_{A,B}$ are the energies of excitonic transitions, and m^* is the effective mass of excitons.

We note ϵ_1, ϵ_2, ϵ_3 the three solutions of (4.18) and (4.19). For each solution, we can determine the associated refractive index $n_i = \sqrt{\epsilon_i}$, the wave vector $k_i = n_i\omega/c$. We define :

$$\epsilon_i^{A,B} = \frac{4\pi\alpha_{0A,B}\omega_{A,B}^2}{\omega_{A,B}^2 - \omega^2 + (\hbar k_i^2\omega_{A,B}/m^*) - i\omega\Gamma_{A,B}} \tag{4.20}$$

The reflection coefficient was derived from the surface boundary conditions for electric field (4.21), magnetic field (4.22) and the total polarization of A (4.23) and B (4.24) excitons :

$$E_I + E_R = E_1 + E_2 + E_3, \tag{4.21}$$

$$E_I - E_R = n_1E_1 + n_2E_2 + n_3E_3, \tag{4.22}$$

$$\epsilon_1^AE_1 + \epsilon_2^AE_2 + \epsilon_3^AE_3 = 0, \tag{4.23}$$

$$\epsilon_1^BE_1 + \epsilon_2^BE_2 + \epsilon_3^BE_3 = 0. \tag{4.24}$$

Here, E_I is the electric field amplitude of incoming light, E_R is the corresponding amplitude for reflected light, E_1, E_2 and E_3 are the electric field amplitudes of the three polaritons propagating inside the sample. From (4.23) and (4.24), we get :

$$\frac{E_2}{E_1} = \frac{\epsilon_1^B\epsilon_3^A - \epsilon_1^A\epsilon_3^B}{\epsilon_2^A\epsilon_3^B - \epsilon_2^B\epsilon_3^A} \tag{4.25}$$

and

$$\frac{E_3}{E_1} = \frac{\epsilon_1^B\epsilon_2^A - \epsilon_1^A\epsilon_2^B}{\epsilon_3^A\epsilon_2^B - \epsilon_3^B\epsilon_2^A}. \tag{4.26}$$

Next, we get an effective refractive index $n^\dagger$

$$n^\dagger = \frac{E_I - E_R}{E_I + E_R} = \frac{n_1 + n_2\frac{E_2}{E_1} + n_3\frac{E_3}{E_1}}{1 + \frac{E_2}{E_1} + \frac{E_3}{E_1}} \tag{4.27}$$

From the expression for $n^\dagger$, we can calculate the reflection coefficient of the material $R = |\frac{n^\dagger-1}{n^\dagger+1}|^2$, which takes into account the presence of the polariton branches. However, it is commonly assumed that the formation of excitons is not possible within a few nanometers close to the surface. A dead (exciton-free) layer of thickness d (about 4 nm), and a background refractive index $n = \sqrt{\epsilon_0}$ is usually added to the model. The reflectivity of the bilayer structure leads to an effective refractive index given by :

$$n^* = n\left[\frac{(n^\dagger + n)e^{ikd} - n + n^\dagger}{(n^\dagger + n)e^{ikd} + n - n^\dagger}\right] \tag{4.28}$$

Finally, the reflectivity spectra are given by :

$$R = \left|\frac{n^* - 1}{n^* + 1}\right|^2 \tag{4.29}$$

Examples of the fits of the reflectivity spectra of ZnO and $Zn_{1-x}Co_xO$ epilayers are shown in Fig. 5.3.

In the above model we assume that only 1S excitons A and B contribute to the reflectivity spectra. However, even in spectral region very close to excitons A and B, the reflectivity spectra are slightly modified by additional non-resonant absorption. For $Zn_{1-x}Co_xO$, we obtained a better fit of the experimental spectra by adding an imaginary part $i\epsilon'$ to the background dielectric constant ϵ_∞ in Eq. (4.18). This is only an approximation, more realistic fit requires taking take into account transitions described in next section : excited states and transitions to continuum of states.

4.7.2 Optical effect of excited states

In order to improve our model of reflectivity, we followed Stępniewski *et al.*,[113] and we replace the background dielectric function ϵ_∞ by the residual dielectric function $\epsilon^*(\omega)$. This new dielectric function depends on the photon energy. Using $\epsilon^*(\omega)$ we take into account additional contributions which are expected to exhibit no significant polariton effects[113] : exciton C, excited states of A, B and C[113,114] which are optically active (S-states), and transitions to the continuum of unbound states.[115] Hence

$$\epsilon^*(\omega) = \epsilon_0^* + \frac{4\pi\alpha_{0C}\omega_C^2}{\omega_C^2 - \omega^2 - i\omega\Gamma_C} + \sum_{j=A,B,C}\left(\sum_{n=2}^{\infty}\frac{4\pi\alpha_{0j}}{n^3}\frac{\omega_{n,j}^2}{\omega_{n,j}^2 - \omega^2 - i\omega\Gamma_{n,j}} + \epsilon_{j,\mathrm{ub}}\right) \tag{4.30}$$

Here ϵ_0^* is background dielectric constant. It is smaller than ϵ_∞, because contribution from many transitions will be taken into account explicitly. Next, α_{0j}, $\omega_j = E_j/\hbar$, and Γ_j are the polarizability, resonant frequency, and damping rate of each exciton A, B, and C. Resonant energies of the excited states n are $\hbar\omega_{n,j} = E_j + R_j^* - R_j^*/n^2$, where R_j^* are the effective Rydbergs. The corresponding damping parameters are calculated by using an empirical formula,[116,117]

$$\Gamma_{n,j} = \Gamma_\infty - (\Gamma_\infty - \Gamma_j)/n^2, \tag{4.31}$$

with one common damping rate Γ_∞. Finally, the contribution $\epsilon_{j,\mathrm{ub}}$ from unbound states is given in Eq. 5 of Ref. 115, with the damping parameter $\Gamma_\infty/2$ and the amplitudes $\mathtt{A}_j$ determined by the exciton polarizabilities α_{0j} (see Refs 118 and 113) :

$$\mathtt{A}_j = 4\pi\alpha_{0j}\,\frac{(E_j)^3}{8(R_j^*)^{3/2}} \tag{4.32}$$

Significant advantage of described residual dielectric function is that it very well describes reflectivity in wide range (as wide as 100 meV, see reflectivity spectra of $Ga_{1-x}Fe_xN$ in Sec. 5.5 or $Zn_{1-x}Mn_xO$ in Sec. 5.12), it describes effect of broadening, and it allows to describe properly exciton C which overlap with the excited states of excitons A and B.

4.7.3 Parameters of reflectivity model

We presented two models of reflectivity spectrum : polariton model for two excitons (Sec. 4.7.1) and model of dielectric function, which takes into account all allowed optical transitions (Sec. 4.7.2). These models can be used together or separately.

In order to fit ZnO and $Zn_{1-x}Co_xO$, we used only the polariton model with 1S excitons A and B (Sec. 4.7.1). It was reasonable to neglect excited states, because 1S and 2S excitonic lines A and B do not overlap in ZnO. We used both models (Sec. 4.7.1 and 4.7.2) in order to describe reflectivity spectra of $Zn_{1-x}Mn_xO$ and $Ga_{1-x}Fe_xN$ samples, which exhibit particularly sharp excitonic lines. In order to fit $Ga_{1-x}Mn_xN$ with very broad excitonic lines, we didn't use polariton model, only dielectric function related to all allowed transition (Sec. 4.7.2). Table 4.3 gives values of constants, that we used to described our reflectivity spectra. Examples of fitting parameters such as exciton transition energies, polarizabilities, and damping parameters are given in Tab. 5.4 (Sec. 5.5.1) for GaN and in Fig. 5.17 for diluted $Zn_{1-x}Mn_xO$ (Sec. 5.3.2).

Host	ϵ_∞	ϵ_0^*	m^*	R_A^*	R_B^*	R_C^*
ZnO	6.2[a]	3.6[b]	0.87 m_e[c]	60 meV[d]	60 meV[d]	60 meV[d]
GaN	9.2[e]	5.2[f]	m_e[f]	25.2 meV[g]	21.9 meV[g]	26.5 meV[h]

[a] Segall, Ref. 119.
[b] We determined this value by fitting spectra of diluted $Zn_{1-x}Mn_xO$.
[c] Hümmer, Ref. 120.
[d] For all three excitons we used one value, determined by Reynolds *et al.*, Ref 96.
[e] Value determined by Kornitzer *et al.*, Ref 117. Actually, we didn't need this value.
[f] Stępniewski *et al.*, Ref. 113.
[g] We determined this value by fitting spectra of GaN.
[h] Kornitzer *et al.*, Ref 117.

Table 4.3: Parameters used in this work for description of reflectivity spectra of ZnO and GaN based DMS.

Chapter 5

Exciton spectroscopy (experimental results)

This chapter is devoted to reflectivity, absorption and photoluminescence measurements performed near energy gap of ZnO and GaN based DMS. It presents a detailed analysis of magnetooptical spectra and description of the excitonic giant Zeeman effect observed for various wide gap DMS with small concentration of magnetic ions. This analysis leads to the determination of effective s,p-d exchange integrals of $Zn_{1-x}Co_xO$*,* $Zn_{1-x}Mn_xO$*,* $Ga_{1-x}Mn_xN$*, and* $Ga_{1-x}Fe_xN$*. Then, we discuss observation of near-gap magnetic circular dichroism in layers with a larger magnetic ions content. Additionally, we present preliminary results of the photoluminescence of* $Zn_{1-x}Mn_xO$*.*

Ce chapitre est dédié aux mesures de réflectivité, d'absorption et de photoluminescence réalisées au voisinage des énergies de bandes interdites de ZnO et GaN. Nous présentons une analyse détaillée des spectres magnéto optiques ainsi que de l'effet Zeeman géant des excitons, observé pour les divers échantillons ayant une faible concentration en ions magnétiques. Cette analyse nous conduit à la détermination des intégrales d'échange s,p-d effectives des différents matériaux étudiés $Zn_{1-x}Co_xO$*,* $Zn_{1-x}Mn_xO$*,* $Ga_{1-x}Mn_xN$ *et* $Ga_{1-x}Fe_xN$*. Enfin, nous discutons le dichroïsme circulaire magnétique pres de l'énergie de bande interdite pour les échantillons avec une concentration plus élevée en ions magnétiques et nous présentons quelques résultats préliminaires de photoluminescence de* $Zn_{1-x}Mn_xO$*.*

5.1 Introduction

Observation of excitons in wide gap DMS is very challenging. Tens of scientific groups around the world have access to samples of ZnO or GaN based DMS and to advanced optical experimental setups, but for our best knowledge, nobody except author and his coworkers[34–40,60] has observed well resolved excitons coupled to the system of magnetic ions introduced to ZnO or GaN. Difficulty lays in a choice of experimental techniques, quality of samples, time consuming characterization and sufficient experience required to find a good conditions for observation of excitonic effects. The author of this work performed his magnetooptical experiments in laboratories with long tradition of magnetooptical study of DMS. The novelty of present study was related to the spectral range of interest. Excitonic lines of ZnO and GaN are observed in UV part of the spectra. Therefore, it was necessary to equip our labs in new UV waveplates, crystal polarizers and high pressure Xe lamps. Moreover, efficient study of Co^{2+} and Mn^{3+} in wide gap DMS requires magnetic field high enough to saturate magnetization (at least $B = 7$ T, but $B = 11$ T was also very useful). Our first successful magnetooptical results motivated technology groups to produce samples especially for us. After characterization of more than 100 samples, it is clear for us that observation of exchange splitting of excitons is the most probable in about 1 μm thick epitaxial layers (MBE or MOCVD) with c-axis parallel to growth axis, concentration about 0.5%, in Faraday configuration, using reflectivity measurements. In thinner layers, reflectivity signal of excitons can be strongly affected by interferences. However, in thin samples observation of excitons in absorption is also realistic. Samples thicker than 1 μm are very good for reflectivity, particularly if one can be sure that they have homogeneous distribution of magnetic ions in depth. Otherwise, determination of the concentration of magnetic ion becomes complex. It is also important to avoid buffer layers with energy gap smaller than energy gap of magnetic layer, otherwise strong absorption of buffer layer can affects excitonic spectra of DMS. Following this suggestions, observation of effects presented in this chapter should be not very complicated.

This chapter is the largest and the most important in this work. It is organized in the following way : there are four sections related to four investigated materials : $Zn_{1-x}Co_xO$, $Zn_{1-x}Mn_xO$, $Ga_{1-x}Mn_xN$, and $Ga_{1-x}Fe_xN$. On the beginning of each section, the zero-field results are presented, as well as information about magnetic field effects not related to magnetic ions. Then, there are main magnetooptical results which allow us to perform a quantitative analysis of the effect of s,p-d exchange interactions. Next, additional results, with more qualitative analysis are shown. Sections are ended with discussion devoted to magnetic properties of the material and to the determination of exchange integrals. In this chapter, we do not discuss all the detail of our exciton and polariton models, which has been presented in previous chapter, we make only references to the part of the model with are crucial for understanding of presented phenomena.

5.2 Spectroscopy of $\mathrm{Zn}_{1-x}\mathrm{Co}_x\mathrm{O}$

5.2.1 Zero field reflectivity

Reflectivity of undoped ZnO layer is shown in the Fig. 5.1. Three excitonic features can be observed in the upper spectrum. These three excitons are typical for the semiconductor of wurtzite structure. They are labeled : A, B, and C. At the bottom spectrum, only A and B excitonic features can be observed. The upper spectrum was measured with the c-axis of the wurtzite crystal tilted by an angle of 45 degrees with respect to the optical axis of experimental setup. The bottom spectrum was measured in our usual configuration, with light perpendicular to the surface of the sample. Since c-axis is perpendicular to the surface of our samples, in our usual configuration light is parallel to the c-axis ($k \parallel c$), so electric field of incoming light is perpendicular to the c-axis ($E \perp c$, σ polarization). If spin orbit interaction is weak comparing to crystal field [$\Delta_3 << (\Delta_1 - \Delta_2)$, see section 4.3], exciton C has weak oscillator strength in σ polarization. This explain lack of feature related to exciton C at the bottom spectra. Optical selection rules for excitons has been already explained in Section 4.4, Fig. 4.2, and Table 4.2.

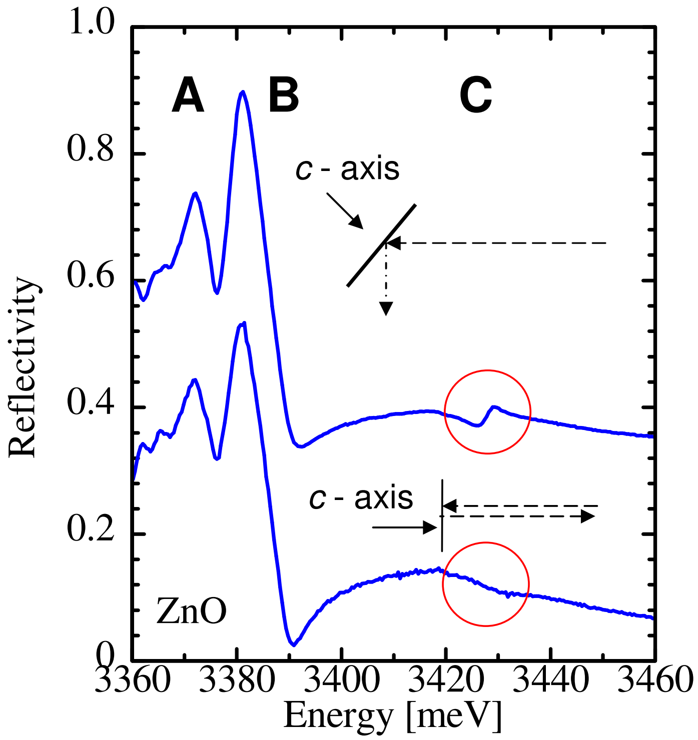

Figure 5.1: Reflectivity spectra of ZnO measured at $T = 1.6$ K with incidence angle of 45 degrees (upper spectrum, combination of σ and π polarization) and with normal incidence (bottom spectrum, pure σ polarization). Three excitonic features are labeled A, B, and C. Exciton C disappears at the bottom spectrum because of weak spin orbit coupling and the optical selection rules (see Sec. 4.4). Sample ♯Z176.

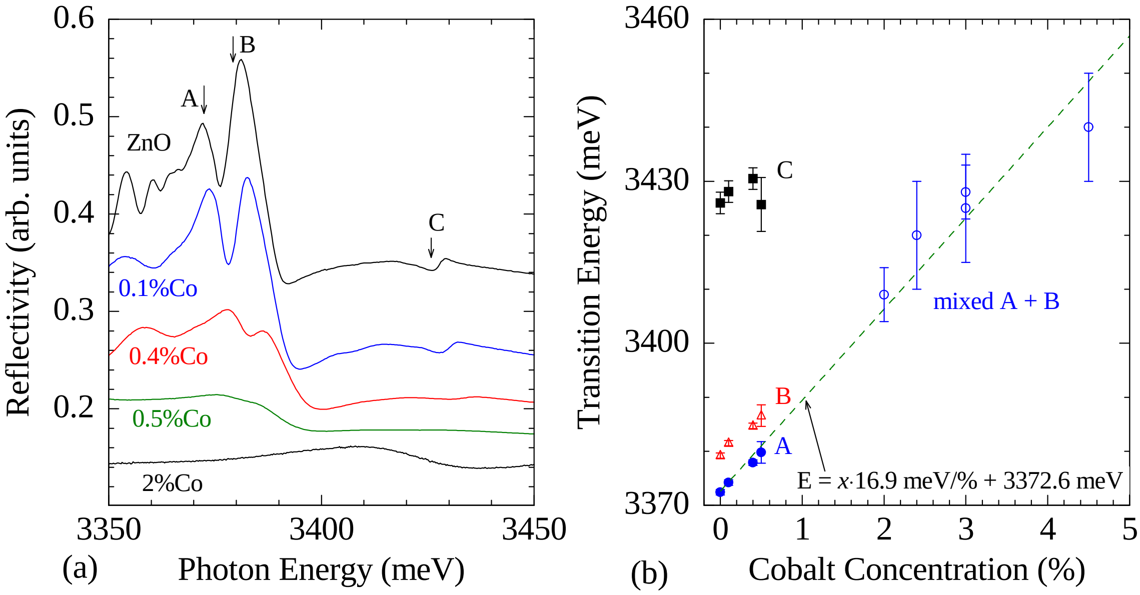

Figure 5.2: (a) Reflectivity spectra measured at $T = 1.6$ K with incidence angle of 45 degrees. The topmost spectrum is for ZnO (sample ♯Z176), other spectra for $\mathrm{Zn}_{1-x}\mathrm{Co}_x\mathrm{O}$ with increasing Co concentration, $x = 0.1\%$ (♯Z158), 0.4% (♯Z159), 0.5% (♯Z227), 2% (♯Z219). Labels A, B, and C identify the three excitons which are visible in ZnO and at low Co content ; Fabry-Perot oscillations are also observed at low photon energy. (b) Spectral positions of the excitonic transition in ZnO and $\mathrm{Zn}_{1-x}\mathrm{Co}_x\mathrm{O}$. Symbols marked as "mixed A+B" means that in the case of samples with a Co concentration higher than 2% we cannot resolve excitons A and B, and we plot the position of a broad structure. The dashed line shows the linear fit for the position of exciton A as a function of Co content.

Reflectivity of ZnO and $\mathrm{Zn}_{1-x}\mathrm{Co}_x\mathrm{O}$ layers is shown in the Fig. 5.2(a). Concentration of Co varies from 0.1% up to 2%. In order to observe all three excitons, all the spectra shown in this figure were measured in the configuration with the sample tilted by an angle of 45 degrees with respect to the optical axis. Three excitons can be resolved for ZnO and for more diluted samples, but the broadening of the excitonic features increases with x. As a result, the excitons cannot be resolved for concentration $x \geq 2\%$. We determined energy position of excitons A and B using the polariton formalism described in the section 4.7.1. Approximate energy position of exciton C was determined by pointing characteristic structure in the spectra, as it is shown by the arrow in Fig. 5.2(a). We observe a systematic increase of the excitonic transition energies with the Co concentration in all studied samples [Fig. 5.2(b)]. The energy of exciton A follows linear dependence. It is marked by a dashed line in Fig. 5.2(b), which indicates an increase of the energy gap of $\mathrm{Zn}_{1-x}\mathrm{Co}_x\mathrm{O}$ with x, about 17 meV/%. In samples with sharp excitonic lines ($x = 0, 0.1, 0.4\%$), the energy differences between the excitonic lines in zero field are $E_B - E_A = 7 \pm 1$ meV and $E_C - E_B = 47 \pm 3$ meV.

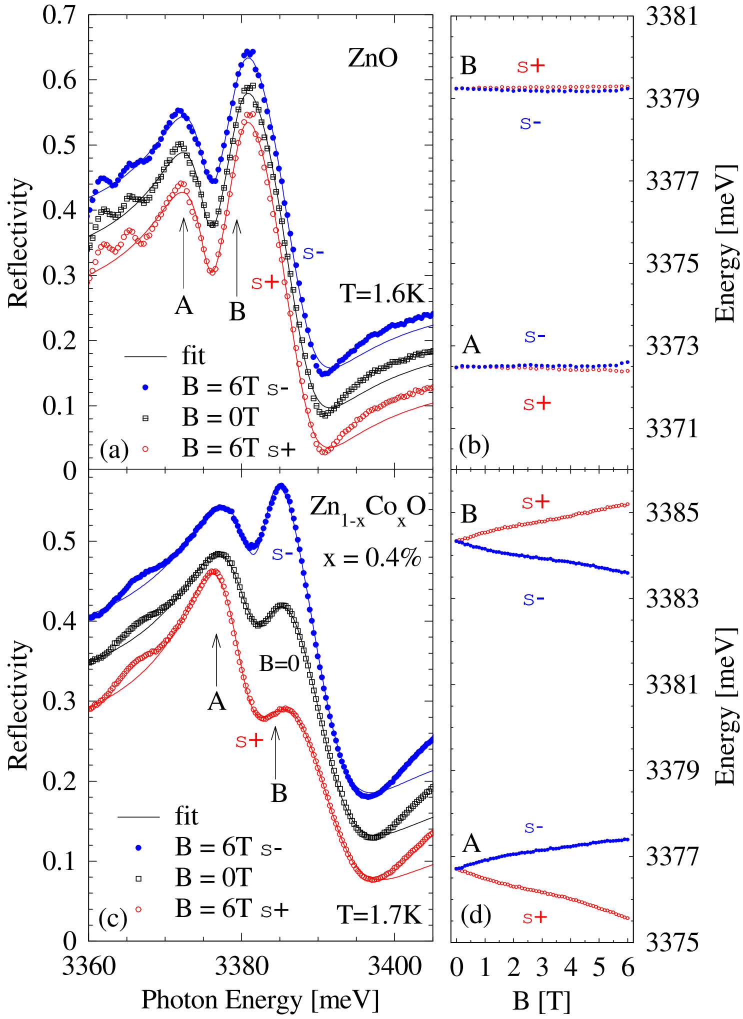

Figure 5.3: (a) Reflectivity spectra of ZnO (sample ♯Z176) at $B = 0$ T and at $B = 6$ T in σ^+ and σ^- circular polarizations (symbols). The positions of excitons A and B, as determined from the fit of the $B = 0$ T spectrum (solid line), are marked by arrows. The Zeeman effect induces a small, opposite shift of the two excitons. (b) The position of excitons A and B in ZnO, as determined from a fits of the reflectivity spectra shown in (a). (c) Reflectivity spectra of $Zn_{0.996}Co_{0.004}O$ (sample ♯Z159) at $B = 0$ T, and $B = 6$ T in σ^+ and in σ^- polarizations. Solid lines are the fits to the spectra. (d) The position of excitons A and B, versus magnetic field. At $B = 6$ T, the value of the splitting is -1.8 meV for exciton A and 1.6 meV for exciton B.

5.2.2 Zeeman effect and diamagnetic shift in ZnO

Fig. 5.3 (a) shows reflectivity spectra of ZnO measured in Faraday configuration. The transition energies of both excitons A and B and the corresponding values of the Zeeman splitting [Fig. 5.3 (b)] were obtained using a model of reflectivity with two excitons-polaritons, as it is described in Sec. 4.7.1. We used a two-step procedure. First, the whole set of parameters (polarizability $\alpha_{0A,B}$, position $\omega_{A,B}$, width $\Gamma_{A,B}$, the dead layer thickness d, and the non resonant absorption contribution $i\epsilon'$) were determined by fitting the zero field spectra. Then, the spectra under magnetic field were fitted by adjusting only five parameters : $\omega_{A,B}$, $\Gamma_{A,B}$, and the relative polarizability of excitons A and B (keeping constant the sum $\alpha_{0A} + \alpha_{0B}$).

We did not observe any excitonic diamagnetic shift, as expected due to the small excitonic Bohr radius ($R_X = 1.8$ nm) in ZnO.[121] The diamagnetic shift is smaller than 0.1 meV at $B = 6$ T, so the corresponding parameter d in Eq. (4.17) is smaller than 3 μeV$/T^2$. The Zeeman splitting of excitons A and B also remains very small, about 0.1 meV at $B = 6$ T. This value corresponds to an effective excitonic

Landé factor less than 0.3. Such a small value of the Landé factors for the allowed excitonic transitions in ZnO has been already reported for the Voigt configuration by Blattner *et al.*,[121] and more recently by Reynolds *et al.*[96] Our experiments were performed in the Faraday configuration with resolved circular polarizations and they confirm unambiguously the previous observations.[96, 121] Unfortunately, we do not use magnetic field high enough to reach an experimental precision sufficient to determine the parameters describing Zeeman effect : Luttinger parameter $\tilde{\kappa}$ [see Eq. (4.16)] and effective g-factor of electron [see Eq. (4.15)].

5.2.3 Giant Zeeman effect

In samples doped with cobalt ions, we observe an enhancement of the excitonic Zeeman splitting [Fig. 5.3, compare (c,d) with (a,b)]. The Zeeman splitting of excitons A and B is almost opposite. It increases with the Co concentration [Fig. 5.4], and decreases with temperature : Fig. 5.5 shows the Zeeman splitting of excitons A and B as a function of the magnetic field up to 11 T, at three temperatures : 1.7, 7 and 20 K. A saturation appears at the lowest temperature and the highest magnetic field. The Zeeman splitting is proportional to the mean spin projection calculated for isolated Co ions using Eq. (3.8) in Section 3.6.1.

This enhancement of the Zeeman splitting which increases with the cobalt content, and its proportionality to the Co magnetization, is essential for the following study. Further, enhanced Zeeman splitting will be labeled giant Zeeman splitting. It will be analyzed as a consequence of s,p-d exchange interactions. First, we will use simplified model which neglect excitonic effects described in Sec. 4.5.1. This will allow us to parameterize ion-exciton coupling. Second, we will use more advanced, excitonic model, which will allow us to conclude about coupling between magnetic ions and free carriers.

Ion-exciton coupling

In order to understand the origin of observed excitonic shifts, we performed a simplified analysis. We based on band-to-band model (Sections 4.3 and 4.4), which neglect electron-hole exchange interaction (Sec. 4.5.1), we neglected Zeeman effect and diamagnetic shift of ZnO. In such a case the energy of the transitions from $\Gamma_{9(5)}$ valence band in $\sigma^{\pm}$ circular polarization are given by sum of (4.4) and (4.5) :

$$E^{\sigma\pm}_{X\Gamma_{9(5)}} = E_0 \mp G_e - \Delta_2 \pm G_h. \tag{5.1}$$

A further simplification is based on fact, that despite sharp A and B excitonic features, we do not observe any feature related to C exciton ($\Gamma_{7(1)}$) in the configuration $k \parallel c$. It suggests very weak spin-orbit coupling in ZnO [$\Delta_3 << (\Delta_1 - \Delta_2)$, see section 4.3]. Hence, we can simplify the sum of (4.4) and (4.6), and we obtain the approximate energy of transitions from $\Gamma_{7(5)}$ valence band:

$$E^{\sigma\pm}_{X\Gamma_{7(5)}} = E_0 \pm G_e + \Delta_2 \mp G_h. \tag{5.2}$$

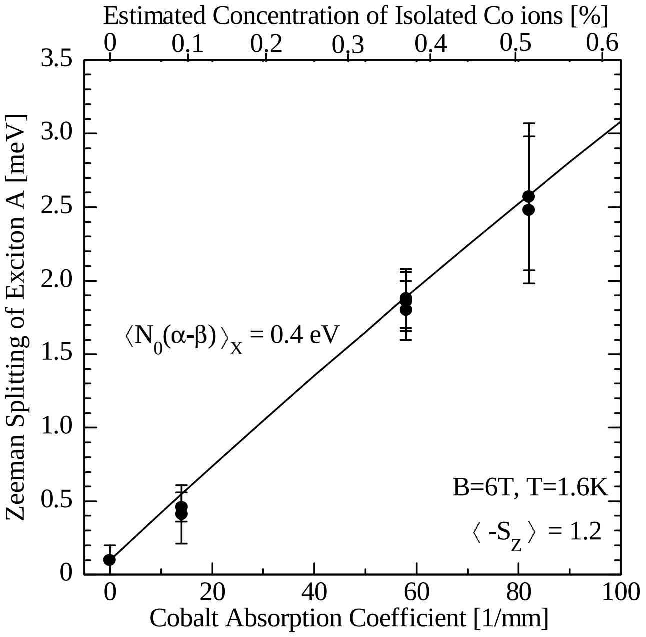

Figure 5.4: Zeeman splitting of exciton A, measured at $B = 6$ T and $T = 1.6$ K, so that the mean spin of isolated Co is $\langle S_z \rangle = 1.2$ [Eq. (3.8)]. The horizontal scale (bottom scale) is the absorption coefficient of the $^4A_2 \rightarrow {}^2E2\overline{A}$ transition of Co (see Fig. 3.2). The top scale (nonlinear) displays the density of free spins x_{eff} expected for a random distribution of Co on the Zn sublattice. The solid line shows the giant Zeeman splitting $N_0|\beta - \alpha|_X \times x_{eff} \times \langle\text{-}S_z\rangle$ calculated with an effective $N_0|\beta - \alpha|_X = 0.4$ eV.

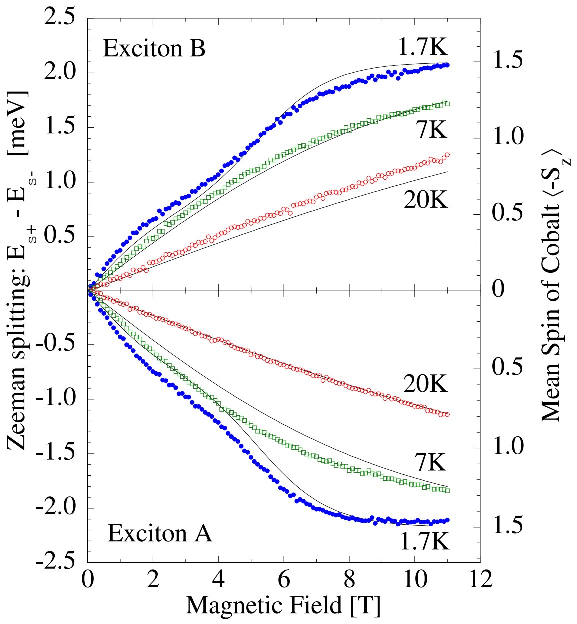

Figure 5.5: Dots and left axis : Zeeman splitting of excitons A and B measured at three temperatures. Lines and right axis : mean spin of isolated Co ions as given by Eq. (3.8). The left and right scales are chosen so that $N_0|\beta - \alpha|_X = 0.40$ eV for exciton A and 0.39 eV for B, calculated with $x_{eff} = 0.36\%$. Sample $\sharp$Z159.

Such a simplification leads to opposite giant Zeeman splittings for the two optically active excitons : $E^{\sigma+}_{X\Gamma_{9(5)}} - E^{\sigma-}_{X\Gamma_{9(5)}} = -(E^{\sigma+}_{X\Gamma_{7(5)}} - E^{\sigma-}_{X\Gamma_{7(5)}}) = 2(G_h - G_e) = N_0(\beta - \alpha)x_{eff}\langle\text{-}S_z\rangle$. This is what we observe experimentally (Figs 5.3 and 5.5). The important consequence is that the α and β exchange integrals cannot be determined independently from this experiment, only their difference can be obtained.

The circular polarization of the giant Zeeman splitting can be used to determine the sign of exchange integral difference $\beta - \alpha$. If valence band order in ZnO is usual one ($\Gamma_{9(5)}$, $\Gamma_{7(5)}$, $\Gamma_{7(1)}$), $E_{X\Gamma_{9(5)}}$ corresponds to energy of exciton A, and $E_{X\Gamma_{7(5)}}$ corresponds to energy of exciton B. Then, shift of exciton A to low energy in σ^+ circular polarization, implies a negative sign of $\beta - \alpha$ (as usually observed in II-VI DMSs, where $\beta < 0$ and $\alpha > 0$).

However, if the valence band order in ZnO is $\Gamma_{7(5)}$, $\Gamma_{9(5)}$, $\Gamma_{7(1)}$, therefore it is different than in other wurtzite semiconductors, we conclude that the energy of exciton A is given by $E_{X\Gamma_{7(5)}}$, and the energy of exciton B is given by $E_{X\Gamma_{9(5)}}$. In such a case, the shift of exciton A to low energy in σ^+ circular polarization, implies a positive sign of $\beta - \alpha$, different from usually observed in II-VI DMSs.

Using a model which neglect interaction with exciton C, we cannot distinguish between two above cases, so we can estimate only an absolute value, $N_0|\beta - \alpha|$. In our diluted samples ($x \leq 0.5\%$), we estimated this magnitude of the exchange integral difference using the optically active excitons, $N_0|\beta - \alpha|_X = 0.4$ eV [Fig. 5.4]. We add $_X$ in order to emphasize that we determined here the parameter describing the giant Zeeman splitting of excitons, so the magnitude of the ion-exciton coupling. We will show, that due to electron-hole exchange interaction, the splitting of excitons is not a simple sum (or difference) of the splitting of the conduction and valence bands. Therefore, $N_0|\beta - \alpha|_X$ does not directly describe ion-carrier coupling.

s,*p*-*d* and electron-hole exchange interactions

We now include the effect of the electron-hole exchange interaction. We will show that the difference of the effective exchange integrals $N_0(\beta - \alpha)_X$, observed by the excitons can be much smaller than the difference of the exchange integrals for free carriers, $N_0(\beta - \alpha)$. Our description is based on hamiltonian (4.11). The position of the three excitons A, B, C, which might be optically active from symmetry considerations, is obtained by digitalization of a 3×3 matrix, which is a sum of 4.12 (hamiltonian of valence band), 4.13 (hamiltonian of electron-hole interactions), and 4.14 (hamiltonian of *s*,*p*-*d* interactions). These matrices lead to mixing of the two electron-hole states active in σ^+ ($|s\downarrow\ p^+\uparrow\rangle$ and $|s\uparrow\ p^+\downarrow\rangle$) and dark electron-hole state ($|s\uparrow\ p^z\uparrow\rangle$. Active electron-hole states give rise to excitons A and B, and dark electron-hole state gives rise to exciton C.

The effect of the electron-hole exchange within the exciton, which mixes the A and B excitons active in a given circular polarization is the most important for the present study. If spin-orbit coupling (Δ_2) dominates over exchange (γ), then one observes excitons formed of pure electron-hole states : $|s\downarrow\ p^+\uparrow\rangle$, and $|s\uparrow\ p^+\downarrow\rangle$ (respectively A and B if $\Delta_2 > 0$). These are eigenstates of the *c*-axis spin projection operator, so that they change their energy due to the giant Zeeman effect.

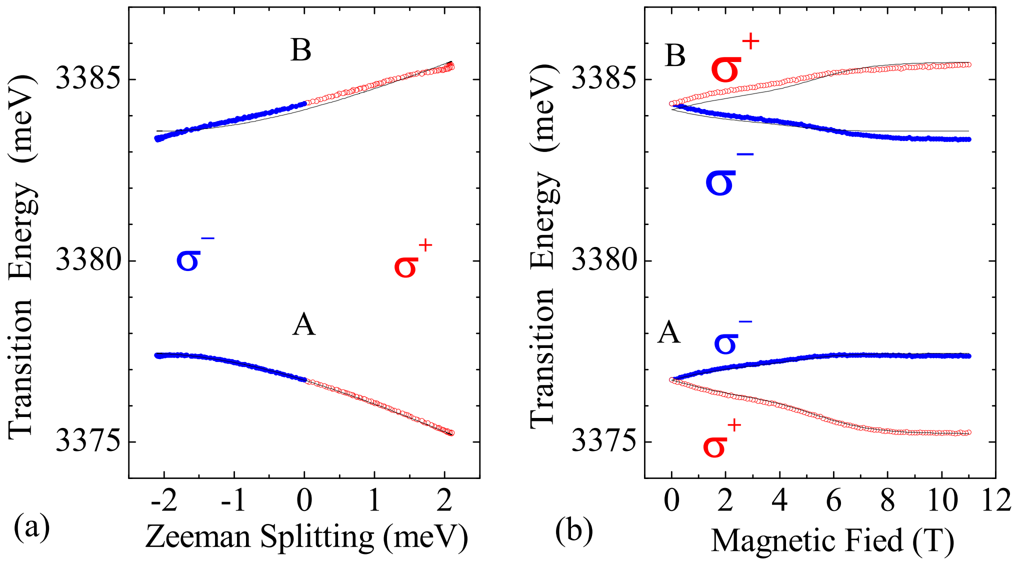

Figure 5.6: Position of the A and B excitons, for the same $Zn_{1-x}Co_xO$ sample as in Fig. 5.3c (with 0.4% Co), measured at different values of the applied field. (a) The horizontal axis is the splitting measured on exciton A, plotted as positive if the σ^+ line is at higher energy. (b) The horizontal axis is magnetic field. Symbols are experimental data : blue (dark gray) for σ^-, red (light gray) for σ^+. Lines are calculated (including for exciton A). Sample ♯Z159.

In that case, one would measure directly the spin-carrier coupling $N_0(\beta - \alpha)$ from the giant Zeeman splitting, as it is show in the plot of Fig. 5.4. In the opposite case, when exchange interaction (γ) dominates over spin-orbit coupling (Δ_2), the two exciton states are formed of the symmetric and antisymmetric combinations of the active electron-hole states : $\frac{1}{\sqrt{2}}(|s \downarrow\ p^+ \Uparrow\rangle + |s \uparrow\ p^+ \Downarrow\rangle)$ (upper exciton, large oscillator strength) and $\frac{1}{\sqrt{2}}(|s \downarrow\ p^+ \Uparrow\rangle - |s \uparrow\ p^+ \Downarrow\rangle)$ (lower exciton, zero oscillator strength). Both excitons have vanishing spin components along the c-axis, so in the first approximation they do not exhibit the giant Zeeman effect in the Faraday configuration. As visible in Fig. 5.3, this is not the case, but any intermediate configuration is possible.

Fig. 5.6(a) shows the position of the A and B excitons, from Fig. 5.3(c), as a function of the splitting of exciton A. It is clear that we observe an anticrossing between the two excitons. It is reasonable to ascribe this anticrossing to the electron-hole interaction. The value of γ describing electron-hole exchange, can be obtained from the minimum distance (2γ) or if we do not observe anticrossing point, from the curvature of excitonic shifts. If we assume that A and B excitons are close to the anticrossing in σ^- circular polarization, the value of γ is equal to a few meV, but rather less than 5.6 meV reported in Ref. 95. However, the two excitons do not show the same curvature, which suggests that we cannot restrict ourself to the interaction between excitons A and B only.

Fig. 5.6(b) shows comparison of the experimental position (symbols) of excitons A and B, as a function of the applied field, to the calculated eigenvalues of the

VB ordering	E_A	$\tilde{\Delta}_1$	Δ_2	Δ_3	γ	$N_0(\beta-\alpha)$
$\Gamma_9, \Gamma_7, \Gamma_7$	3376.7	51	3.0	6.3	3.4	-0.8 eV
$\Gamma_7, \Gamma_9, \Gamma_7$	3376.7	53	-2.1	0.1	3.1	$+0.8$ eV

Table 5.1: Fitting parameters describing giant Zeeman effect observed by reflectivity of $Zn_{1-x}Co_xO$ with $x = 0.4\%$ (sample ♯Z159). Two sets of parameters are used to plot solid line in Fig. 5.6(a,b). Values are given in meV, except for exchange integrals $N_0(\beta-\alpha)$ which is in eV. Value of $N_0\alpha = 0$ was assumed, it was not important for determination of $N_0(\beta-\alpha)$.

Hamiltonian (4.11) [solid lines]. We did not analyze exciton C, except for its zero field energy (3431 meV, see Fig. 5.2), because we do not observe this exciton in the experiments done in our usual Faraday configuration ($B \parallel k \parallel c$). The average spin projection of Co ions is calculated using Eq. (3.8). A good fit is obtained for two sets of values of the parameters given in Table 5.1. The fit is shown in Fig. 5.6(a,b). Fits corresponding to two sets of parameters cannot be distinguished at the scale of the figure.

In both cases, we obtain a very good fit of the lowest exciton, and the fit for the second optically active exciton is reasonable, although not as good. The splittings of both excitons are almost opposite, as experimentally observed. We obtain no information about the valence band ordering (a similar conclusion was claimed by Lambrecht *et al.*[91] in their analysis of the effect of strain). This is due to the fact that we mainly observe an anticrossing between the two excitons A and B, which is a symmetrical process. Hence, our fit is mainly sensitive to the relative value of $(G_h - G_e)$ and γ. We may simply notice that the hypothesis $\Delta_2 > 0$ leads us to a much more isotropic spin-orbit coupling.

5.2.4 Magnetic Circular Dichroism

In samples with Co concentration above 2%, the broadening of the excitonic lines prevents a direct observation of the Zeeman splitting of excitons A and B. In such a case, we measured the degree of circular polarization of the transmitted light, $(I_{\sigma+} - I_{\sigma-})/(I_{\sigma+} + I_{\sigma-})$. For the sake of comparison with published data,[21,24,41–45] we plot the magnetic circular dichroism (MCD) defined as :

$$\mathrm{MCD} = \frac{180°}{4\pi}(k_{\sigma-} - k_{\sigma+}), \tag{5.3}$$

where $k_{\sigma-}$ and $k_{\sigma+}$ are the optical absorption coefficients in σ^- and σ^+ polarizations. Assuming a weak absorption and neglecting multiple reflections, the MCD can be expressed as

$$\mathrm{MCD} = \frac{180°}{2\pi l}\frac{I_{\sigma+} - I_{\sigma-}}{I_{\sigma+} + I_{\sigma-}}, \tag{5.4}$$

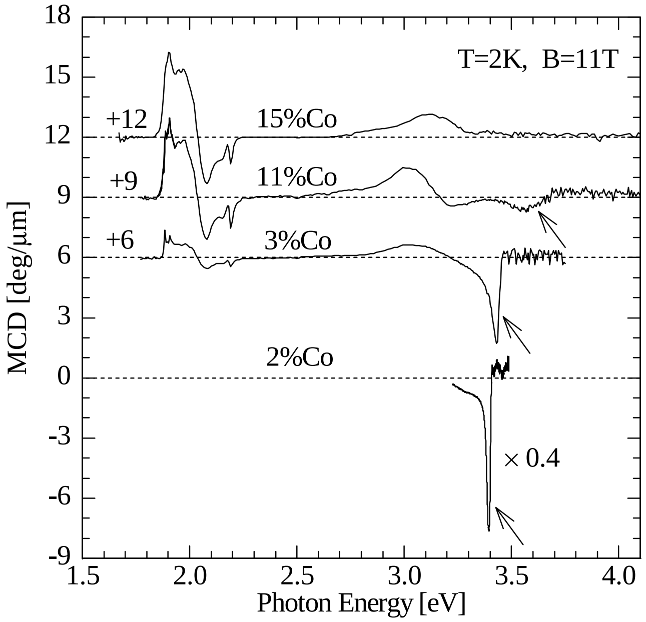

Figure 5.7: (a) Magnetic Circular Dichroism (MCD) obtained in transmission on four $Zn_{1-x}Co_xO$ samples with various Co concentrations. The MCD signal contains three contributions, one (pointed by arrow, most intense in the sample with the lowest Co concentration, $x = 2\%$) close to the band gap at 3.4 eV, the second below the gap, the last one (most intense in the sample with the highest Co concentration, $x = 15\%$) in coincidence with the internal transitions of Co (1.8 eV - 2.3 eV). Spectra are shifted for clarity. Samples : ♯Z159 (0.4%), ♯Z218 (3%), ♯Z215 (11%), ♯Z287 (15%).

where l is the thickness of the sample, and $I_{\sigma+}$ and $I_{\sigma-}$ the intensities of transmitted light in σ^- and σ^+ polarizations. The MCD depends on the photon energy and it is usually very strong near a resonant line or band split by Zeeman effect. In simple cases, the Zeeman splitting ΔE can be estimated[41] from the expression $\mathrm{MCD} = -180°/4\pi \times dk/dE \times \Delta E$, where dk/dE is the derivative of the absorption coefficient in zero field. However, to use properly this equation, the line shape should remain constant : this is not the case in $Zn_{1-x}Co_xO$, where the line shape changes significantly, and where the A and B excitonic transitions are close together. Additionally, they split in opposite directions, as clearly observed on the reflectivity spectra of Fig. 5.3. These changes of the lineshape are the reason, why we did not attempt to determine the absolute value of the Zeeman splitting from these MCD measurements. In each sample, we only analyzed the temperature, spectral and magnetic field dependence of the MCD signal.

We observe three main MCD features over a large spectral range, from 1.7 eV to 4 eV (Fig. 5.7). The first one is related to the energy gap (3.4 eV). In samples up to a Co content of 11%, it is seen as a sharp negative component, which broadens as the Co content increases. It is accompanied by broader positive component from 2.9 to 3.2 eV, which was attributed[21,44,45] to a charge transfer transition, or level to band transition. This peak was used to study the onset of ferromagnetism upon annealing.[45] The third feature corresponds to the internal transitions of cobalt, and

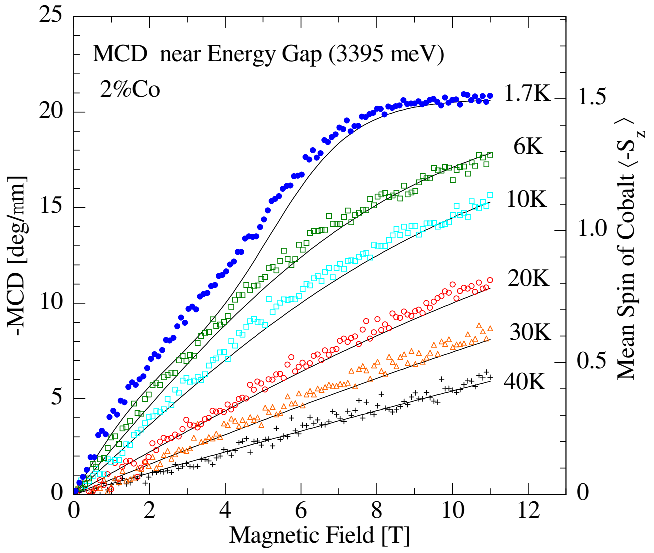

Figure 5.8: Symbols, left vertical axis : Magnetic Circular Dichroism in transmission, at a photon energy 3395 meV, close to the band gap ; lines, right vertical axis : mean spin of isolated Co ions [Eq. (3.8)]. The sample is $Zn_{1-x}Co_xO$ with $x = 2\%$ (♯Z2219).

it is observed between 1.8 eV and 2.3 eV in samples with a Co concentration over 0.4%. Its intensity systematically increases with the Co concentration. This MCD signal is quite complex and mainly results from the different intra-ionic absorption lines. We analyzed them in section 3.2.

We find that the temperature and magnetic field dependence of the MCD signal near the energy gap [Fig. 5.8] is proportional to the magnetic moment of isolated Co ions, even in a sample with a cobalt content of 4.5%. For higher concentrations, the resonant signal becomes too weak and too broad to be detected with reasonable accuracy by our experimental setup.

5.2.5 Discussion

Magnetic properties determined from optical data

A measure of the excitonic Zeeman splitting and of the MCD signal near the energy gap is known to represent an efficient method to study the magnetic properties of DMSs. The dependence on the magnetization results from s, p-d interactions involving substitutional magnetic ions. These magneto-optical properties are less affected by the presence of secondary phases or inclusions, which fully contribute to the magnetization as measured by SQUID. Hence, the observation of a clear effect of the magnetization on the excitonic or band-to-band magneto-optical properties of the semiconductor is a good hint, that the observed magnetization is due to the diluted magnetic semiconductor.

In the whole set of studied $Zn_{1-x}Co_xO$ samples, both the giant Zeeman splitting and the near-bangap MCD signal agree with the idea of a paramagnetic system of isolated Co impurities [Maxwell-Boltzmann occupancy of the $|\pm\frac{3}{2}\rangle$ and $|\pm\frac{1}{2}\rangle$ spin states of Co^{2+}, given by Eq. (3.2)]. This model is based on the observation of characteristic d-d transitions of the $3d^7$ electronic configuration of Co, which confirms the values of the parameters describing the anisotropy and Zeeman effect in the ground state. The intensity of these lines increases linearly with the Co content, which suggests that all Co ions are incorporated in substitution of Zn. A Maxwell-Boltzmann distribution over the spin components in the ground state well accounts for the intensity of the d-d transitions, and for the giant Zeeman effect of the optically active excitons. This demonstrates that $\mathrm{Zn}_{1-x}\mathrm{Co}_x\mathrm{O}$ is a DMS with a coupling between the bands of the semiconductor and the localized spins.

It also results in some differences with respect to the most usual case of Mn-based II-VI DMSs. The magnetization of the single Co ion is not described by the isotropic Brillouin function used for cubic II-VI DMS such as $\mathrm{Cd}_{1-x}\mathrm{Mn}_x\mathrm{Te}$. The anisotropy causes appearance of a step in the field dependence of the magnetization at low temperature, and a deviation from the Curie law in the thermal dependence of the low-field susceptibility. On samples with a few % of Co, we did not need to introduce an effective temperature $T_{eff} = T + T_0$ (see Sec. 3.6.2) in order to describe the influence of spin-spin interactions between neighboring spins (at least, beyond the nearest-neighbor spins). Any such phenomenological Curie-Weiss temperature T_0 has to be smaller than 0.5 K for concentration up to 5%.

On the other hand, in the model we take into account isolated Co ions, so that the eventual magnetic moments associated with Co pairs and complexes are significantly smaller than the moment associated to isolated Co ions. The negligible contribution of anti-ferromagnetically coupled nearest neighbor pairs at low temperature can be explained by short range superexchange interaction integrals higher than a few tens of Kelvin.

In the contrary to the resonant peak close to the energy gap, the MCD signal related to internal Co transitions is not necessarily proportional to the Co magnetization. This signal is governed by the occupancy of the cobalt spin sublevels, the Zeeman shifts, and selection rules of the multiline absorption structure. Experimentally, its temperature dependence is also much weaker than the corresponding one for the energy gap resonant MCD peak.

We have not found any evidence of a ferromagnetic behavior. Upon increasing the Co content, the excitonic Zeeman splitting or the MCD continue to follow the paramagnetic behavior expected for isolated Co impurities - with perhaps the exception of a small additional contribution below 5 T at our lowest temperature curve, which tends to increase with the Co content (compare Figs. 5.5 and 5.8). No hysteretic behavior was detected in agreement with a study of the present samples by magnetometry and electronic paramagnetic resonance.[76] Our result contrast with other observations on samples which have been grown by a different methods, which exhibit ferromagnetic magnetization with an easy axis along the c-axis (an anisotropy which is opposite to the one we see for isolated, substitutional, $3d^7$ cobalt),[19] or with samples which have been annealed.[45] It has been recently suggested that the ferromagnetism may result from the formation of a donor band during the growth or during post-growth annealing treatments.[23,45]

p-*d* exchange integral

The value obtained for the spin-carrier coupling, $N_0|\alpha - \beta| = 0.8$ eV, has to be considered as a first estimate. A larger value of the electron-hole exchange γ reduces the sensitivity of the exciton to the spin splitting, implying a larger spin-carrier coupling. In fact, literature data suggest value of gamma even larger than our estimate, but we could not fit our data with $\gamma = 5.6$ meV. Hypothetical smaller value of γ would lead to the conclusion that $N_0|\alpha - \beta|$ is closer to the value of $N_0|\alpha - \beta|_X = 0.4$ eV determined neglecting electron-hole exchange. Reasonable results are within experimental error about 0.3 eV.

The value $N_0|\alpha - \beta| \simeq 0.8 \pm 0.3$ eV is smaller than in many other DMSs. For example, in $\mathrm{Cd}_{1-x}\mathrm{Co}_x\mathrm{Se}$, another wurtzite Co-based DMS, the exchange integral difference is 2.1 eV.[68,106] However, comparable or even smaller values of $N_0|\alpha - \beta|$ have been also reported for wurtzite DMSs, e.g. -0.26 eV for $\mathrm{Cd}_{1-x}\mathrm{Cr}_x\mathrm{S}$.[102] It is also in significant disagreement with theoretical predictions. Blinowski and co-workers[12] calculated $N_0\beta = -3.2$ eV in for $\mathrm{Zn}_{1-x}\mathrm{Mn}_x\mathrm{O}$. They have also pointed out that the absolute value of $N_0\beta$ is expected to be larger for Co than for Mn ions. Since $N_0\alpha$ is usually about 0.2 eV and does not depend strongly on the host material in II-VI DMSs,[68,122] one could expect $N_0(\alpha - \beta) > 3.4$ eV in the case of $\mathrm{Zn}_{1-x}\mathrm{Co}_x\mathrm{O}$. These predictions are in good agreement with the estimation of $N_0\beta = -3.4$ eV deduced from the analysis of L edge X-ray absorption peaks of Co^{2+} ions in ZnO.[123] A large exchange integral, $N_0\beta = -2.3$ eV, has been also proposed to analyze shift of the absorption edge in $\mathrm{Zn}_{1-x}\mathrm{Co}_x\mathrm{O}$ nanocristallites,[44] but the details of the spectra supporting this conclusion were not given and non-standard model still needs confirmation (in our opinion). The origin of the much smaller value obtained in our case is not understood using a standard description of DMS. We will come back to this surprising result in Chapter 6.

Unfortunately, the sign of $N_0\beta$ cannot be determined experimentally due to the ambiguity of the valence band ordering, so we cannot verify the negative sign of $N_0\beta$ expected from theory. Consequently, $N_0|\alpha - \beta| = 0.8 \pm 0.3$ eV leads to two alternative results. Assuming $N_0\alpha = 0.2 \pm 0.1$ eV, we obtain $N_0\beta = -0.6 \pm 0.4$ eV or $N_0\beta = +1 \pm 0.4$ eV.

5.3 Spectroscopy of $Zn_{1-x}Mn_xO$

5.3.1 Zero field reflectivity

Reflectivity spectra of MBE grown $Zn_{1-x}Mn_xO$ samples are shown in Fig. 5.9(a,b). Spectra are very similar to the reflectivity of MBE grown $Zn_{1-x}Co_xO$ (see Figs 5.1 and 5.2). Fig. 5.9(a) shows, that exciton C can be observed when reflectivity is measured with the incidence angle of 45 degrees, but it disappears from reflectivity spectra measured with the normal incidence, similarly to $Zn_{1-x}Co_xO$. Fig. 5.9(b) shows, that broadening and exciton transition energy increase with magnetic ion concentration x. In contrary to $Zn_{1-x}Co_xO$, A and B excitons in $Zn_{1-x}Mn_xO$ can be resolved even in samples with relatively high magnetic ion concentration. For $x = 1.4\%$, we clearly observe two excitonic features, and by fitting the spectra using a polariton model, A and B can be resolved even in spectrum with the highest accessible concentration of magnetic ions $x = 2.6\%$. Fig. 5.10 shows energy position of A and B excitons determined from spectra shown in Fig. 5.9(b). As in $Zn_{1-x}Co_xO$, exciton transition energy increases with x, however the dependence is weaker, about 8 meV/%.

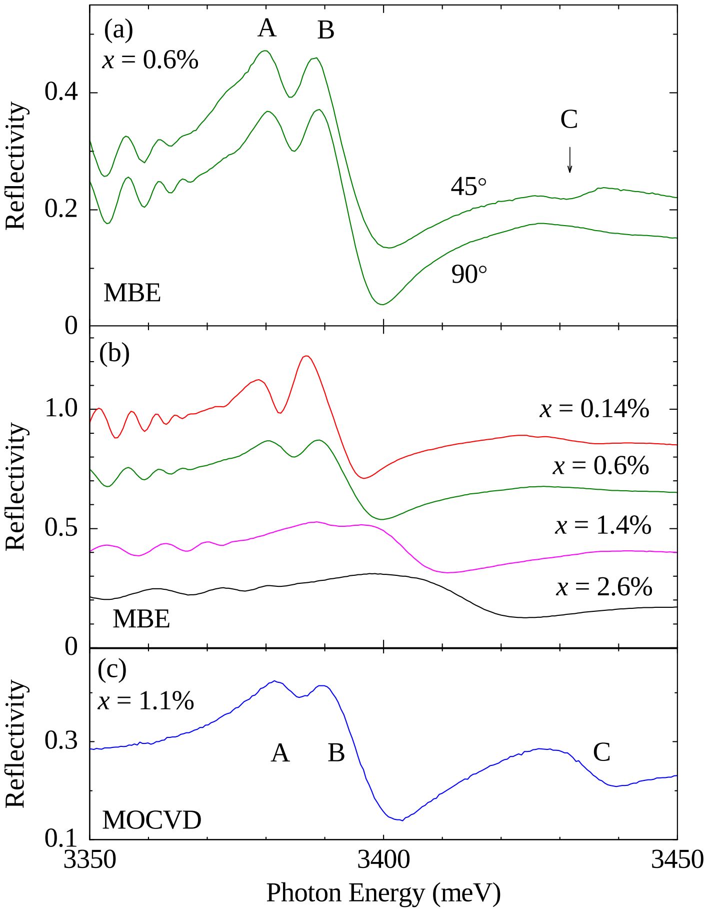

Figure 5.9: (a) Reflectivity spectra of MBE $Zn_{1-x}Mn_xO$ with $x = 0.6\%$ (sample ♯Z435) measured at $T = 1.6$ K with incidence angle of 45 degrees (upper spectrum) and with normal incidence (bottom spectrum, σ polarization). Three excitonic features are labeled A, B, and C. Exciton C disappears at the bottom spectrum because of weak spin-orbit coupling and the optical selection rules. (b) Reflectivity spectra of MBE $Zn_{1-x}Mn_xO$ with increasing Mn concentration, from the top to the bottom : 0.14% (♯Z440), 0.6% (♯Z435), 1.4% (♯Z441), and 2.6% (♯Z434). Spectra are measured with normal incidence. (c) Reflectivity spectra of MOCVD $Zn_{1-x}Mn_xO$ with $x = 1.1\%$ (♯160606-2), measured with normal incidence.

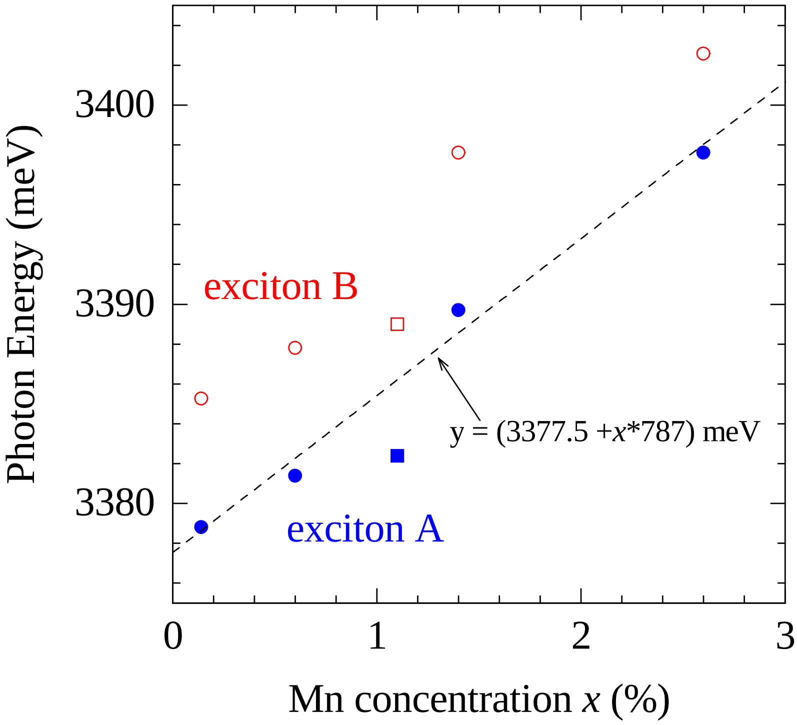

Figure 5.10: Spectral positions of the excitons in MBE $Zn_{1-x}Mn_xO$ (circles), and MOCVD $Zn_{1-x}Mn_xO$ (squares) versus concentration of Mn ions x. Full symbols - exciton A, empty symbols - exciton B. The dashed line shows the linear fit for the position of exciton A in MBE layers. Energies of excitonic transitions were obtained from fit to the reflectivity spectra shown in Fig. 5.9.

Example of reflectivity spectrum of $Zn_{1-x}Mn_xO$ sample grown by MOCVD technique is shown in Fig. 5.9(c). Although the spectrum was measured with normal incident, we observe here exciton C with oscillator strength comparable to strength of excitons A and B. This is very different from the case of MBE layers (a,b), where exciton C is not observed in the reflectivity spectra measured with normal incidence. There are at least two possible explanations : First, c-axis is non-parallel to the growth axis. In such a case, we observed combination of σ and π polarization in reflectivity spectrum. Second, MOCVD layers are under strain which reduce separation energy of excitons, and consequently observation of exciton C in possible also in σ polarization. Surprisingly, none of this explanations can be directly applied in our case : x-ray characterization shows that c-axis is perpendicular to the surface. Separation energy of exciton B and C seems to be even larger for MOCVD sample 5.9(c) comparing to MBE sample 5.9(a). Also zero-field positions of excitons A and B in MOCVD layer (squares in Fig. 5.10) are quite close to positions of A and B excitons in MBE layers with similar concentration of Mn (circles in Fig. 5.10). Therefore, strain cannot be a reason for observation of exciton C. Concluding, we cannot understand zero-field reflectivity of MOCVD layers at this moment. We will come back to this problem later in this section, when we will analyze magnetoreflectivity spectra.

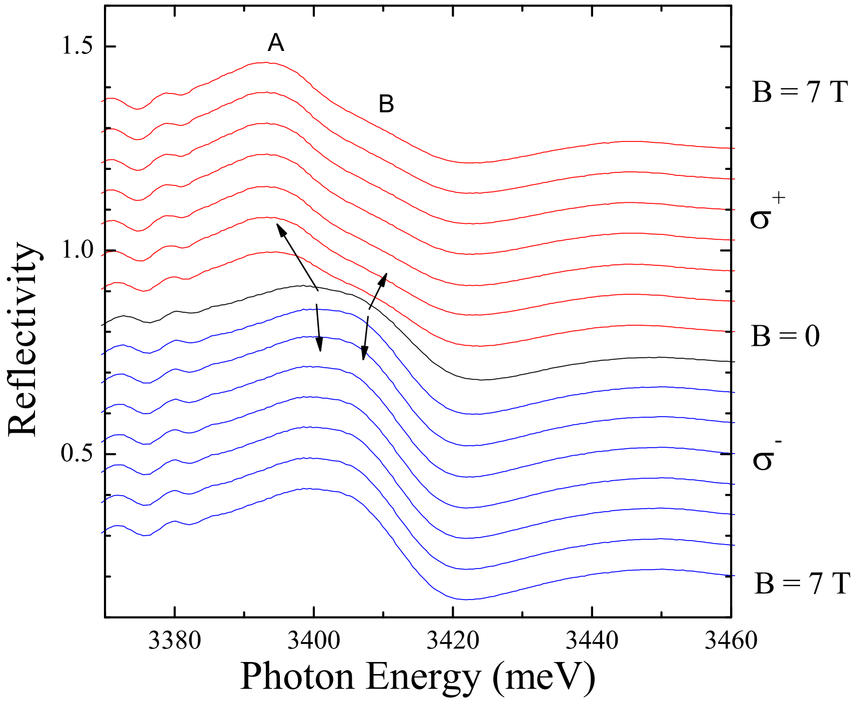

Figure 5.11: Reflectivity spectra of $Zn_{1-x}Mn_xO$ with $x = 2.6\%$ (♯Z434), measured in Faraday configuration at $T = 1.6$ K. Exciton A shifts to low energy in σ^+ circular polarization.

5.3.2 Giant Zeeman effect

Sample with the highest Mn concentration

We have shown in Sec. 5.2.2 and in Fig. 5.3(a,b), that effect of magnetic field on excitons in pure ZnO is very weak, and it is negligible comparing to the giant Zeeman effect in $Zn_{1-x}Co_xO$. It is similarly in $Zn_{1-x}Mn_xO$ (see Fig. 5.11), where s,p-d exchange interactions also induce significant shift of excitons. However magnetic field dependence at super-liquid helium ($T < 2$ K) is different for this two ZnO based DMSs. In $Zn_{1-x}Mn_xO$, about 2 T is almost enough to saturate exchange shift, in $Zn_{1-x}Co_xO$ it was about 8 T. This high magnetic field needed to saturate magnetization of Co^{2+} originates from the anisotropy and significant zero field splitting. Mn^{2+} is almost isotropic and fundamental state is almost degenerate (see Fig. 3.9).

Fig. 5.11 shows that exciton A in $Zn_{1-x}Mn_xO$ shifts to low energy in σ^+ circular polarization, the same as in $Zn_{1-x}Co_xO$. It is the same circular polarization as in $Cd_{1-x}Mn_xTe$, in which also σ^+ circular polarization component of the heavy hole exciton shifts to low energy. This suggest that sign of exchange integrals in $Zn_{1-x}Co_xO$ and $Zn_{1-x}Mn_xO$ is the same. But since we are not sure of the valence band ordering in ZnO, we cannot conclude if the sign of exchange integrals in this two ZnO based DMS is the same as in $Cd_{1-x}Mn_xTe$. We have already discussed this problem in Sec. 5.2.3.

In order to determine the exact energy position of excitons shown in Fig. 5.11, we

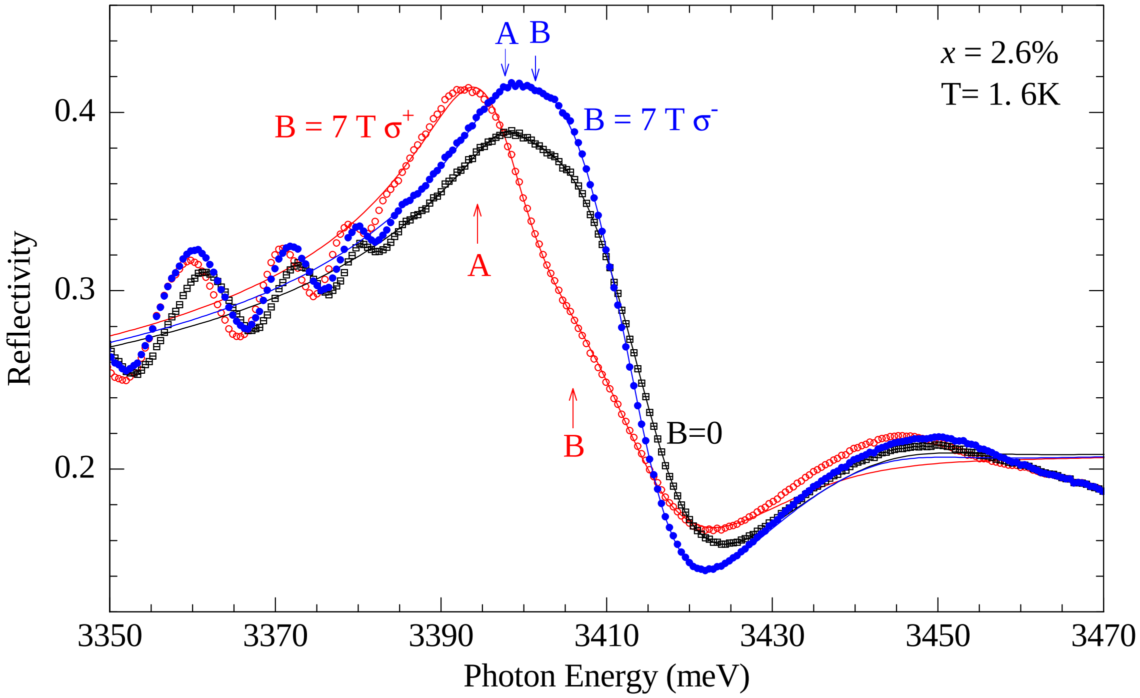

Figure 5.12: Reflectivity spectra (symbols) of $Zn_{1-x}Mn_xO$ with $x = 2.6\%$ (♯Z434), measured at $B = 0$ and $B = 7$ T in two circular polarizations, at $T = 1.6$ K. Solid lines show fits with polariton model. Arrows show determined positions of excitons.

fitted spectra using polariton model described in section 4.7. We took into account excitons A and B (Sec. 4.7.1), and we used a residual dielectric function including excited states and transitions to continuum of states related to A and B (Sec. 4.7.2). As it was shown for diluted $Zn_{1-x}Co_xO$, excited states are not crucial for fitting 1S excitons. However, all excited states can be introduced with only one fitting parameter (Γ_∞). It allows us to fit a larger spectral region. Since we do not observe exciton C, this exciton and related excited states were not included into calculation. Example of spectra and calculated reflectivity are shown in Fig. 5.12. Energies of transitions determined from fits are shown in Fig. 5.13.

Excitonic shifts shown in Fig. 5.13 are much more pronounced in σ^+ circular polarization than in σ^-. It results from electron hole exchange interaction. When $A - B$ separation energy increases (in σ^+), exciton mixing due to electron-hole exchange interaction becomes weaker. In σ^- circular polarization, excitons anticross, so their shifts are strongly reduced. Transition energies can be described by two sets of parameters given in Table 5.2. Two sets of parameters correspond to usual and reversed valence band ordering. Our limited experimental precision does not allow us to discriminate one from both assumptions.

Value of electron-hole exchange energy γ determined form fit is two times smaller than value determined for diluted $Zn_{1-x}Co_xO$ (see Table 5.1). It could be a result of difficult determination of exciton position near the anticrossing of A and B excitons in this $Zn_{1-x}Mn_xO$ sample with relatively high concentration and broad excitonic lines. We will show that diluted $Zn_{1-x}Mn_xO$ can be still described by γ about 3 meV,

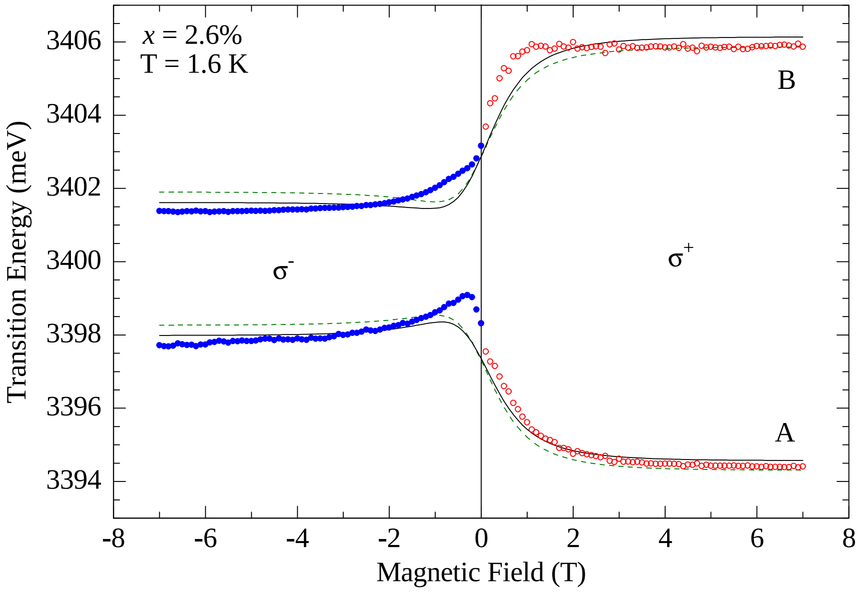

Figure 5.13: Transition energies determined from the reflectivity spectra shown in Figs 5.11 and 5.12 (sample ♯Z434). Lines represent fit with excitonic model. They correspond to sets of fitting parameters given in Table 5.2. Dashed lines correspond to set, where valence band ordering is usual one ($\Gamma_9, \Gamma_7, \Gamma_7$). Solid lines correspond to set, where valence band ordering is reversed ($\Gamma_7, \Gamma_9, \Gamma_7$). In both cases $N_0|\alpha - \beta| \simeq 0.15$ eV. Sample has Mn concentration determined by SIMS $x = 2.6\%$, so we estimate $x_{eff} = 1.9\%$ (see Eq. 3.13).

VB ordering	E_A	$\tilde{\Delta}_1$	Δ_2	Δ_3	γ	$N_0(\beta - \alpha)$	$N_0(\beta + \alpha)$
$\Gamma_9, \Gamma_7, \Gamma_7$	3397.3	43.0	+2.3	0.0	1.5	−0.14 eV	−0.14 eV
$\Gamma_7, \Gamma_9, \Gamma_7$	3397.4	38.1	−0.5	8.9	1.6	+0.15 eV	+0.15 eV

Table 5.2: Fitting parameters describing giant Zeeman effect determined using reflectivity of $Zn_{1-x}Mn_xO$ with $x = 2.6\%$ (sample ♯Z434). Two sets of parameters are used to plot solid lines in Fig. 5.2. Values are given in meV, except for exchange integrals $N_0(\beta - \alpha)$ and $N_0(\beta + \alpha)$, which are in eV. Since we do not observe exciton C, estimation of $N_0(\beta + \alpha)$ has huge experimental error, much larger than obtained value.

same as obtained for $Zn_{1-x}Co_xO$.

For one set of parameters in Tab. 5.2, fitting procedure leads to $\Delta_3 = 0$. It is an artefact, because $\Delta_3 \neq 0$ leads to decrease of the shift of exciton involving Γ_7 hole, X_{Γ_7}. Therefore fitting procedure results in $\Delta_3 = 0$ for valence band ordering where shift of X_{Γ_7} is larger than shift of X_{Γ_9}. In our case (but also in case of fit to $Zn_{1-x}Co_xO$ data) asymmetry between A and B is within experimental error, so serious determination of Δ_3 is not possible. Since we do not observe exciton C, also determination of $N_0(\beta + \alpha)$ is rather risky in this experiment.

In both sets of parameters of Table 5.2 $N_0|\beta - \alpha|$ are almost equal. It is a result of the fact that this parameter is determined from shifts of excitons in σ^+ circular

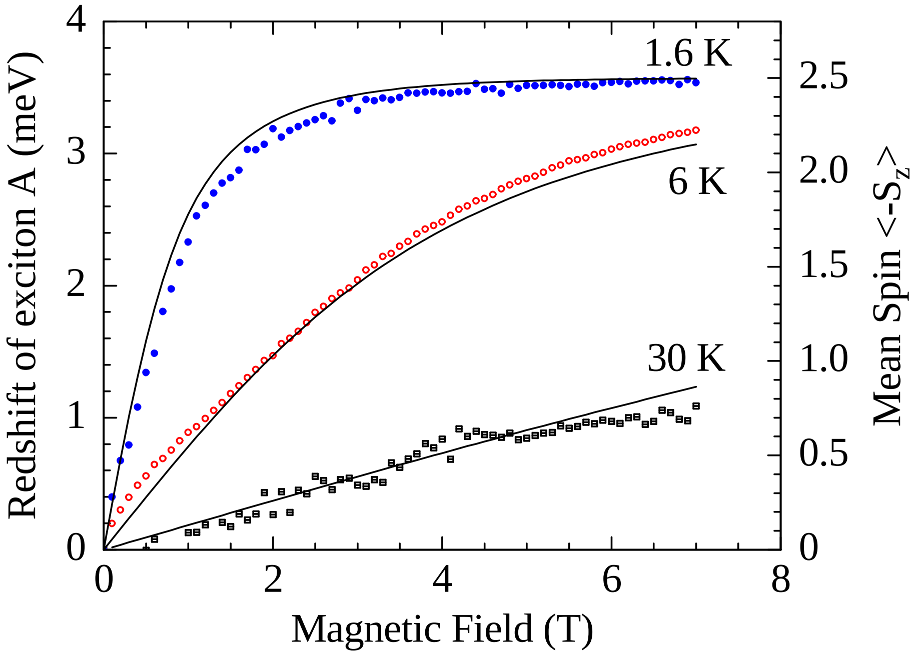

Figure 5.14: Redshift of exciton A in $Zn_{1-x}Mn_xO$ with the highest accessible Mn concentration, $x = 2.6\%$ (sample ♯Z434). It is determined for 3 temperatures (left axis), as a function of magnetic field. The redshift is compared to the mean spin of Mn^{2+} (right axis), given by Brillouin function (3.4) with the same temperature as set in experiment (there is no effective temperature).

polarization, and it very weakly depends on other parameters (important for σ^-). As it was in $Zn_{1-x}Co_xO$, sign of determined $N_0(\beta-\alpha)$ depends on assumed valence band ordering. Assuming usual valence band ordering $(\Gamma_9, \Gamma_7, \Gamma_7)$ we find negative $N_0(\beta-\alpha)$, and assuming valence band ordering $(\Gamma_7, \Gamma_9, \Gamma_7)$ we find $N_0(\beta-\alpha) > 0$.

From two shifts observed in σ^+ circular polarization : redshift of exciton A and blue shift of exciton B, easier to be determined is redshift of A. It is clearly visible in the spectra even without polariton fit. Moreover, it is sure that exciton A do not anticross with others excitons, when it shifts to low energy, so effect of electron-hole exchange interaction on this shift should be suppressed. Fig. 5.14 shows that the redshift of exciton A is proportional to the magnetization calculated using Brillouin function. It confirms that the redshift of A is mainly governed by *s*,*p*-*d* exchange interactions.

Concluding, analysis of MBE grown $Zn_{1-x}Mn_xO$ samples with high Mn content is very useful for determination of exchange integral difference, but it cannot rather serve to determine properties of ZnO, such as valence band ordering.

Sample with optically active C exciton

Magnetoreflectivity of MOCVD $Zn_{1-x}Mn_xO$ layer with $x = 1.1\%$ is shown in Fig. 5.15. There are three excitons in the spectra. We clearly observe splitting of A and B excitons, but energy position of exciton C remains constant up to $B = 7$ T.

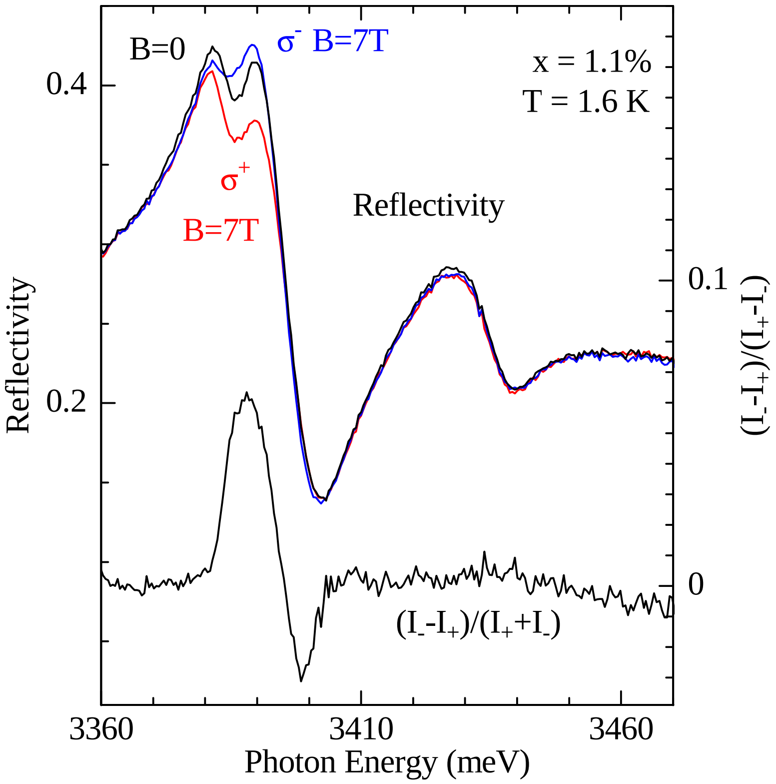

Figure 5.15: Left axis : Reflectivity of MOCVD $Zn_{1-x}Mn_xO$ with $x = 1.1\%$ (sample ♯160606-2), in Faraday configuration. Right axis : MCD of reflectivity defined as : $\frac{I_- - I_+}{I_- + I_+}$. There is a strong dichroism related to excitons A and B, but we do not observe dichroism related to exciton C.

We were very motivated to find exciton C which splits in circular polarizations. It could help us to determine valence band ordering in ZnO. In order to find any trace of magnetic field effects related to exciton C, we plotted reflectivity-MCD signal ($\frac{I_- - I_+}{I_- + I_+}$) shown below reflectivity spectra in Fig. 5.15. There is a significant dichroism related to A and B excitons, but dichroism related to exciton C is below level of noise. If the observed feature is really related to exciton C in σ polarization, then $N_0(\beta + \alpha)$, which govern splitting of exciton C, is close to zero. On the other hand, we could observe exciton C in π polarization. Such exciton cannot be easily split by magnetic field due to electron-hole exchange interaction. This explanation seems to be more probable if we take into account that surface of this sample is not optically flat. Reflected light is strongly dispersed, so there are various facets, and some of them allows interaction of the light and exciton C. Anyhow, using exciton C in this sample, we cannot get information about valence band ordering in ZnO. Shifts of excitons A and B determined for this sample leads to significantly smaller value of $N_0|\beta - \alpha|$ than in the case of other samples. It is about 0.05 eV. This result can be affected by problems with polarization.

Diluted samples

Since the difference of exchange integrals is evidently smaller in $Zn_{1-x}Mn_xO$ comparing to $Zn_{1-x}Co_xO$, we didn't expect huge magnetooptical effects in more diluted $Zn_{1-x}Mn_xO$. Nevertheless, this kind of samples appeared to be very interesting for our work. It is related to very high optical quality, which allow us to test the model of reflectivity spectra and to resolve 2S excitons. Fig. 5.16 presents reflectivity of samples with $x = 0.14\%$ and 0.6%.

Procedure of fitting of the reflectivity spectra was slightly different than in case of highly doped sample. This time we would like to include impact of electron hole-exchange interaction on reflectivity spectra. Position of 2S excitons were assumed to be independent on position of 1S excitons. The excitonic effects such as electron-hole exchange interaction or diamagnetic shift, are different for 1S and 2S excitons. Therefore, we had to take into account four fitting parameters related to energy : E_{A1S}, E_{B1S}, E_{A2S}, and E_{B2S}. In the first (but successful) try, exciton C was neglected, and we had no reason to introduce it into the model. Next, we had three parameters related to oscillator strength : $4\pi\alpha_{0A}$, $4\pi\alpha_{0B}$, and parameter describing relation of oscillator strength of 2S excitons A and B. We did not assume that oscillator strength of each 2S exciton is equal to 1/8 of oscillator strength of corresponding 1S exciton. Such an assumption would be unjustified. The oscillator strengths of 1S excitons A and B are exchanged due to electron-hole exchange interaction. Instead of this, the sum of the oscillator strength of 2S excitons should conserve following rule : $(4\pi\alpha_{0A2S} + 4\pi\alpha_{0B2S}) = (4\pi\alpha_{0A} + 4\pi\alpha_{0B})/8$. Finally, we had three parameters describing damping : Γ_A, Γ_B, and Γ_∞. In zero field we fitted background dielectric constant, and we found $\epsilon = 3.6$, then we kept this value constant and we left 10 above parameters, as free parameters for fitting various spectra in the magnetic field. Since intensity of 1S excitonic features is much larger comparing to 2S, fit is very good for 1S excitons, and but we are not able to fit all details of spectra near 2S excitons. It would be probably possible if we do separate fits for region of 1S and 2S excitons.

VB ordering	E_A	$\tilde{\Delta}_1$	Δ_2	Δ_3	γ	$N_0(\beta-\alpha)$
$\Gamma_7, \Gamma_9, \Gamma_7$	3381.4	51.1	0.5	11.6	2.7	+0.22 eV

Table 5.3: Fitting parameters describing giant Zeeman effect observed using the reflectivity of $Zn_{1-x}Mn_xO$ with $x = 0.6\%$[according to Eq. (3.13), $x_{eff} = 0.56\%$]. Values are given in meV, except for $N_0(\beta-\alpha)$ which is in eV. Value of $N_0\alpha = 0.2$ eV is assumed. Splitting of exciton B larger than splitting of exciton A suggests reversed valence band ordering, but we cannot be sure that this difference is significantly larger than experimental error. Sample ♯Z435.

Transition energies, polarizabilities, and damping parameters of 1S excitons determined for sample with $x = 0.6\%$ are plotted in Fig. 5.17. As expected (see Sec. 4.5.3), we observe the decrease of the polarizability (and oscillator strength) of exciton A, and the increase of the polarizability of exciton B near the anticrossing. However, a quantitative interpretation of this result is difficult because the changes of the polarizability are associated by the significant changes of the value of damping parameter Γ. When exciton lines overlap, it is very difficult to distinguish between the increase of polarizability and the decrease of damping. Both result in sharper

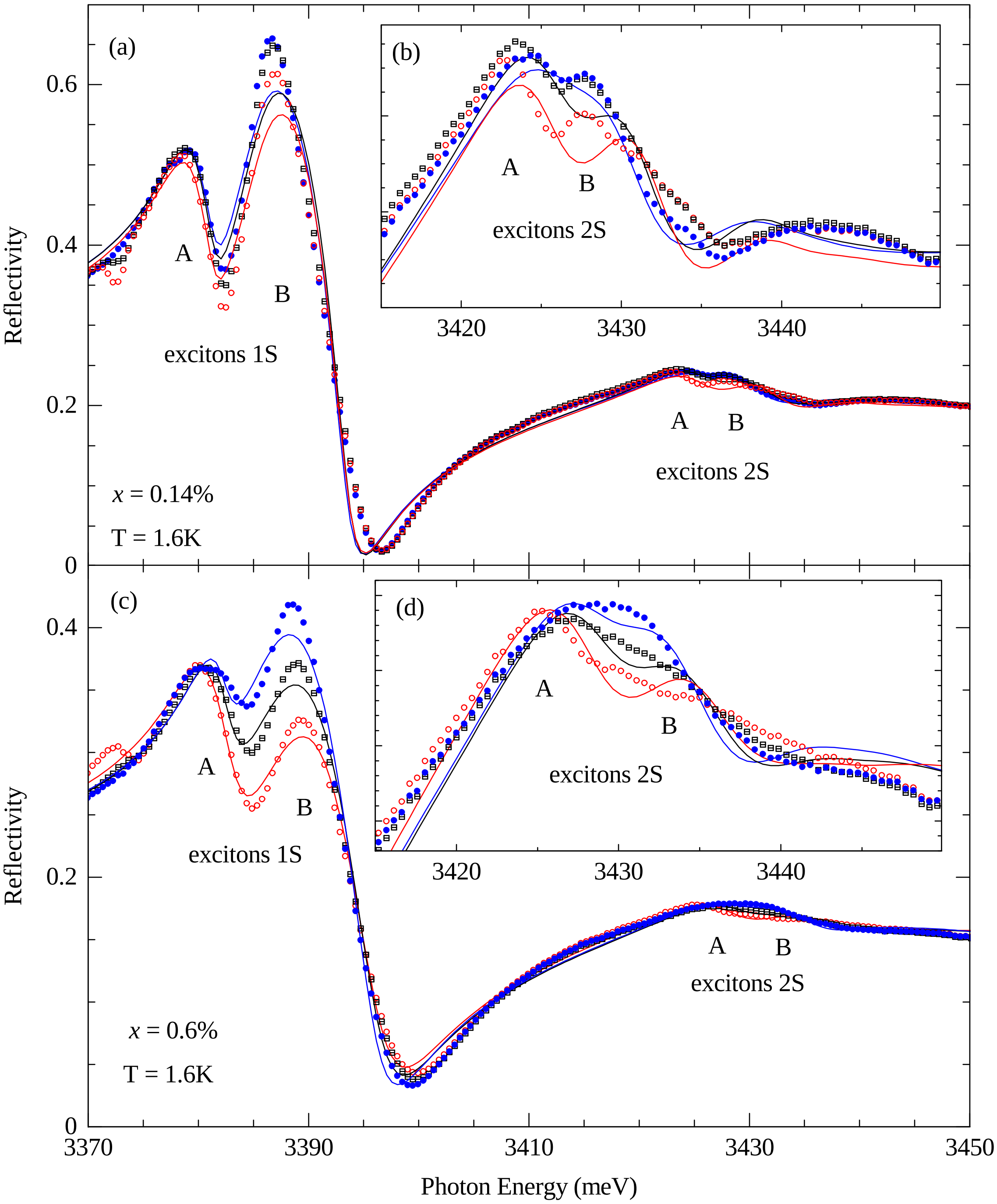

Figure 5.16: Reflectivity spectra (points) of $Zn_{1-x}Mn_xO$ with $x = 0.14\%$ (a,b) and $x = 0.6\%$ (c,d). Solid lines show fits with polariton model. Features related to 1S and 2S excitons A and B are marked. Spectral region with 2S excitons is plotted with different scale in inserts (b) and (d). Blue color of symbols and lines is related to σ^- circular polarization and magnetic field $B = 7\ T$, black color of symbols and lines is related to spectra measured at $B = 0$, red color of symbols and lines is related to σ^+ circular polarization and magnetic field $B = 7\ T$. Sample with $x = 0.14\%$ is labeled ♯Z440, sample with $x = 0.6\%$ is labeled ♯Z435.

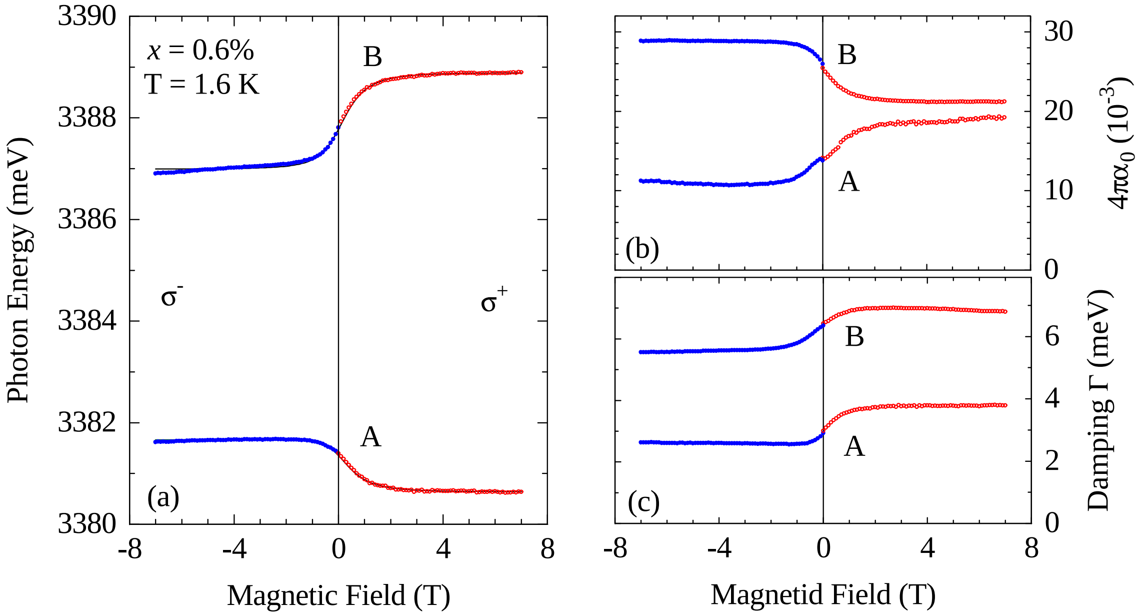

Figure 5.17: Transition energies (a), polarizabilities (b), and damping parameters (c) determined from the reflectivity spectra shown in Fig 5.16(c). Lines in (a) represent fit with excitonic model and with parameters given in Table 5.3. Sample (♯Z435) has Mn concentration determined by SIMS $x = 0.6\%$.

excitonic line.

In order to determine parameters given in Table 5.3, we fitted transition energies of Fig. 5.17(a) using our standard hamiltonian (4.11) describing excitonic giant Zeeman effect. It is interesting that although spin-orbit parameter Δ_2 has been found to be positive, valence band ordering have been found to be reversed due to interaction with exciton C. Our experimental precision is not high enough to be sure of this result, but we should consider it, at least.

5.3.3 Photoluminescence study of bound excitons

Pure ZnO and GaN exhibit strong photoluminescence signal near energy gap, but introducing magnetic ions leads to significant quenching of the photoluminescence intensity. The effect of quenching seems to be the less efficient in $Zn_{1-x}Mn_xO$, when it is compared to other studied wide gap DMSs.

Fig. 5.18(a) presents photoluminescence spectra in logarithmic scale. It is magneto-photoluminescence of MOCVD grown $Zn_{1-x}Mn_xO$ with $x = 2.5\%$. The zero-field PL is quite weak, but PL measured at $B = 7$ T is one order of magnitude stronger. Comparing to zero field, PL lines at $B = 7$ T are shifted to low energy by 5 meV (σ^+) and 6 meV (σ^-). Energy position of the PL peak is shown in Fig. 5.18(b). Energy shift approximately follows a Brillouin function.

It is interesting to note, that shifts observed in spectra PL are different from shifts observed in reflectivity (presented in previous paragraphs). The difference is visible for σ^- circular polarization. In magneto-reflectivity measurements, exciton

A in σ^- shifts first to high energy, than anticrosses with exciton B. In magneto-PL measurements, exciton A shifts directly to low energy. In σ^+ circular polarization, there is no important difference between PL and reflectivity results. In both measurements, we observe redshift of exciton A.

PL redshift shift is larger in σ^- than in σ^+. Therefore splitting observed in photoluminescence has opposite sign when it is compared to the splitting of exciton A in reflectivity. PL line observed in σ^+ is stronger than PL line observed in σ^- .

Shift of both : photoluminescence line and exciton A observed in reflectivity, are related to A valence band, but reflectivity mainly probes free excitons, because they have large oscillator strength, and PL mainly probes bound excitons, because of their lower energy comparing to free excitons. Nevertheless, the origin of difference between giant Zeeman splitting of bound and free excitons is not understood for us at this moment. We will come back to this problem in Chapter 6.

We can eventually interpret PL-redshift of strong component (in σ^+). It is similar to the redshift observed in reflectivity measurements in the same polarization. A value of both shifts at saturation is quite close for samples with similar concentration of Mn. The redshift of A is 3.5 meV for $x = 2.6\%$ in reflectivity and 5 meV for $x = 2.5\%$ in PL. This suggest that both results are related to the energy of the giant Zeeman shift $1/2xN_0(\alpha - \beta)$.

Nonlinear increase of the PL amplitude with magnetic field is shown in Fig. 5.18(c). Similar changes, has been already reported for $Zn_{1-x}Mn_xSe$ in Ref. 124. The reduced effect of quenching under magnetic field was explained by spin polarization of carriers and Mn^{2+}, which blocks relaxation channel involving Mn. In consequence, near energy gap PL intensity strongly increases with magnetic field. This explanation seems to be reasonable also for the case of magneto-PL of $Zn_{1-x}Mn_xO$.

5.3.4 Magnetic Circular Dichroism

Transmission MCD (Fig. 5.19) was measured for the sample, which was previously studied using PL (Fig. 5.18). As expected shape and sign of MCD signal (Fig. 5.19a) is the same as in $Zn_{1-x}Co_xO$ (Fig. 5.7). However, the temperature dependence of the amplitude of MCD signal in $Zn_{1-x}Mn_xO$ (Fig. 5.19b) is very different from analogical dependence observed for $Zn_{1-x}Co_xO$ (Fig. 5.8). It is due to the magnetization of Mn^{2+} governed by Brillouin function, while the magnetization of Co^{2+} is governed by function including zero-field splitting of the fundamental state.

Weak deviations from Brillouin function can be observed in MCD dependence of this highly doped $Zn_{1-x}Mn_xO$ sample (Fig. 5.19b). These deviations were not yet confirmed by other experiments. They can be related to some magnetization steps, or to complex excitonic behavior. The redshift of exciton A measured for the sample with similar concentration of Mn, as shown in Fig. 5.14, does not show similar deviations from Brillouin function.

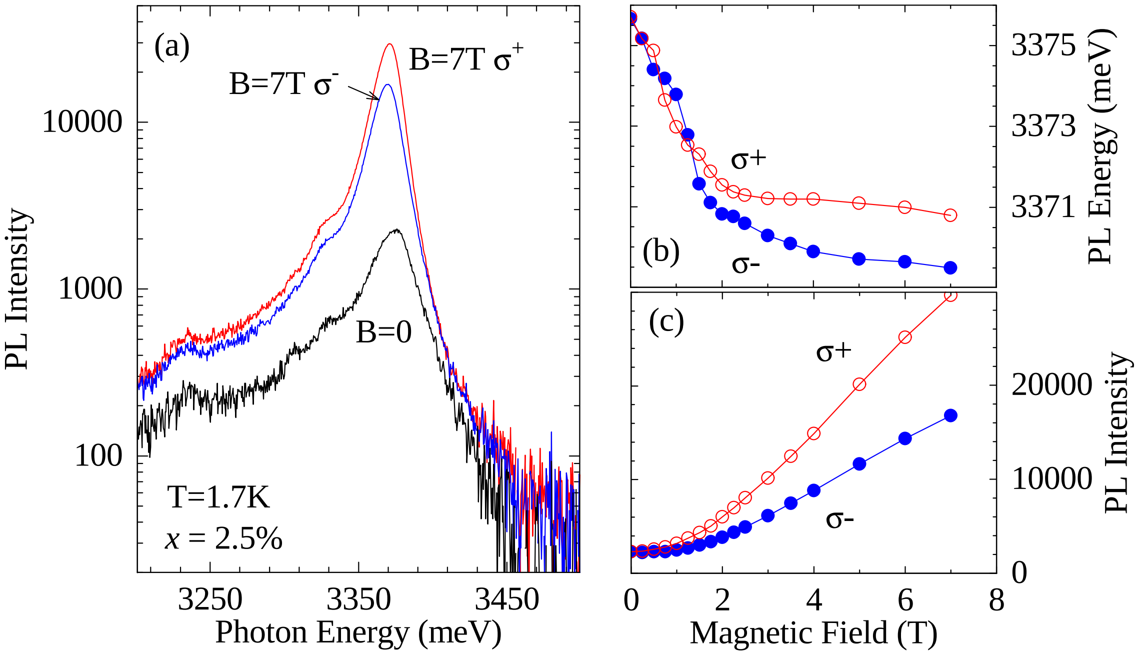

Figure 5.18: (a) Photoluminescence spectra of $Zn_{1-x}Mn_xO$ with 2.5% Mn (sample ♯1207) shown in the logarithmic scale. (b) Spectral position of the PL peak shown in (a) vs magnetic field. (c) Amplitude of photoluminescence peak vs magnetic field.

5.3.5 Discussion

In our experiments, $Zn_{1-x}Mn_xO$ appears to be almost typical II-VI DMS : magnetization is well described by Brillouin function, circular polarization of the giant Zeeman effect is the same as in $Cd_{1-x}Mn_xTe$ (if we assume usual valence band ordering), introduction of Mn does not degrade optical quality of the crystal too much. We can observe excitons using reflectivity and photoluminescence in samples with quite high concentration of magnetic ions. There is one important difference : strength of *s*,*p*-*d* exchange interactions is without any doubts one order of magnitude weaker than expected from Schrieffer-Wolf theory : $N_0\beta = -3.2$ eV if material parameters are derived theoretically,[12] or $N_0\beta = -3.0$ eV if material parameters were determined from x-ray spectroscopy.[123]

In order to obtain the final magnetooptical estimation of the strength of *s*,*p*-*d* exchange interactions, we summarized all accessible results in Fig. 5.20. There are redshifts of exciton A (related to Γ_9 valence band if usual valence band ordering is observed) and blueshifts of exciton B (related to Γ_9 valence band if reversed valence band ordering is observed). There is also shift of PL line to low energy determined for our highly doped sample, and three PL redshifts reported in Ref. 39. Mn concentration in this reference has been calibrated by SQUID not by SIMS, as it is in case of our samples, so we have two quite independent estimations. In the simplest model neglecting excitonic interactions in σ^+, A and B exciton shift due to *s*,*p*-*d* exchange is governed by $\frac{1}{2}x_{eff}\langle\text{-}S_z\rangle N_0|\beta-\alpha|$. We show this dependence for $x_{eff} = x(1-x)^{12}$ and for three different values of $N_0|\beta-\alpha|$: 0.10, 0.15, and 0.20 eV. The solid line

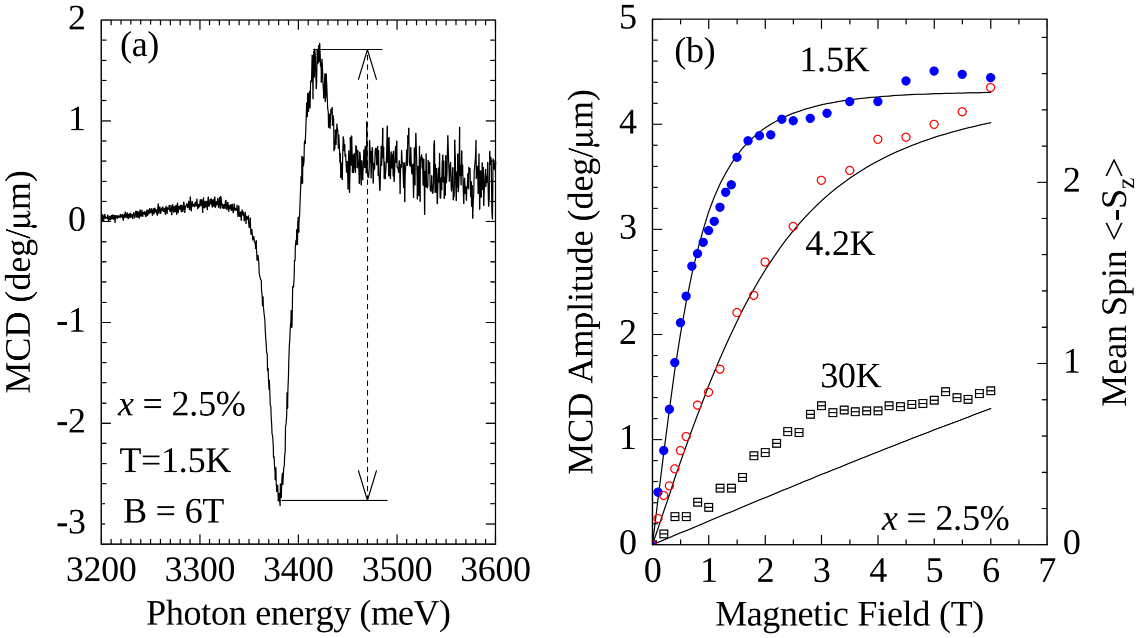

Figure 5.19: (a) Spectrum of magnetic circular dichroism (MCD) measured for $Zn_{1-x}Mn_xO$ with 2.5% Mn (sample ♯1207), at $T = 1.5$ K, and $B = 6$ T. (b) Symbols, left axis : MCD amplitude shown by the arrow in (a), is plot versus magnetic field, for three temperatures. Solid lines, right axis : mean spin of Mn^{2+}, given by Brillouin function (3.4) with the same temperature as set in experiment.

calculated for $N_0|\beta - \alpha| = 0.15$ eV well describes majority of presented results and we will keep it as final value. This value can be slightly underestimated, because effect of electron-hole exchange interaction has been not taken into account, but the fits of excitons A and B shown in Table 5.2 give almost the same values of $N_0|\beta - \alpha|$. It means that the effect of electron-hole exchange interaction on the redshift of exciton A is much less important than the effect of electron-hole exchange interaction on giant Zeeman splitting (analyzed for $Zn_{1-x}Co_xO$). Very prudent estimation of the experimental error requires taking 0.1 eV as an experimental error, but extreme points are not so well understood (PL and samples with strange reflectivity spectra), as points near solid line (carefully fitted reflectivity data). Thus a smaller error 0.05 eV seems for us to be justified.

Assuming usual value of $N_0\alpha = +0.2 \pm 0.1$ eV, from our value of $N_0|\beta - \alpha| = 0.15 \pm 0.05$ eV, we obtain in both cases positive *p-d* exchange interaction $N_0\beta = +0.35 \pm 0.15$ eV or $N_0\beta = +0.05 \pm 0.15$ eV. We note, that second result includes within the experimental error zero and negative values. We can estimate the limit of absolute value of *p-d* exchange integral $|N_0\beta| < 0.5$ eV. In any case our experiment excludes $N_0\beta = -3.0$ eV within experimental error.

It is interesting, that *s,p-d* exchange interactions in $Zn_{1-x}Mn_xO$ are significantly weaker comparing to $Zn_{1-x}Co_xO$. This conclusion could be already deduced from MCD spectra measured by Ando *et al.*[41] for various ZnO based DMS. MCD signal was there much more weak for $Zn_{1-x}Mn_xO$ than for $Zn_{1-x}Co_xO$. We will continue

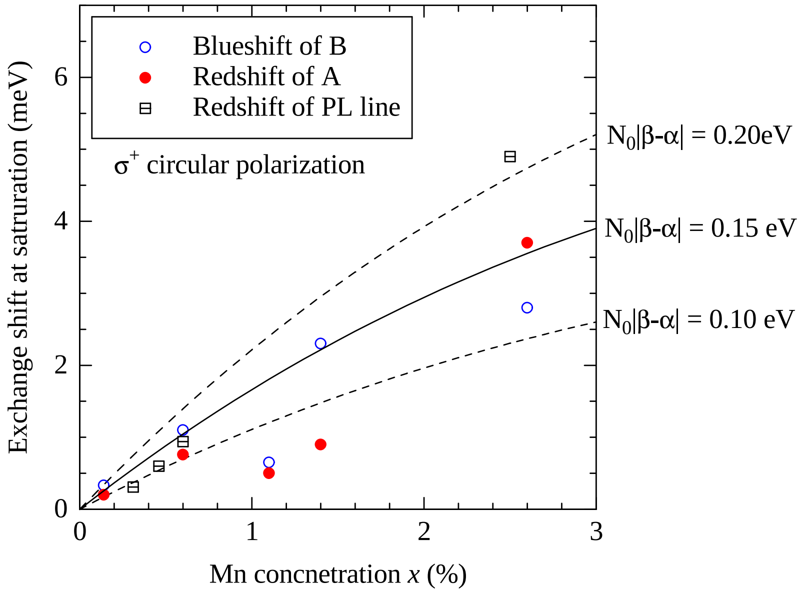

Figure 5.20: Summary of the experimental results on $Zn_{1-x}Mn_xO$. Shift of excitons induced by *s*,*p*-*d* exchange interactions, observed in σ^+ circular polarization. The shifts are measured at saturation and plotted versus Mn concentration. There is the redshift of exciton A determined using reflectivity (full circles, red color) ; the blueshift of exciton B in σ^- circular polarization determined using reflectivity (empty circles, blue color) ; the redshift of bound exciton A determined from photoluminescence measurements (squares, black color). PL data for three diluted samples are taken from Ref. 39. Solid line represents value of the shift $\Delta E = -1/2 N_0(\alpha - \beta) x_{\mathrm{eff}} \langle\text{-}S_z\rangle$ calculated with $N_0|\alpha - \beta| = 0.15$ eV, $\langle\text{-}S_z\rangle = 2$, $x_{\mathrm{eff}} = x(1-x)^{12}$. Dashed lines correspond to values $N_0|\alpha - \beta| = 0.25$ eV and $N_0|\alpha - \beta| = 0.05$ eV.

discussion of exchange integrals in Chapter 6.

5.4 Spectroscopy of $\mathrm{Ga}_{1-x}\mathrm{Mn}_x\mathrm{N}$

5.4.1 Zero field reflectivity

We measured reflectivity spectra in our usual configuration ($k \parallel c$), where only the σ polarization is accessible. In zero-field spectra, we observe two characteristic features. For the most diluted sample [$x = 0.01\%$, Fig. 5.21(a)], the energy of these features corresponds to the energy of the A and B excitons in GaN, shifted toward high energy by a biaxial compressive strain estimated to be about 19 kbar according to Ref. 104. Such a strain strongly reduces the oscillator strength of exciton C. In addition, exciton C is particularly sensitive to the broadening due to strain disorder. This explains why we do not observe a third structure at about 3540 meV, as expected for exciton C for such a strain value. In another sample with $x = 0.5\%$ [see the middle spectra marked as $B = 0$ in Fig. 5.21(b)], A and B excitonic features are further broadened and shifted to higher energies. This shift confirms the increase of the band gap energy upon increasing the Mn content, previously inferred from MCD spectra.[47]

5.4.2 Giant Zeeman effect in reflectivity and absorption

Magneto-optical spectra were measured in the Faraday configuration, with the magnetic field parallel to the common c-axis and optical axis. Magneto-reflectivity spectra of pure GaN or very diluted $\mathrm{Ga}_{1-x}\mathrm{Mn}_x\mathrm{N}$ ($x = 0.01\%$, not shown), exhibit a very small excitonic Zeeman shift, $\Delta E < 0.5$ meV, even at $B = 11$ T, in agreement with previously reported data on GaN.[93,125] We will describe the details of the magnetoreflectivity of GaN in Sec. 5.5.

The Zeeman shift of excitons is strongly enhanced in the presence of a significant content of Mn ions. This is shown in Fig. 5.21(b), which displays reflectivity spectra of the sample with $x = 0.5\%$, at 1.7 K and different values of the applied field. Exciton A shifts to low energy (redshift) in σ^- polarization ($\Delta E = 6$ meV at $B = 11$ T). Note that the saturation of the redshift of A starts at quite high field values when compared to other DMS containing Mn^{2+} (d^5 configuration). In σ^+, exciton A shifts to high energy and merges with the B exciton. The behavior of exciton B is more complex. Excitons A and B are observed also in absorption, Fig. 5.21(c), however, excitonic features are more visible in the derivative of these absorption spectra, Fig. 5.21(d), which confirm the observations made on the reflectivity spectra.

The positions of excitonic features were determined by different methods. The most advanced method involves a detailed fit of the reflectivity spectra using a model based on the dielectric function related to the three excitons A, B, and C, including their optically active excited states, and transitions to the continuum of states, as described in Sec. 4.7.2. Since we observe very broad excitonic structures (compare with reflectivity of GaN, Fig. 5.27 or ZnO, Fig. 5.1), we neglected here polaritonic effects, which are important only for sharp excitonic lines.[113] The dielectric function was calculated for the system formed by a 374 nm thick $\mathrm{Ga}_{1-x}\mathrm{Mn}_x\mathrm{N}$ layer (thickness determined from SIMS) deposited on a semi-infinite substrate with an refractive in-

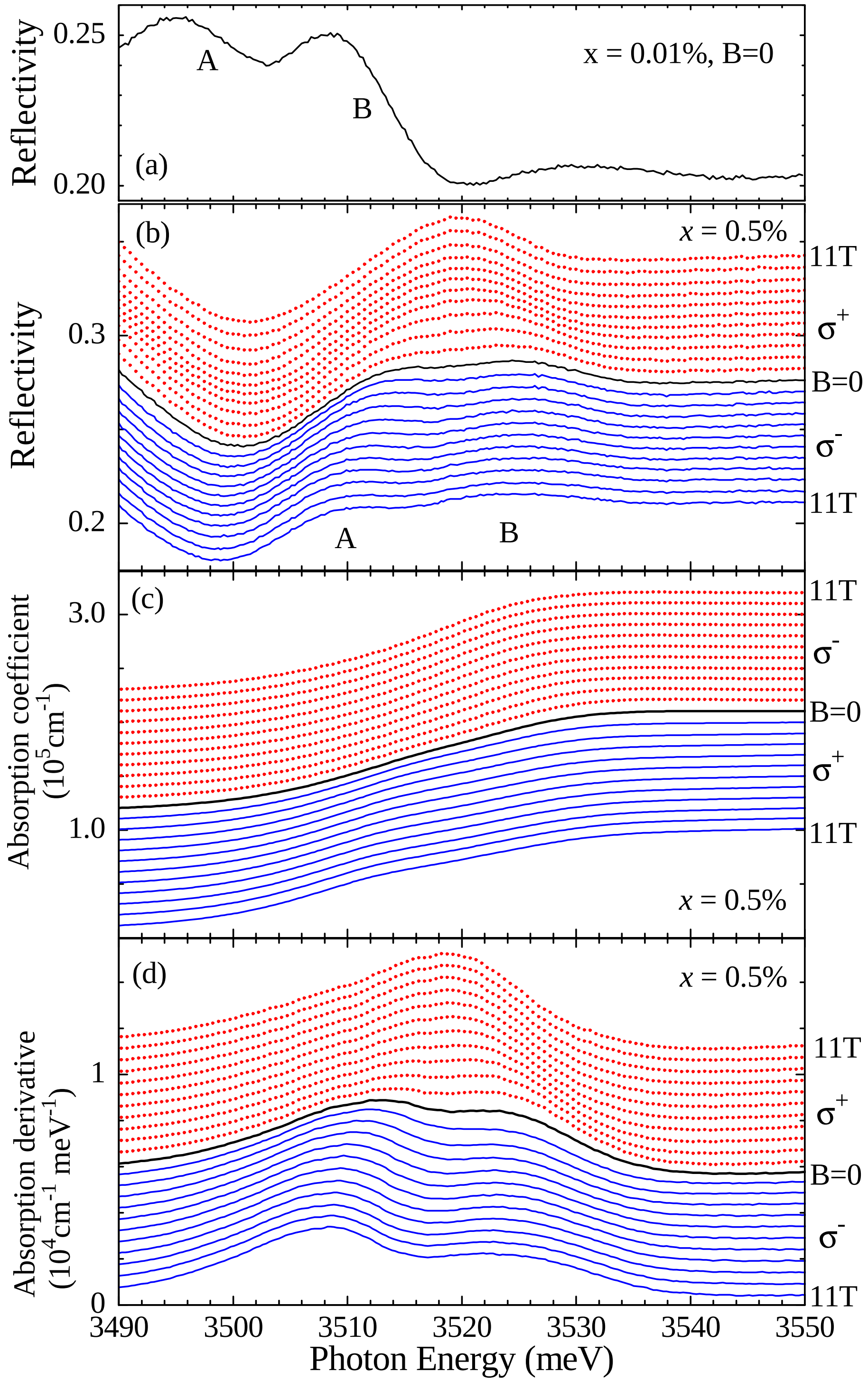

Figure 5.21: a) Reflectivity measured for $Ga_{1\text{-}x}Mn_xN$ with $x = 0.01\%$ (sample ♯E787). (b) Reflectivity, (c) absorption and (d) derivative of absorption, for $x = 0.5\%$ (sample ♯E766), in Faraday configuration, in σ^+ (red color, dots) and σ^- (blue color, solid lines) circular polarization, at $T = 1.7$ K. In (b), (c), and (d) spectra are shifted for clarity, left axis is valid for $B = 11$ T in σ^- polarization.

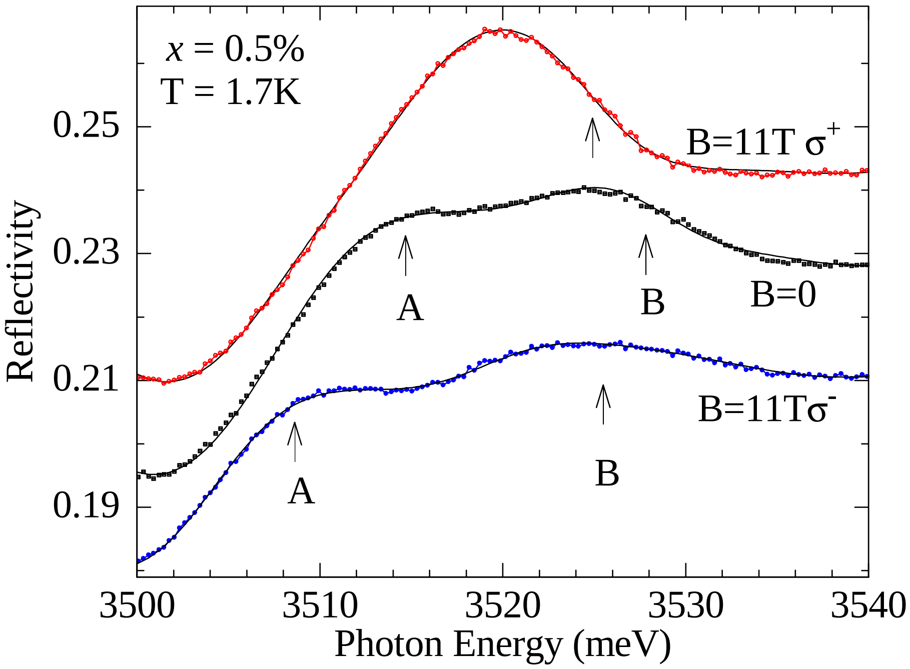

Figure 5.22: Details of the reflectivity spectra shown in Fig. 5.21(b) for the sample with $x = 0.5\%$ (sample ♯E766) at $T = 1.7$ K ; experimental spectra are shown by dots, and calculated spectra by solid lines. The values of exciton energy used in the calculation and plotted in Fig. 5.23 (filled circles), are shown by vertical arrows.

dex of 1.8. (it corresponds to sapphire at $\lambda = 350$ nm). The total reflectivity of the structure was then calculated, and therefore, interferences within the thin epilayer are automatically taken into account. As an example, Fig. 2 displays the fit of experimental spectra recorded in zero field and at 11 T. The values of exciton energy entering this fit are shown by arrows in Fig. 5.22 and by full circles in Fig. 5.23. A simpler method to determine the field dependence of the exciton energy is based on the determination of a characteristic point in the spectra. We have chosen the maximum of reflectivity and the maximum of the absorption derivative, and these maxima were determined either by visual pointing or by a local fit with two Gaussian lines. All methods give very similar results, as shown by different symbols in Fig. 5.23. In particular, the redshift of exciton A was the same, to within 1 meV, for all methods. We take this value of 1 meV as our experimental accuracy in the determination of the redshift of exciton A. The accuracy in the determination of the position of exciton B is significantly worse, ±2 meV. Finally, in σ^+ polarization at $B > 3\ T$, excitons A and B merge, therefore the only feature which remains, is marked in Fig. 5.23 with error bars taken as the value of the $A - B$ splitting for the last resolved spectra. We will come back later on to the redshift of exciton A, which provides us with a particularly easy way of measuring a quantity proportional to the magnetization.

We use the excitonic model described in Sec. 4.5.3 to fit the experimental data shown in Fig. 5.23. The fitting parameters were determined as follows : we used

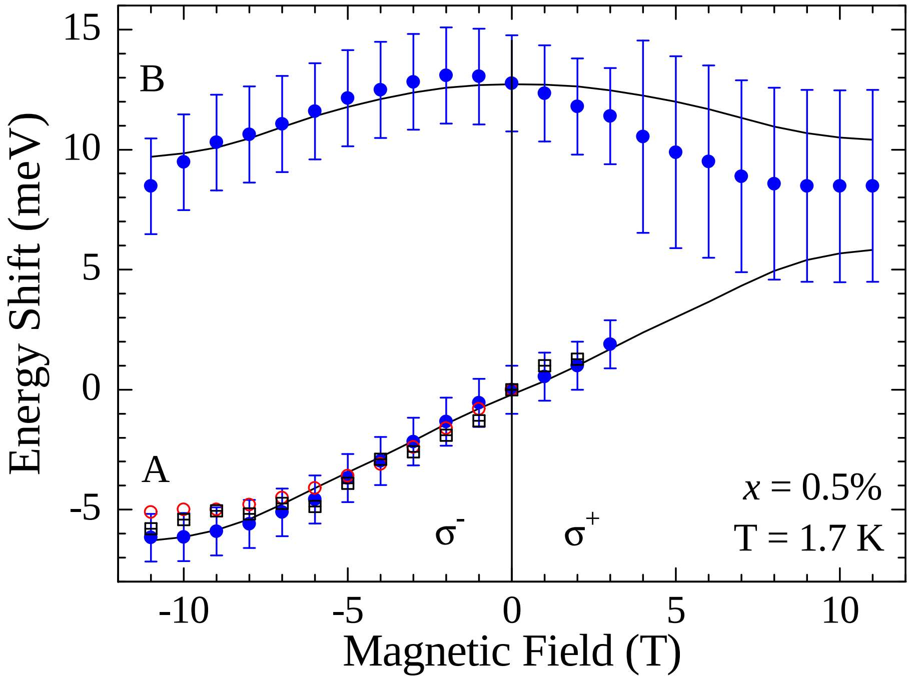

Figure 5.23: Zeeman shifts of excitonic transitions determined from the fit of reflectivity spectra (filled circles, blue color), from the reflectivity maxima (empty squares, black), and from the maxima of absorption derivative (empty circles, red), at T = 1.7 K and $B||c$. Corresponding spectra are shown in Figs. 5.21(b), 5.21(d), and Fig. 5.22. Solid lines represent the excitonic shifts calculated using the model and with parameters as discussed in text. Sample ♯E766.

$\Delta_3 = 5.5$ meV, $\gamma = 0.6$ meV as reported for pure GaN,[89,104] and $N_0\alpha = 0.2 \pm 0.2$ eV. Then, we calculated the mean spin of Mn^{3+} $\langle\text{-}S_z\rangle$ from the Eq. (3.7). Finally, we fitted the data by keeping $\tilde{\Delta}_1$, Δ_2, and $N_0(\beta - \alpha)$ as free parameters. The best fit was obtained with $\tilde{\Delta}_1 = 11$ meV and $\Delta_2 = 10$ meV, and we determined $N_0(\beta - \alpha) = 1.2 \pm 0.2$ eV.

In practice, the value $N_0(\beta - \alpha) = 1.2 \pm 0.2$ eV, obtained from the fit above, can be read directly on the slope of exciton A in σ^- polarization. The latter method will be used for a whole series of samples below.

A separate determination of $N_0\alpha$ and $N_0\beta$ would require to fit the giant Zeeman shift of exciton C, which is governed by $N_0(\alpha+\beta)$, or to have a stronger anticrossing between excitons B and C at high field (*i.e.*, higher Mn concentration or smaller $\tilde{\Delta}_1$). Reflectivity spectra of a sample with a larger Mn content are shown in Fig. 5.24. The Zeeman shift of exciton B in σ^- polarization increases significantly the mixing with exciton C. As a result, at high field, exciton C acquires an oscillator strength sufficient to be observed. This is in good qualitative agreement with the predictions of the exciton model, but the linewidth is too large and precludes any quantitative study.

An important result discussed in Sec. 4.5.3 is that generally speaking, the giant Zeeman splitting of excitons A and B is not proportional to the Mn magnetization.

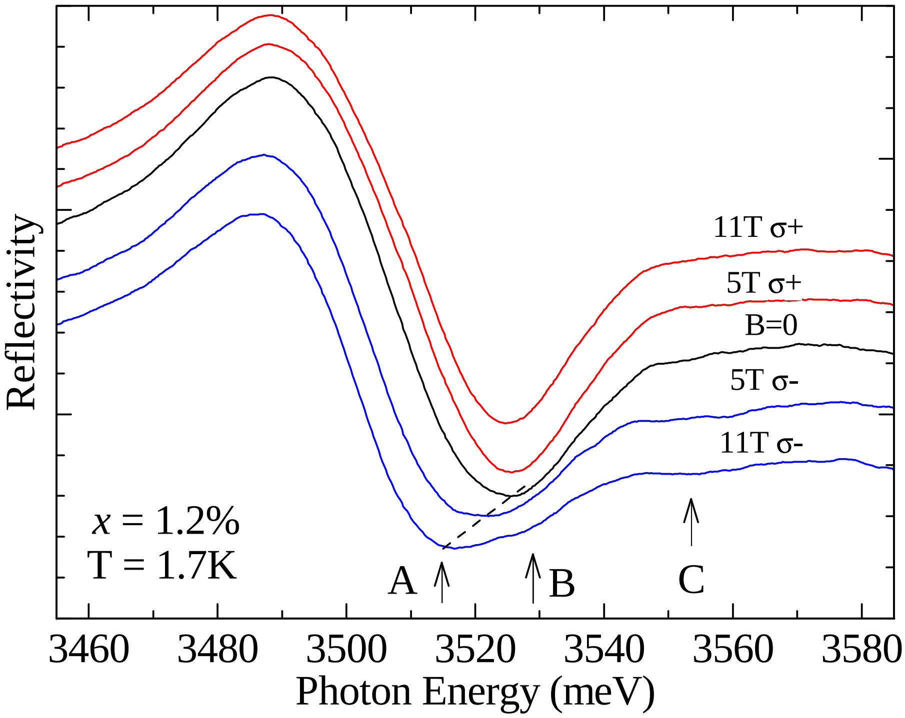

Figure 5.24: Reflectivity of the sample ♯E364c with the highest Mn concentration $x = 1.2\%$. Due the increase of the linewidths, excitons A and B are not resolved in zero field and in σ^+ polarization. Nevertheless, the giant Zeeman effect can be clearly observed by the redshift of exciton A in σ^- polarization (the dashed line is a guide for the eye). In the same polarization, the blue shift of exciton B increases the mixing between excitons B and C, so that exciton C can be observed at high field.

In order to probe the giant Zeeman energy $[N_0(\alpha - \beta)\ x\langle -S_z\rangle]$, one should rather use the redshift of exciton A in σ^- polarization, which appears to be proportional to the magnetization as shown by the straight line in Fig. 4.3. This redshift of A is well accounted for over a large range of fields and temperatures, as shown in Fig. 5.25, where the mean spin of Mn^{3+} is calculated using Eq. (3.7). Both saturate only at the lowest temperature and the highest magnetic field, in agreement with the fact that the field is applied along the hard magnetization axis of the strongly anisotropic Mn^{3+} ion. Any contribution from Mn^{2+} ions would saturate at low field (3 T), as does the Brillouin function for d^5. From the data presented in Fig. 5.25, we conclude that such a contribution should be at least one order of magnitude weaker than the Mn^{3+} contribution. This agrees with the negligible Mn^{2+} content ($x < 0.01\%$) estimated using EPR[83] on the same sample, compared to the Mn^{3+} content equal to $x = 0.5\%$, determined from d-d absorption.

This magnetooptical study was extended to a whole series of samples [see Fig. 5.26]. For higher Mn concentrations than $x = 0.5\%$, the behavior of A and B excitons under magnetic field is qualitatively similar (see Fig. 5.24), but the line broadening prevents any precise fit of the spectra. Nevertheless, the giant Zeeman effect can be unambiguously determined using the Zeeman shift of exciton A in σ^- polari-

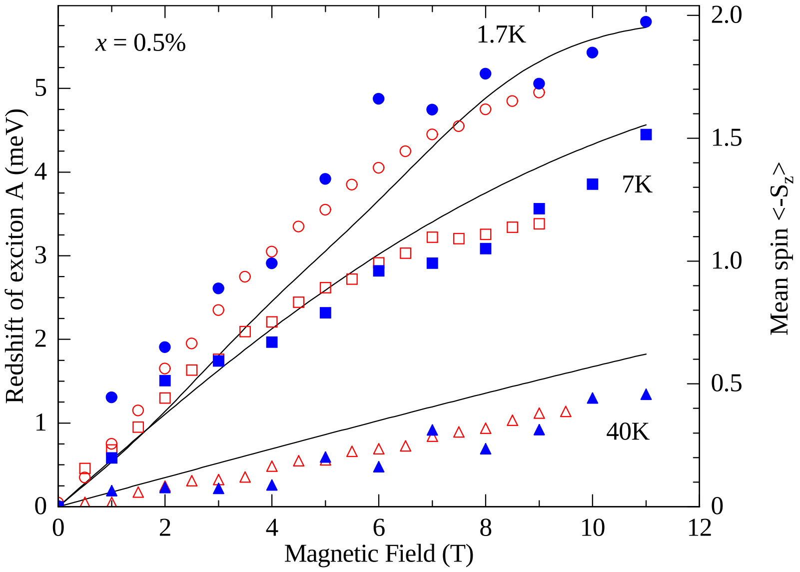

Figure 5.25: Redshift of exciton A determined using reflectivity (full symbols, blue color) and absorption (empty symbols, red color), compared to the mean spin of Mn^{3+} (solid lines, right axis) calculated using Eq. 3.7, for temperatures 1.7, 7, and 40 K. Sample ♯E766.

zation. As expected, it increases with the Mn^{3+} content determined from intra-ionic absorption. In Fig. 5.26, it is compared as usual to the effective concentration $x_{\mathrm{eff}} = x(1-x)^{12}$, rather than the total concentration x, which accounts for the small non linear variation of the redshift. x_{eff} corresponds to the density of Mn impurities with no magnetic ion over the 12 nearest-neighbors present in the Ga sublattice[71] and is used to take into account an antiferromagnetic blocking of the Mn-Mn nearest neighbor pairs at low temperature. As shown in Fig. 5.26, the value $N_0(\beta-\alpha) = 1.2 \pm 0.2$ eV determined previously accounts well for the giant Zeeman effect observed in the whole concentration range. We can note that a spin splitting of exciton A of about 20 meV can be obtained with a Mn concentration of about 1%.

5.4.3 Discussion

The redshift of exciton A in σ^- polarization unambiguously points to a positive sign of $N_0(\beta-\alpha)$. So far, $|N_0\alpha|$ has been reported to be small (< 0.3 eV) and almost constant for all DMS, and there is no theoretical hint that the case of GaN-based DMS could be different. Then, $N_0(\beta-\alpha) = 1.2$ eV means that β is positive for GaN :Mn^{3+}. If we assume a usual value, $N_0\alpha = 0.2 \pm 0.2$ eV, with error which take into account eventual reduction of effective $N_0\alpha$ to zero,[126,127] we deduce $N_0\beta = +1.4 \pm 0.4$ eV, which means a ferromagnetic interaction between the magnetic ions and the holes.

A positive β was rarely observed in DMS. A known exception[102,128] is Cr in II-VI DMS, where Cr has the same $3d^4$ electronic configuration as Mn^{3+} in GaN. This could suggest that a less than a half-filled d-shell would be responsible for a positive

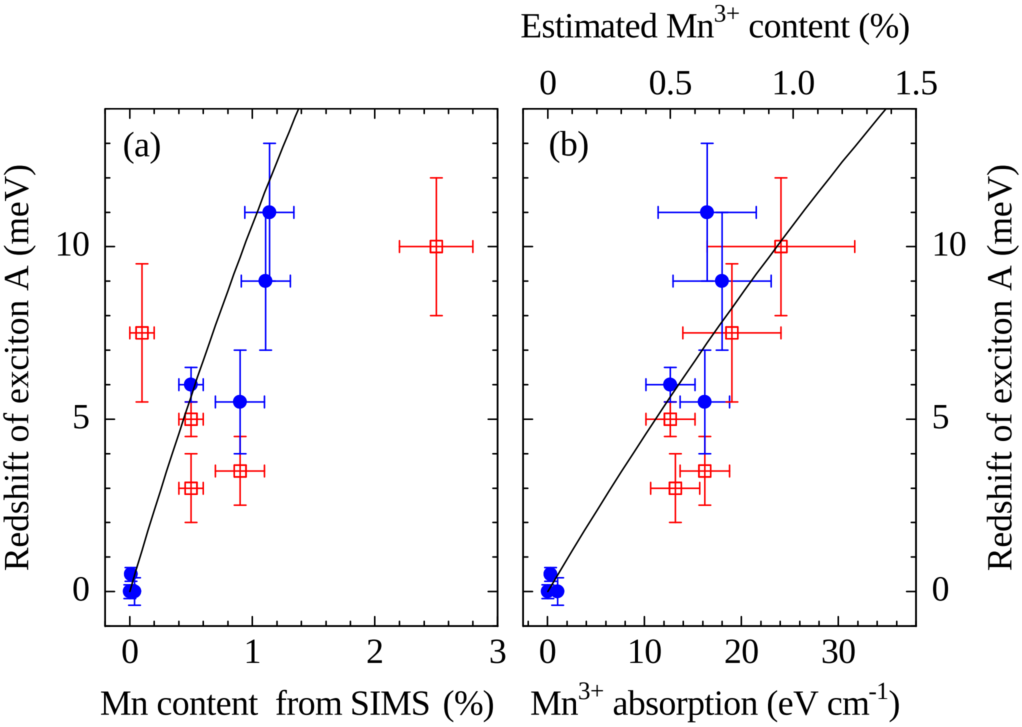

Figure 5.26: Giant Zeeman shift (redshift) of exciton A at saturation versus Mn concentration determined from SIMS (a) and versus absorption of Mn^{3+}(b). The redshift is determined using reflectivity (full circles, blue color) and absorption (empty squares, red color). Solid lines represent value of the shift $\Delta E_A = 1/2N_0(\beta-\alpha)x_{\text{eff}}\langle -S_z\rangle$ calculated with $N_0(\beta-\alpha) = 1.2$ eV, $\langle\text{-}S_z\rangle = 2$, $x_{\text{eff}} = x(1-x)^{12}$.

β. However this analogy is probably misleading, because it is essentially the position of the donor and acceptor levels which governs the sign of β (Refs. 129 and 130).

A negative value of $N_0\beta$ has been deduced from x-ray spectroscopy[131] of $\text{Ga}_{1-x}\text{Mn}_x\text{N}$ layers where Mn ions have been observed to be in the 2+ configuration. In our samples, the present magnetooptical observation of the d^4 electronic configuration of Mn in GaN is consistent with XANES (x-ray absorption near edge spectroscopy) measurements performed at the K-edge,[132] infrared absorption,[47,52] magnetic anisotropy,[133] and EPR.[83] It would be interesting to understand whether the different electronic configuration originates from an observation of different samples with different Fermi levels, or a sensitivity to different part of the samples (high sensitivity to the surface in the case of photoemission). Another possible explanations will be discussed in Chapter 6.

5.5 Spectroscopy of $\mathbf{Ga_{1-x}Fe_xN}$

We studied $Ga_{1-x}Fe_xN$ layers with a very low concentration of iron ($x < 0.21\%$). Therefore, effects of s,p-d exchange interactions are expected to be weaker than in the case of previously analyzed samples of wide gap DMS. In the case of diluted limit, one should consider taking into account the direct influence of magnetic field on excitons due to Zeeman effect and diamagnetic shift (see Sec. 4.6). Hence, we started our study by a careful characterization of the Zeeman effect in pure GaN. Fortunately, one sample (♯590) from the studied series of MOVPE layers is intentionally free of iron, so we had a possibility to have the same parameters of the sample as in $Ga_{1-x}Fe_xN$ study.

5.5.1 Reflectivity of GaN

Fit to the zero-field spectrum

Fig. 5.27 presents zero field reflectivity spectra of GaN. A comparison to very similar spectra from Ref. 134 allows us to identify 5 well defined excitonic structures : 1S states of A, B, and C excitons (labeled as : $X_A^{n=1}$, $X_B^{n=1}$, and $X_C^{n=1}$) and two exciton 2S states : $X_A^{n=2}$ and $X_B^{n=2}$. Their exact energy positions (see Table 5.4) have been determined using a fit with a polariton model for two excitons (A and B, Sec. 4.7.1) and the residual dielectric function including exciton C, all excited states of A, B, and C, and the continuum of band-to-band transitions (Sec 4.7.2). By fitting the spectra, we found the effective Rydberg energy 25.2 meV for exciton A and 21.7 meV for exciton B. In a simple spherical model, this energy is enough to calculate the relative position of all excited states, however only 2S states are resolved. The determination of effective Rydbergs was very important for us, because a quite large range of effective Rydberg in GaN from 20 meV[113] up to 26.5 meV[117] are reported in literature. We will use our values of R^* for the description of $Ga_{1-x}Fe_xN$, where excited states are not resolved, but contribute to the reflectivity spectra.

Table 5.4 list fitting parameters. There are 5 parameters for each series of A, B, and C excitonic transitions : polarizability ($4\pi\alpha_0$), energy position, and broadening of 1S exciton, effective Rydberg energy (R^*) and broadening of continuum. The position of 2S exciton was not used as a fitting parameter, it is given by $E_{n=1}+3/4R^*$, we list it only for clarity. Also, effective Rydberg energy for exciton C was not fitted, we only checked if literature data,[117] $R^* = 26.5$ meV, can describe properly our spectrum (the answer is yes, it fits well). Following Ref. 113, we have taken a background dielectric constant $\epsilon_0 = 5.2$, an effective mass of excitons equal to m_e, and we used an identical mass for both A and B excitons. Since we neglect the spatial dispersion of exciton C, we do not need the corresponding effective mass. We have found from fit that $\gamma_{n\to\infty}$ does no vary significantly between A, B, and C. Hence, it is reasonable to limit further the number of fitting parameters, and use only one common $\gamma_{n\to\infty}$ for all three transitions.

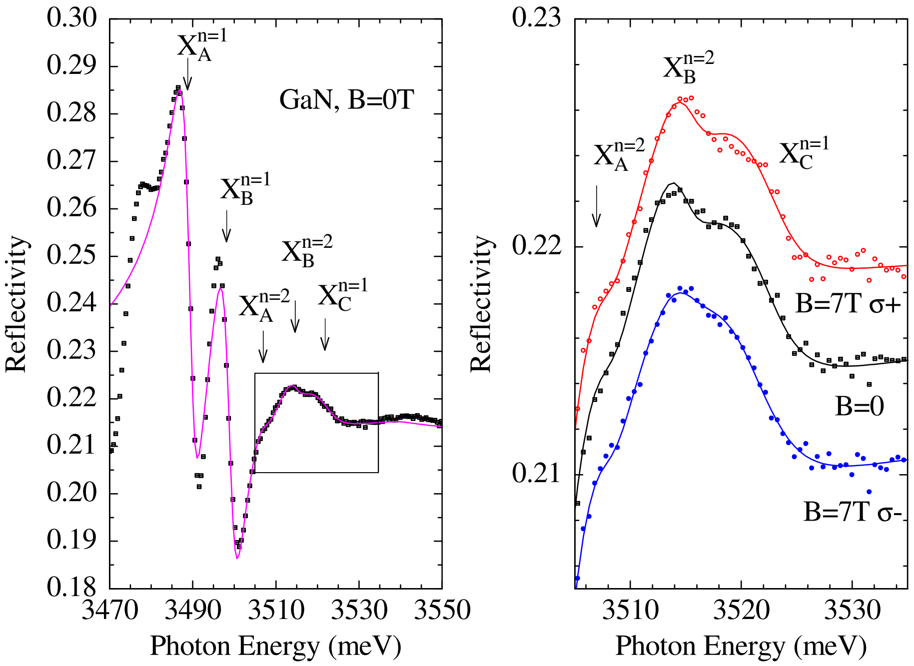

Figure 5.27: (a) Reflectivity of GaN at 1.5 K, $B = 0$ T (b) Reflectivity in spectral region of exciton C. Zero field spectrum (middle), and spectra measured in Faraday configuration, at $B = 7$ T (σ^+ and σ^- helicity). Sample ♯590.

Exciton	Polarizability $4\pi\alpha_0$	Position $E_{n=1}$	Broadening $\gamma_{n=1}$	Rydberg R^*	Broadening $\gamma_{n\to\infty}$	Position $E_{n=2}$
A	$6.6\ 10^{-3}$	3488.6	3.7	25.2	7.6	3506.9^b
B	$4.4\ 10^{-3}$	3498.3	4.0	21.9	7.2	3514.7^b
C	$0.5\ 10^{-3}$	3521.8	8.2	26.5^a	8.2	3541.7^b

[a] Value determined by Kornitzer *et al.*; Ref 117.

[b] We use approximation, where $E_{n=2} = E_{n=1} + 3/4R^*$ at zero field.

Table 5.4: Parameters describing zero field reflectivity spectrum of pure GaN grown on (Ga,Al)N (sample ♯590.), plotted in Fig. 5.27(a). Unit is meV for all the parameters except for polarizability, which has no unit.

Zeeman effect and diamagnetic shift

We have measured the reflectivity of GaN in the Faraday configuration, with magnetic field (up to 7 T) parallel to the c-axis. We analyzed spectra using two fits. First we fitted energy position of A and B excitons keeping constant other parameters listed in Table 5.4, and we obtained energies shown by symbols in Fig. 5.28(b,c). Next we fitted spectral region above exciton B, with fitting parameters : energy position, oscillator strength, and damping parameter of exciton C, and energy position of 2S excitons. We obtained solid lines shown in 5.27(b), and energy position of exciton C show in Fig. 5.28(a).

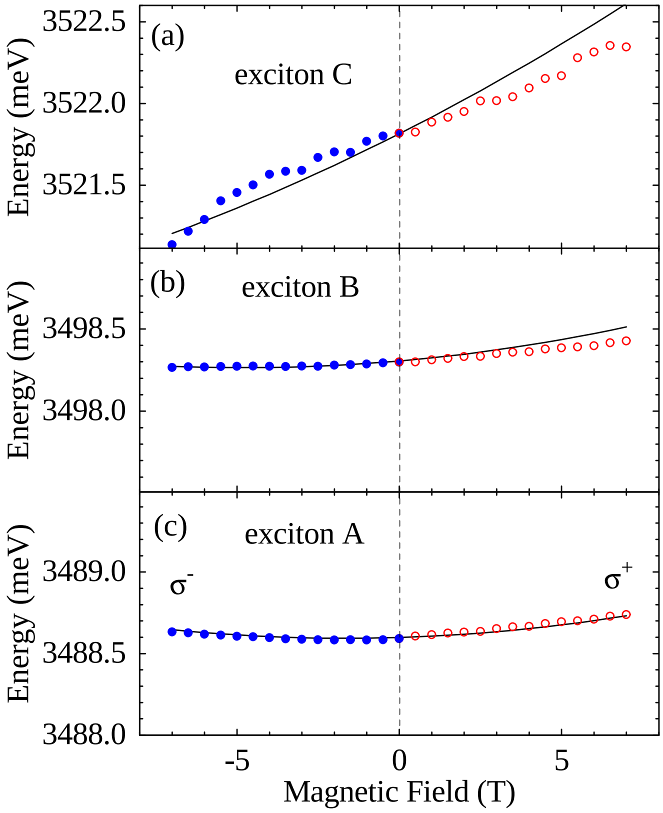

Figure 5.28: Transition energy of the A, B, and C excitons of GaN determined from magneto-reflectivity measured in Faraday configuration at 1.5K (points) and calculated (solid lines) using Eqs (4.15), (4.16), (4.17), (4.1), (4.10), and parameters of Ref. 93 : $\tilde{\kappa} = -0.36$ for holes, $g_e = 1.95$ for electrons, and excitonic diamagnetic shift d=1.8 μeV/T^2. Sample ♯590.

Excitons A and B of pure GaN shift very weakly. The Zeeman splitting determined by fitting the spectra is about 0.11 meV for exciton A, and about 0.16 meV for exciton B (see Fig. 5.28). The diamagnetic shift for these two excitons was found about 2 μeV/T^2 and 1 μeV/T^2, respectively. Much more pronounced magnetooptical effects are shown in the spectral region near exciton C (Fig. 5.27b). The Zeeman splitting of exciton C, was found to be 1.2 meV with an significant error, about ±0.3 meV, because exciton C is hardly resolved. The diamagnetic shift of 2S exciton B, was found to be about 10 μeV/T^2. An increase of the diamagnetic shift with the radius of the exciton is in fact expected from the theory, so it is reasonable that diamagnetic shift is significantly larger for 2S exciton in comparison to 1S. It is interesting, that all found excitonic splittings have the same signs : upper component is observed in σ^+ polarization, and lower, in σ^- polarization. We will keep this in mind for the analysis of the circular polarization of $Ga_{1-x}Fe_xN$.

We compared the excitonic splittings determined from fit to the values calculated using the excitonic model. We have taken into account the following terms : hamiltonian of the valence band in wurtzite structure (4.1), Zeeman splitting of the valence band (4.16), Zeeman splitting of the conduction band (4.15), excitonic diamagnetic shift (4.17), and electron-hole exchange interaction (4.10). We used three parameters from Ref. 93 : an effective Luttinger parameter $\tilde{\kappa} = -0.36$, an electron g-factor $g_e = 1.95$, a diamagnetic shift 1.8 μeV/T^2, and we used our zero-field position of excitons. The calculated values of the transition energies are shown by solid

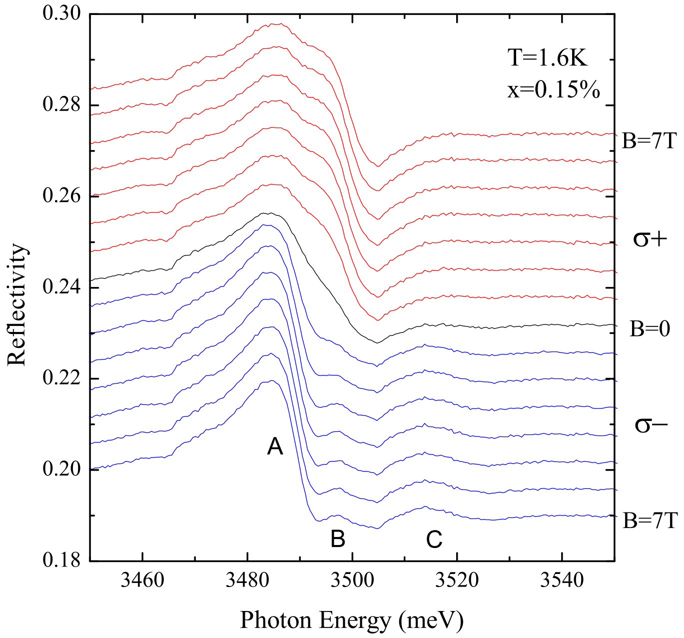

Figure 5.29: (a) Reflectivity of $\mathrm{Ga}_{1\text{-}x}\mathrm{Fe}_x\mathrm{N}$ with $x = 0.15\%$ (sample ♯647) at $T = 1.6$ K, in Faraday configuration. In σ^- polarization (see bottom spectrum) A, B, and C excitons are well resolved. Exciton C is much weaker in σ^+ polarization (see upper spectra).

lines in Fig. 5.28. At $B = 7$ T, values of the splittings are 0.09 meV for exciton A, 0.24 meV for exciton B, and 1.40 meV for exciton C, with the same sign for all three excitons (σ^+ at higher energy). There is quite a good agreement between our data and theory, similar to the one reported in Ref. 135. Moreover, a simple change of the value of $\tilde{\kappa}$ will be not enough to recover full agreement of the theory and our experiment. Therefore, we decided to use further parameters of Ref 93, which were determined at high magnetic fields.

5.5.2 Giant Zeeman effect of A, B, and C excitons

Magneto-reflectivity spectra were measured, as usually in this work, in the Faraday configuration, with the magnetic field parallel to the common c-axis of the crystal and the optical axis of the experimental setup. Fig. 5.29 shows reflectivity of $\mathrm{Ga}_{1-x}\mathrm{Fe}_x\mathrm{N}$ with $x = 0.15\%$. We observed A, B and C excitons which shift under magnetic field due to s,p-d exchange interactions. In σ^- circular polarization A and B excitons separate, and B and C excitons get closer. In σ^+, the situation is opposite.

We determined the energy position of excitons using a fit with the polariton model. Fig. 5.30(a,b) presents spectra and polariton fit for $\mathrm{Ga}_{1-x}\mathrm{Fe}_x\mathrm{N}$ samples with $x = 0.11\%$ and $x = 0.15\%$, at zero field and at $B = 3$T in σ^- and σ^+ circular polarizations.

The procedure of fitting the reflectivity spectra of $\mathrm{Ga}_{1-x}\mathrm{Fe}_x\mathrm{N}$ with polariton model requires for each exciton 3 fitting parameters : polarizability, energy position,

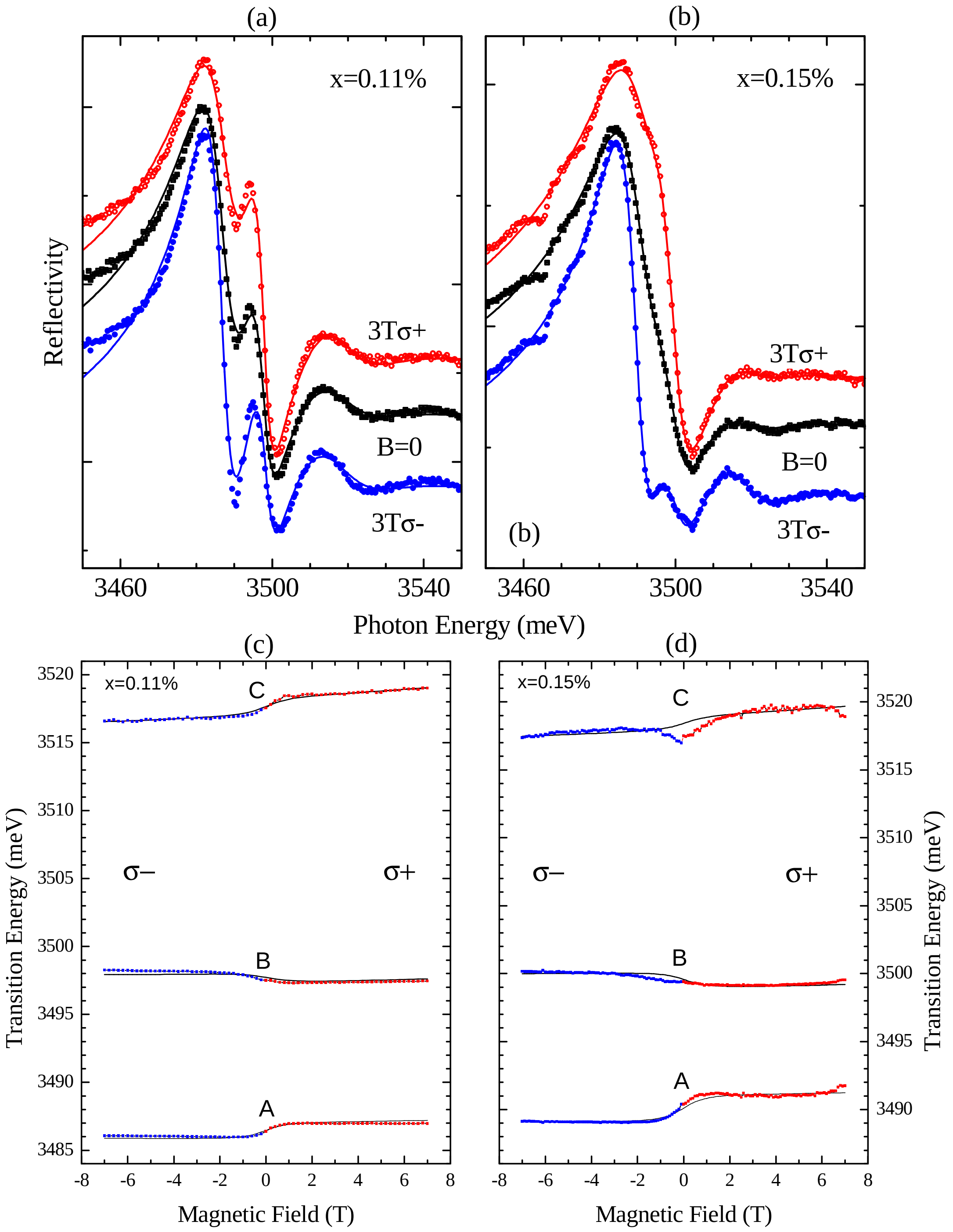

Figure 5.30: (**a,b**) Reflectivity spectra of Ga$_{1\text{-}x}$Fe$_x$N with $x = 0.11\%$ [sample ♯588] (a) and $x = 0.15\%$ [sample ♯647] (b) measured at $T = 1.6$ K. Points are experimental data, continuous curves represent fits with polariton model.

(**c,d**) Transition energies determined from reflectivity spectra above are shown by points for Ga$_{1\text{-}x}$Fe$_x$N with $x = 0.11\%$ [Sample ♯588] (c) and $x = 0.15\%$ [Sample ♯647] (d). Lines represent fits with our excitonic model and fitting parameters given in Table 5.5.

and damping. One additional parameter Γ_∞ is enough to approximately describe all other transitions. From theoretical point of view, any of these parameters can evolve with magnetic field. Energies change due to s,p-d interactions, Zeeman effect, and diamagnetic shift. The oscillator strength (polarizability) is exchanged between excitons A and B due to electron hole exchange interaction, when their energy separation changes. Excitons B and C exchange oscillator strength when they anticross due to spin-orbit interaction. Moreover, the studied samples are inhomogeneous : there are regions containing higher Fe concentration, which exhibit shifted transition energy in comparison to more diluted ones. Under magnetic field, regions with different concentration exhibit different exchange shifts. As a consequence, linewidths decrease with excitonic redshifts, and increase with excitonic blueshifts. A similar change of broadening has been already observed in II-VI DMSs.[136] The same argumentation leads to the conclusion, that Γ_∞ can also evolve with magnetic field, but we decided to limit fitting parameters to 9 as mentioned above.

The points in Fig. 5.30 (c,d) show the excitonic shifts determined for the samples presented in Fig. 5.30 (a,b). All observed magnetic field shifts are well described using a Brillouin function $B_{5/2}$ with real experimental temperature and fit with our excitonic model which is shown in Fig. 5.30 (c,d) by solid lines. Comparing to other sections, we use here the most advanced model. The field dependance of the exciton energies is calculated for the hamiltonian

$$H = E_0 + H_{\mathrm{v}} + H_{\mathrm{e-h}} + H_{\mathrm{Z}} + H_{\mathrm{diam}} + H_{sp-d}, \tag{5.5}$$

where E_0 is the band-gap energy and H_{v} describes the valence band at $k = 0$, in semiconductors with the wurtzite structure (4.1). This term includes the trigonal component of both crystal field and biaxial strain as well as the anisotropic spin-orbit interaction. The component $H_{\mathrm{e-h}}$ describes the electron-hole interaction within the exciton (4.10). Effects linear in the magnetic field are taken into account by the standard Zeeman hamiltonian for excitons H_{Z} which is a sum of (4.16) and (4.15). The diamagnetic shift is described by a single term quadratic in the magnetic field, H_{diam} given by (4.17). Finally, $H_{sp-d} = H_{p-d} + H_{s-d}$ is the exchange interaction between Fe ions and free carriers, sum of (4.2) and (4.3).

The fitting parameters are summarized in the Table 5.5. They are : zero-field position of the lowest exciton E_A, crystal field with strain $\tilde{\Delta}_1$, spin orbit interaction Δ_2, s,p-d exchange integral difference $N_0(\beta - \alpha)$, and s,p-$d$exchange integral sum $N_0(\beta + \alpha)$. Other parameters required for calculation of transition energies were taken from literature : $\Delta_3 = 5.5$ meV[104] and $\gamma = 0.6$ meV,[89] as reported for pure GaN at zero field, and parameters of Ref. 93 for magnetic field effects in pure GaN : $g_e = 1.95$ for electrons, $\tilde{\kappa} = -0.36$ for holes, and excitonic diamagnetic shift $d = 1.8$ μeV/T^2.

A similar analysis to that shown in Fig. 5.30 has been done for sample with a higher Fe concentration ($x = 0.21\%$), where the determination of the position of the exciton C was not possible. Reflectivity spectra with polariton fits are show in Fig 5.31(a). The determined energies of the excitons A and B are shown in Fig 5.31(b). A fit with exciton model leads to the parameters given in the last row of Table 5.5.

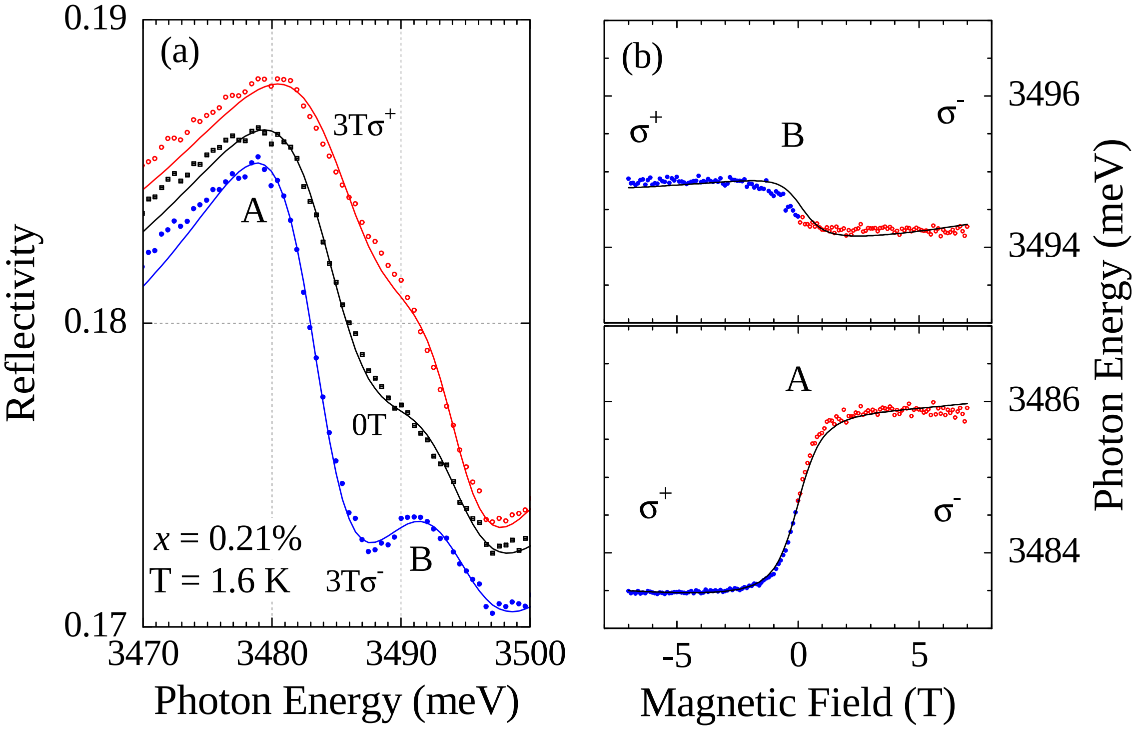

Figure 5.31: (a) Reflectivity spectra (symbols) of $Ga_{1\text{-}x}Fe_xN$ with the highest accessible Fe concentration, $x = 0.21\%$ [Sample ♯589]. Solid lines represent fits with polariton model. (b) Transition energies (symbols) determined from fits to the reflectivity spectra shown in (a). Solid lines represent the fit with exciton model and parameters shown in Table 5.5.

Sample	Fe content	E_A	$\tilde{\Delta}_1$	Δ_2	$N_0(\beta-\alpha)$	$N_0(\beta+\alpha)$	Figures
♯588	0.11%	3486.4	19.4	7.5	+0.44 eV	+0.60 eV	Fig. 5.30(a,c)
♯647	0.15%	3490.1	16.9	6.7	+0.54 eV	+0.48 eV	Fig. 5.30(b,d)
♯589	0.21%	3484.6	15.5	7.2	+0.46 eV	+0.63 eV	Fig. 5.31(a,b)

Table 5.5: Fe concentration and fitting parameters describing giant Zeeman effect in three $Ga_{1-x}Fe_xN$ samples. Values of transition energy of the lowest exciton E_A, crystal field parameter $\tilde{\Delta}_1$, and spin orbit parameter Δ_2 are given in meV. Exchange integrals $N_0(\beta-\alpha)$ and $N_0(\beta+\alpha)$ are in eV.

The detailed analysis of the hamiltonian 5.5 shows that the giant Zeeman shifts of excitons A and B are mainly governed by $N_0(\beta-\alpha)$. Moreover, exciton A, which in GaN is formed from the valence band states with parallel spin and orbit (Γ_9 state), shifts to low energies in σ^- polarization : hence the exchange integral difference $N_0(\beta-\alpha)$ is positive. At the same time, exciton B is mixed with exciton C, whose shift at low magnetic fields is primarily controlled by $N_0(\beta+\alpha)$ and at high magnetic fields by Zeeman effect. Hence, by incorporating exciton C in our description of the reflectivity spectra, we can evaluate independently the exchange energy $N_0\beta$ for the valence band and the exchange energy $N_0\alpha$ for the conduction band. This

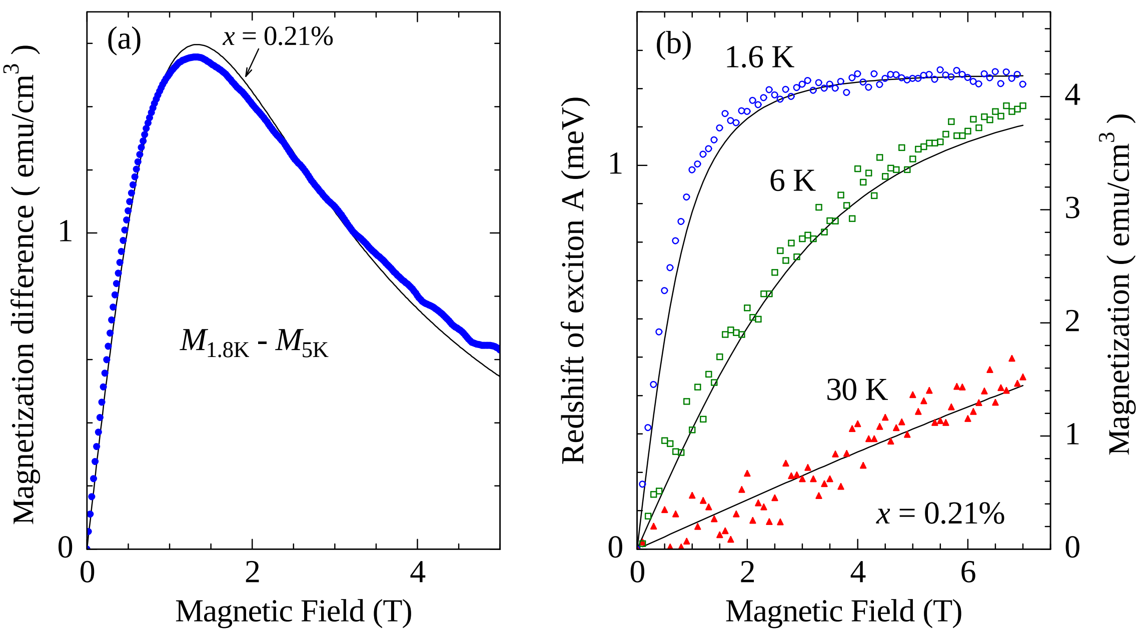

Figure 5.32: $Ga_{1-x}Fe_xN$ with the highest accessible Fe concentration, $x = 0.21\%$ [Sample 589]. (a) Difference between magnetization at 5K and 1.8 K (points) and theoretical difference between Brillouin function calculated for 5 K and 1.8 K. There is only one fitting parameter : concentration of Fe, which appears to be $x = 0.21\%$. (b) The redshift of exciton A determined for 3 temperatures (left axis), as a function of magnetic field, is compared to the magnetization (right axis), given by saturation of magnetization determined in (a) and Brillouin function (3.4) with the same temperature as set in experiment (there is no effective temperature). Adjusting of the left and right axis corresponds to the value $N_0(\beta - \alpha) = 0.47$ eV.

determination is quite accurate in the case of the 0.11% and 0.15% samples, for which exciton C is spectrally well resolved, but an estimation is still possible in the 0.21% sample through its effect on exciton B. From the shifts of B and C, we find that the sign of $N_0(\beta + \alpha)$ is also positive, and its value is quite close to that of $N_0(\beta - \alpha)$, see Table 5.5. Hence, $|N_0\alpha|$ is much smaller than $|N_0\beta|$, and $N_0\beta$ is positive. More precisely, the complete fit yields the values of the exchange energies $N_0\beta = +0.5 \pm 0.2$ eV and $N_0\alpha = +0.1 \pm 0.2$ eV. The role of the classical Zeeman effect is really important only for the description of the shift of exciton C. This shift is at high fields comparable to the exchange shift.

s,p-d exchange shift vs Brillouin function

The classical s,p-d hamiltonian used in our calculation [(4.2) and (4.3)] gives the prediction of the proportionality of magnetization and giant Zeeman energy ($N_0(\beta{-}\alpha)\, x\langle\text{-}S_z\rangle$) observed by exciton spectroscopy. We verified this proportionality by testing temperature and magnetic field dependence of magnetization and giant Zeeman shift in the sample with the highest accessible Fe concentration. Fig. 5.32(a) shows the difference of magnetizations measured at $T = 1.8$ K and $T = 5$ K, by

Michał Kiecana and Maciej Sawicki from Institute of Physics PAN, Warsaw. We plot only the difference, because the total magnetization signal is dominated by a strong diamagnetic contribution from the substrate with only a weak paramagnetic contribution from thin layer of DMS. Since the diamagnetic contribution from substrate exhibits negligible temperature dependence, the difference between magnetization at $T = 1.8$ K and $T = 5$ K results mainly from the layer of DMS and it is only weakly affected by other magnetic contributions. The curve starts from zero, reaches a maximum near $B = 1.3$ T and then exhibits an asymptotic decrease to zero, because at very high magnetic fields there is almost no temperature dependence (magnetization is close to saturation). The good agreement between experimental data (points) and calculated difference between two Brillouin curves for $T = 1.8$ K and for $T = 5$ K confirms that the magnetization at low temperatures is well described by a Brillouin function. There is only one fitting parameter (magnetization at saturation), which can be translated into an effective concentration $x_{eff} = 0.21\%$. We use the term of effective concentration, because from this experiments we cannot exclude the presence of non paramagnetic ions : antiferromagnetically coupled pairs or complexes or ferromagnetic clusters.

We have already shown in Sec. 4.5.3, that the most efficient measure of the giant Zeeman energy is from the redshift of exciton A. Therefore in Fig. 5.32 (b) we plot shift of exciton A in σ^- circular polarization. The redshift is plotted for three temperatures and values of magnetic field between 0 T and 7 T. The corresponding axis is on the left side. On the right side, the axis shows the magnetization calculated using a Brillouin function and saturated magnetization determined in (a). Excitonic redshift perfectly agree with the magnetization of Fe^{3+}, as expected from theory. By adjusting left and right axis, we can deduce an approximate value of $N_0(\beta - \alpha) = 0.47$ eV. It fit quite well to values determined from fit using excitonic model for this sample and for diluted diluted samples (Tab. 5.5).

5.5.3 Discussion

We studied very diluted $\mathrm{Ga}_{1-x}\mathrm{Fe}_x\mathrm{N}$ samples, so it is natural, that they are paramagnetic, and that their magnetization is well described by a Brillouin function. We note that our evaluation of $N_0\alpha = +0.1 \pm 0.2$ eV includes within the experimental error the values of $N_0\alpha = +0.25 \pm 0.06$ eV found in early studies of Mn-based II-VI DMS (Ref. 137, see also Table 6.2). This agreement confirms that the assumption of a small positive $N_0\alpha$ used for the analysis of others wide gap DMS was reasonable. Surprisingly, our evaluation of $N_0\beta = +0.5 \pm 0.2$ eV is in clear contradiction with the large negative value of $N_0\beta$ expected for the d^5 electronic configuration. The theoretical value $N_0\beta = -2.8$ eV was determined in Ref. 129 for Fe^{3+} electronic configuration of iron in GaN, the same as observed in our experiment. In fact, weak and ferromagnetic type *p*-*d* exchange interaction between the d^5 ions and holes is observed for the first time in quite long history of diluted magnetic semiconductors.

Chapter 6

Discussion

This chapter contains a discussion of the magnetic properties of our samples and the estimated values of p-d exchange integrals. We compare the sign and strength of ion-carrier exchange interaction observed in our magnetooptical measurements on wide gap DMS, to the ion-carrier exchange interaction determined for other DMS materials and determined for materials studied by us, but using other techniques. This comparison evidences surprising differences, which we are trying to understand using various approaches. Finally, we discuss the accuracy of our modèls of wide gap DMS.

Dans ce chapitre, nous discutons les propriétés magnétiques des échantillons et les valeurs estimés des intégrales d'échange p-d. Le signe et la valeur absolue des l'interactions ions-porteurs déduites de nos mesures sont comparés soit aux mesures effectuées avec les mêmes matériaux, mais utilisant d'autres techniques, soit aux mesures effectuées avec d'autres semi-conducteurs magnétiques dilués. Grâce à cette confrontation, nous pouvons mettre en évidence des différences surprenantes que nous cherchons a interpréter par différentes approches. Enfin, nous discutons la validité de nos modeles pour les semiconducteurs magnétiques dilués à large bande interdite.

6.1 Magnetism

In Chapter 5 we presented results of the study of the temperature and magnetic field dependence of excitonic shifts and UV magnetic circular dichroism measured for four wide gap DMS. In each of them, magnetooptical phenomena scale with the magnetization calculated for paramagnetic ions. The magnetization is given by a Brillouin function for the d^5 electronic configuration (Fe^{3+} and Mn^{2+}). For other electronic configurations it is described by a function resulting from the anisotropy (zero-field splitting) of the fundamental state of Co^{2+} and Mn^{3+}. Therefore, the magnetization calculated in Sec. 3.6.1 is well confirmed experimentally. Ferromagnetic behavior has not been found in studied samples. Both signals : excitonic shift and UV MCD are governed by s,p-d exchange interactions. They allow us to study the magnetization of magnetic ions incorporated in the cation sublattice, but we cannot get information about the magnetic properties of other magnetic ions : interstitial ions and ions in precipitates. It means, that we didn't observe ferromagnetism in homogeneous wide gap DMS, but we cannot exclude presence of ferromagnetic precipitates in some our samples.

According to theoretical predictions,[9, 11, 12] paramagnetism, as observed in our samples is not surprising. Carrier induced ferromagnetism requires a high concentration of free holes, while our samples are n-type or semi-insulating. A very weak ferromagnetism has been observed[61] by SQUID and XMCD in n-type $Ga_{1-x}Mn_xN$ with high Mn concentration ($x = 6\%$). Unfortunately, we were not able to observed this ferromagnetic phase using magnetooptical measurements. It was caused by lower optical quality of the ferromagnetic sample. Moreover, we could not use polarization resolved measurements to study ferromagnetism with an easy magnetization axis oriented in the plane of the sample.

6.2 *s*,*p*-*d* exchange integrals

6.2.1 Magnetooptical study of *s*,*p*-*d* exchange interactions

ZnO and GaN based DMS

In Chapter 5 we presented a determination of the following set of data characterizing the strength of *s*,*p*-*d* coupling in ZnO and GaN based DMS (Table 6.1).

Ion	*d*-shell	Host	Our experimental result	Estimated $N_0\beta$
Co^{2+}	d^7	ZnO	$N_0\|\beta-\alpha\| = 0.8 \pm 0.3$	-0.6 ± 0.4 or $+1.0 \pm 0.4$
Mn^{2+}	d^5	ZnO	$N_0\|\beta-\alpha\| = 0.15 \pm 0.05$	$+0.05 \pm 0.15$ or $+0.35 \pm 0.15$
Mn^{3+}	d^4	GaN	$N_0(\beta-\alpha) = 1.2 \pm 0.2$	$+1.4 \pm 0.4$
Fe^{3+}	d^5	GaN	$N_0\beta$=0.5 ± 0.2; $N_0\alpha$=0.1 ± 0.2	$+0.5 \pm 0.2$

Table 6.1: This table summarizes the magnetooptically determined exchange integrals. All values are given in eV. $N_0\beta$ is estimated with assumption that $N_0\alpha = 0.2$ eV, except for $Ga_{1-x}Fe_xN$, where no assumption was needed. There are two estimations of $N_0\beta$ for ZnO based DMS : the first one related to usual valence band ordering, the second one to reversed valence band ordering.

Our quantitative analysis of exciton splittings is consistent with qualitative results obtained using MCD technique : Ando *et al.*[24] have already shown that *s*,*p*-*d* coupling is much stronger in $Zn_{1-x}Co_xO$ than in $Zn_{1-x}Mn_xO$. It is shown in Fig. 6.1 (after Ref. 24), where MCD signals of various ZnO based DMS are shown. There are two types of magnetic ions which induce a large peak near the ZnO energy gap : Co and Fe. There are also three types of ions inducing a very weak MCD signal : Mn, Ni, and Cu. The rest : Sc, Ti, V, and Cr do not enhance magnetooptical effects in ZnO. Joining our quantitative results for two types of ions (Co and Mn) and

MCD signal measured by Ando *et al.*[24] for all other magnetic ions, we can estimate $N_0|\beta-\alpha|$ in ZnO:Fe. It should be close to our value of $N_0|\beta-\alpha| = 0.8$ eV in ZnO:Co, and the sign of the interaction should be the same for both magnetic ions. All other exchange integral differences should be much smaller than $N_0|\beta-\alpha| = 0.8$ eV. Our estimation of $N_0|\beta-\alpha| = 0.15 \pm 0.05$ eV for $Zn_{1-x}Mn_xO$, which is based on the observation of free excitons, is in agreement with $N_0|\beta-\alpha| = 0.1$ eV determined in Ref. 39 using the shift of bound excitons.

$Ga_{1-x}Mn_xN$ has also been studied using MCD technique before our magnetooptical study. Ando[46] demonstrated an MCD signal related to the *s,p-d* exchange interactions, and Marcet *et al.*[47] have shown that the sign of the MCD signal suggests a positive *p-d* coupling. It is in agreement with our results. To our best knowledge, our results on $Ga_{1-x}Fe_xN$ are the first observations of *s,p-d* coupling in this material.

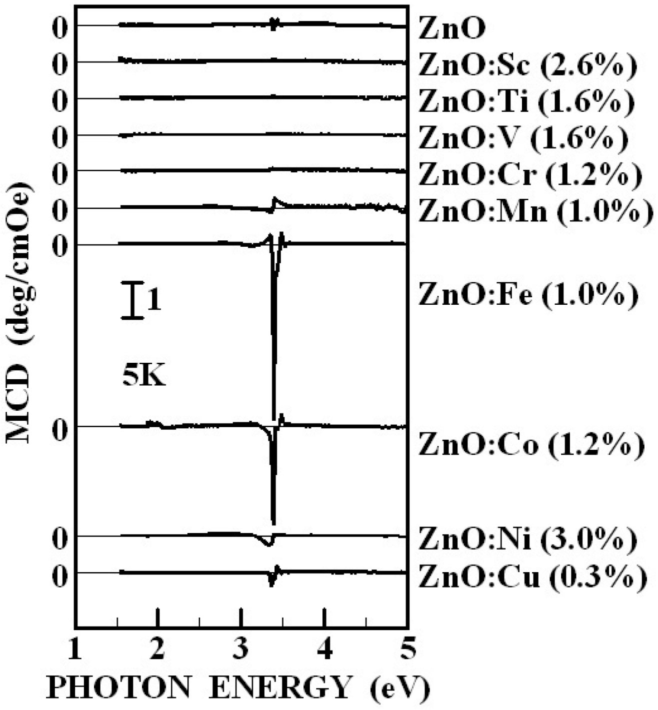

Figure 6.1: After Ando *et al.*, Ref. 24. MCD signal of various ZnO based DMSs.

Summary on other DMSs

Before the huge increase of the interest in wide gap DMS, many other DMS materials were successfully studied using magnetooptical techniques. In Table 6.2 we summarize values of exchange integrals determined for various II-VI DMSs. The table is an updated set of data from Ref. 138.

The optical determination of the exchange integrals in III-V DMS is much more complex than in II-VI materials. In II-VI semiconductors, magnetic ions are isoelectronic centers - they do not introduce carriers. In III-Vs, magnetic ions are usually acceptors. They introduce holes and the density of hole might be even close to the

Ion	d-shell	Host	$N_0\alpha$	$N_0\beta$	Reference
Mn^{2+}	d^5	CdTe	0.22	-0.88	J. A. Gaj *et al.*, Ref. 63
Mn^{2+}	d^5	CdSe	0.23	-1.27	M. Arciszewska and M. Nawrocki, Ref. 101
Mn^{2+}	d^5	CdS	0.22	-1.8[a]	M. Nawrocki *et al.*, Ref. 32
Mn^{2+}	d^5	CdS		-1.55[b]	C. Benoit à la Guillaume *et al.*, Ref. 33
Mn^{2+}	d^5	ZnTe	0.19	-1.09	A. Twardowski *et al.*, Ref. 139
Mn^{2+}	d^5	ZnSe	0.26	-1.31	A. Twardowski *et al.*, Ref. 140
Fe^{2+}	d^6	CdTe	0.30	-1.27	C. Testelin *et al.*, Ref. 141
Fe^{2+}	d^6	CdSe	0.26	-1.53	D. Scalbert *et al.*, Ref. 142
Fe^{2+}	d^6	ZnSe	0.22	-1.74	A. Twardowski *et al.*, Ref. 107
Fe^{2+}	d^6	ZnTe	0.29	-1.50	C. Testelin *et al.*, Ref. 143
Co^{2+}	d^7	CdTe	<0.02	-2.33	H. Alawadhi, *et al.*, Ref. 144
Co^{2+}	d^7	CdSe	0.28	-1.87	M. Nawrocki *et al.*, Ref. 106
Co^{2+}	d^7	ZnTe	0.31	-3.03	M. Zieliński *et al.*, Ref. 145
Co^{2+}	d^7	ZnSe	[c]	-2.22	Liu *et al.*, Ref. 146
Cr^{2+}	d^4	ZnSe	[c]	+0.95	W. Mac *et al.*, Ref. 147
Cr^{2+}	d^4	ZnTe	[c]	+4.25	W. Mac *et al.*, Ref. 147
Cr^{2+}	d^4	ZnS	[c]	+0.62	W. Mac *et al.*, Ref. 147
Cr^{2+}	d^4	CdS	0.22	+0.48	M. Herbich *et al.*, Ref. 102

[a] high x value, see also Ref. 33

[b] reinterpretation.

[c] $N_0\alpha = 0.2$ eV has been assumed.

Table 6.2: Summary of reported exchange integrals $N_0\alpha$ and $N_0\beta$ determined by magnetooptical measurements of II-VI DMS compounds. Units for exchange integral is eV. The Table is an updated set of data from Ref. 138.

concentration of magnetic ions. This leads to carrier mediated ferromagnetism (under special conditions), but this also affects strongly the optical properties. High density of holes leads to a screening of Coulomb interactions (crucial for excitons), electrostatic disorder, and Moss-Burstein effect. As a consequence, direct measurement of the strength of the ion-carrier coupling through the observation of the giant Zeeman splitting of excitons, as routinely performed in II-VI DMS, is generally not accessible in III-V DMSs. Hence, different conclusions have been drawn based on studies of extremely diluted samples[148] or on a complex interpretation of experimental data.[149,150] For $Ga_{1-x}Mn_xAs$, Szczytko *et al.*[149] found $N_0\beta \simeq -2$ eV, but Lang *et al.*[150] found $N_0\beta \simeq +0.9$ eV and $N_0\beta \simeq +2.3$ eV. Therefore the situation seems to be not clear at this moment, so we will not compare our results to magnetooptical results on classical III-V DMS.

By contrast, the situation in II-VI is very clear : magnetic ions with half-filled d-shell : d^5, d^6, and d^7 exhibit negative $N_0\beta$, and magnetic ions with less than half-filled d-shell : d^4 represented by Cr^{2+}, exhibit positive $N_0\beta$. Such an explanation of the sign of $N_0\beta$ has been suggested in Refs. 147 and 102 when positive $N_0\beta$ has been experimentally demonstrated.

The above rule could explain magnetooptical results obtain for $\mathrm{Zn}_{1-x}\mathrm{Co}_x\mathrm{O}$ and $\mathrm{Zn}_{1-x}\mathrm{Mn}_x\mathrm{O}$ (if valence band ordering is usual one), and it could explain positive $N_0\beta$ in $\mathrm{Ga}_{1-x}\mathrm{Mn}_x\mathrm{N}$, where we found Mn ions in the d^4 configuration (the same configuration as in Cr^{2+}). But positive $N_0\beta$, observed by us in $\mathrm{Ga}_{1-x}\mathrm{Fe}_x\mathrm{N}$ with d^5 configuration does not match this rule. As a consequence, we are sure that our results are not a simple continuation of Table 6.2, and we are forced to search for a more advanced model to explain our results.

6.2.2 The Schrieffer-Wolf formula

In the previous section, we have shown, that the most amazing of our results is the positive value of $N_0\beta$ in $\mathrm{Ga}_{1-x}\mathrm{Fe}_x\mathrm{N}$. We will show that such a positive sign is not excluded by the theory of *p*-*d* exchange interaction for d^5 configuration. Larson *et al*[151] derived from Schrieffer-Wolf theory[152,153] the equation for the value of $N_0\beta$ in DMS with the d^5 electronic configuration. We give this equation using usual notation (e.g. Ref. 154 or 68) :

$$N_0\beta = -\frac{32V_{pd}^2}{2S}\left(\frac{1}{\epsilon_d + U_{eff} - E_v} + \frac{1}{E_v - \epsilon_d}\right). \tag{6.1}$$

Here V_{pd} is an matrix element describing the hybridization of $3d$ orbitals with the valence band, S is spin of magnetic ion, and the two terms within the parenthesis are energy denominators. ϵ_d is the energy of occupied d-levels, $\epsilon_d + U_{eff}$ is the energy of unoccupied d-levels, E_v is the energy of the valence band edge. If occupied d-levels are below the valence band edge and the unoccupied levels are above the valence band edge, both denominators are positive. Thus $N_0\beta$ is negative. This is the reason for antiferromagnetic *p*-*d* exchange interactions in Mn based II-VI DMS, as shown in Table 6.2. However, one can imagine that occupied d-levels are within the energy gap of wide gap DMS. Then occupied d-levels are above the valence band edge $\epsilon_d > E_v$. This can be stabilized by Fermi level. In such a situation, the second denominator is negative and leads to ferromagnetic *p*-*d* exchange interaction (positive $N_0\beta$).

Eq. (6.1) derived for d^5 configuration can be used to calculate $N_0\beta$ for magnetic ions with d^6 and d^7 configurations, because additional electrons in d^6 and d^7 occupies e orbital, which is not coupled to the valence band in Γ point.[12,155,156] Only occupation of t_2 orbitals is important for the calculation. Therefore d^6 and d^7 configurations also exhibit positive $N_0\beta$, if occupied t_2 orbital is within the energy gap ($\epsilon_d > E_v$).

Comparing to d^5, the occupation of t_2 orbital decreases for d^4 configuration. Hence, the formula for $N_0\beta$ is more complex for this configuration.[12,130,154–156] Bhattacharjee[130] has shown for Cr^{2+}, that the dominant term leads to positive $N_0\beta$, if occupied t_2 levels are within the energy gap.

In conclusion, independently on electronic configuration, $N_0\beta$ derived from Schrieffer-Wolf theory is positive, providing that occupied t_2-levels are within the energy gap.

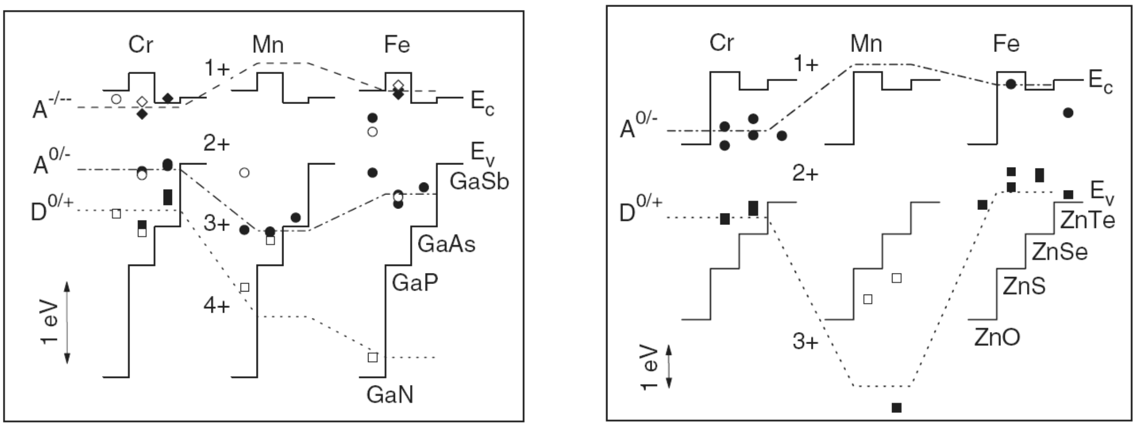

Figure 6.2: After Graf *et al.*, Ref. 157. Charge-transfer levels $A^{-/--}$ (diamonds), $A^{0/-}$ (circles), and $D^{0/+}$ (squares) of the transition metal impurities Cr, Mn, and Fe in Ga-based III-V semiconductors and in Zn-based II-VI semiconductors with the band edges E_c and E_v. Above energies ar based on reference rules, they were derived by Graf *et al.*, but they are still matter of controversy, see e.g. Ref. 55 and 36.

Position of *d* levels : a first example

Fig. 6.2 shows the energy of various ionization levels proposed by Graf *et al.*[157] for Cr, Mn, and Fe in Ga-based III-V DMS and in Zn-based II-VI DMS. The $3+/4+$ (or $D^{0/+}$) level is placed above the top of the valence band for both Mn and Fe in GaN. It determines $\epsilon_d > E_v$ and positive $N_0\beta$ for both Mn^{3+} and Fe^{3+}. In ZnO, $Mn^{2+/3+}$ (or $D^{0/+}$) is placed below the valence band edge, so $\epsilon_d < E_v$ for Mn^{2+}, and consequently $N_0\beta < 0$. We can expect a similar situation for Co^{2+}.

The above analysis can explain all experimentally observed signs of exchange integrals : positive $N_0\beta$ for Fe^{3+} and Mn^{3+} in GaN, and if we assume usual valence band ordering in ZnO, it can eventually explain negative $N_0\beta$ for Co^{2+} and Mn^{2+} in ZnO.

However, this hypothesis has two weak points. First, if occupied *d*-levels are really just above the top of the valence band, Eq. (6.1) leads to a positive $N_0\beta$, but it does not reduce the value of $N_0|\beta|$. Small $\epsilon_d - E_v$ leads to strong increase of $N_0|\beta|$, in disagreement with our experimental observations. Second, a position of *d*-levels derived in Ref. 157 are in significant disagreement with the results of x-ray spectroscopy (discussed in the next section).

p-*d* exchange integrals for 2+ configuration : the Schrieffer-Wolf formula and x-ray spectroscopy

Parameters of Eq. (6.1) can be determined by x-ray spectroscopy,[156,158] and consequently $N_0\beta$ can be calculated independently from magnetooptical measurements. Table 6.3 presents a set of $N_0\beta$ values for II-VI and III-V DMS, determined by this method.

X-ray spectroscopy suggests that there is nothing special in wide gap DMS :

Ion	d-shell	ZnTe	ZnSe	ZnS	ZnO	InAs	GaAs	GaN
Mn^{2+}	d^5	-0.9[a]	-1.0[a]	-1.3[a]	-3.0[b]	-0.7[c]	-1.2[d]	-1.6[e]
Fe^{2+}	d^6		-1.3[f]	-1.5[f]	-2.7[b]			
Co^{2+}	d^7		-2.3[f]	-2.2[f]	-3.4[b]			
Cr^{2+}	d^4		+0.8[f]	-0.5[f]				

[a] Mizokawa *et al.*, Ref. 78
[b] Okabayashi *et al.*, Ref. 123
[c] Okabayashi *et al.*, Ref. 160
[d] Okabayashi *et al.*, Ref. 159
[e] Hwang *et al.*, Ref. 131
[f] Mizokawa *et al.*, Ref. 156

Table 6.3: Summary of reported exchange integral $N_0\beta$ determined using x-ray spectroscopy of II-VI and III-V DMS compounds.

occupied d-levels are located similarly as in other DMS, below the valence band edge. Therefore the sign of $N_0\beta$ remains negative for Mn, Co, and Fe based wide gap DMS. There are no results on Fe in GaN, but we would not expect significant differences comparing to Fe in ZnO or Mn in GaN. Absolute values of exchange integrals determined from x-ray spectroscopy are larger for wide gap DMS, than for other DMS. The hybridization energy scales with the cation density, so it is large for semiconductors with small lattice parameters.

Results of x-ray absorption for ZnO based DMS can be directly compared to our magnetooptical results. Both are related to 2+ configuration. Without any doubt, the value of $N_0|\beta|$ determined by magnetooptical spectroscopy is much smaller than value obtained from x-ray spectroscopy. The case of $Ga_{1-x}Mn_xN$ is more complex. The results of x-ray spectroscopy suggests that Mn is in the 2+ configuration. We observe 3+. If we compare both sets of data, despite of the problem of charge state of Mn in $Ga_{1-x}Mn_xN$, the amplitude of $N_0|\beta|$ is almost the same in both approaches. However, we are sure that the sign of magnetooptically determined $N_0\beta$ in $Ga_{1-x}Mn_xN$ is positive, and it is obtained negative if basing on the results reported for x-ray spectroscopy.

p-d exchange integrals for 3+ configuration : the Schrieffer-Wolf formula and reference rule

It is difficult to compare results of x-ray spectroscopy and magnetooptical results in GaN : x-ray spectroscopy allows Hwang *et al.* to determine exchange integral $N_0\beta$ for Mn^{2+}, and we determine exchange integral $N_0\beta$ for Mn^{3+}. Moreover, to our best knowledge there is no determination of $N_0\beta$ in $Ga_{1-x}Fe_xN$, based on x-ray spectroscopy. From a theoretical point of view, the problem of the charge is not so important. Blinowski and Kacman[129] calculated $N_0\beta$ for the 3+ configuration of Mn, Fe, and Co in GaN. Their results are given in Table 6.4. They assumed reasonable positions of d-levels (2 eV for the distances of donor levels to the top of the GaN valence band), which appeared to be similar to determined further by x-ray spectroscopy. As a results, Blinowski and Kacman[129] derived values of $N_0\beta$ for the

3+ configuration not very different from further results of x-ray spectroscopy for the 2+ configuration.

Host	Mn^{3+}	Fe^{3+}	Co^{3+}	Reference
GaN	-1.5	-2.8	-3.1	Blinowski and Kacman, Ref. 129

Table 6.4: Exchange integrals $N_0\beta$ calculated for the 3+ configuration of magnetic ions in GaN. Values are given in eV.

It is interesting to note, that in the theoretical study based on Schrieffer-Wolf theory and reported in Ref. 129, $N_0\beta$ has been found to be negative even for the d^4 electronic configuration of Mn^{3+} in GaN. This result might be surprising in the context of positive $N_0\beta$ for Cr^{2+} in II-VI DMS.

To summarize the study based on Schrieffer-Wolf theory, large negative $N_0\beta$ is expected for Mn, Fe, and Co based wide gap DMS, independently on the charge state 2+ or 3+. It is in contradiction with $N_0\beta$ determined by us from giant Zeeman splitting of excitons. The magnetooptically determined $N_0\beta$ appears to be small and positive.

6.2.3 p-d exchange integrals : comparison

d^5 configuration

Fig. 6.3 presents the comparison values of $N_0\beta$ for d^5 configuration. There are magnetooptical results and results based on Schrieffer-Wolf theory, using parameters derived theoretically and determined from x-ray spectroscopy. Dashed line plots the material trend related to constant β. Mn^{2+} in ZnO and Fe^{3+} in GaN do not follow this trend.

d^4, d^5, d^6, and d^7 configurations

Fig. 6.4 shows the comparison values of $N_0\beta$ for d^7 and d^4 configuration. For d^7 configuration $N_0\beta$ is negative, except for one of our estimations in ZnO. For d^4 configuration magnetooptically detremined $N_0\beta$ is always positive, however $N_0\beta$ calculated using Schrieffer-Wolf theory can by positive or negative, depending on material parameters (see e.g. Table I of Ref 156).

Fig. 6.5 shows the comparison of all values of $N_0\beta$, which has been discussed in this chapter. There are magnetooptical results and results based on Schrieffer-Wolf theory, with parameters derived theoretically and determined from x-ray spectroscopy.

There are three separate groups of data presented in Fig. 6.5 : (i) negative values of $N_0\beta$ for classical Mn, Fe, and Co based II-VI and III-V DMS ; (ii) positive values of $N_0\beta$ for Cr and (iii) positive and small negative values of $N_0\beta$ determined in this work.

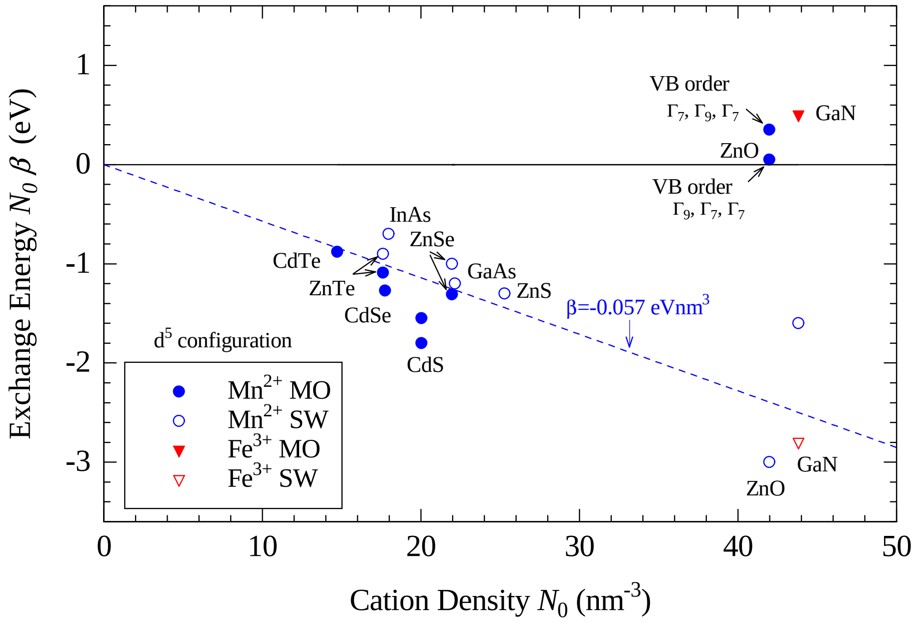

Figure 6.3: Exchange energy $N_0\beta$ for magnetic ions with d^5 configuration : Mn^{2+} and Fe^{3+}, versus cation density N_0. Full symbols - magnetooptical determination (MO). Empty symbols - determination based on Schrieffer-Wolf theory, Eq. (6.1) or on analogical calculations, with parameters determined from theory or x-ray spectroscopy (SW). Corresponding values of $N_0\beta$ are given in Tables 6.1, 6.2, 6.3, and 6.4. Cation density for each semiconductor is calculated using lattice constant a_0 from Ref. 11 ($N_0 = 4/a_0^3$).

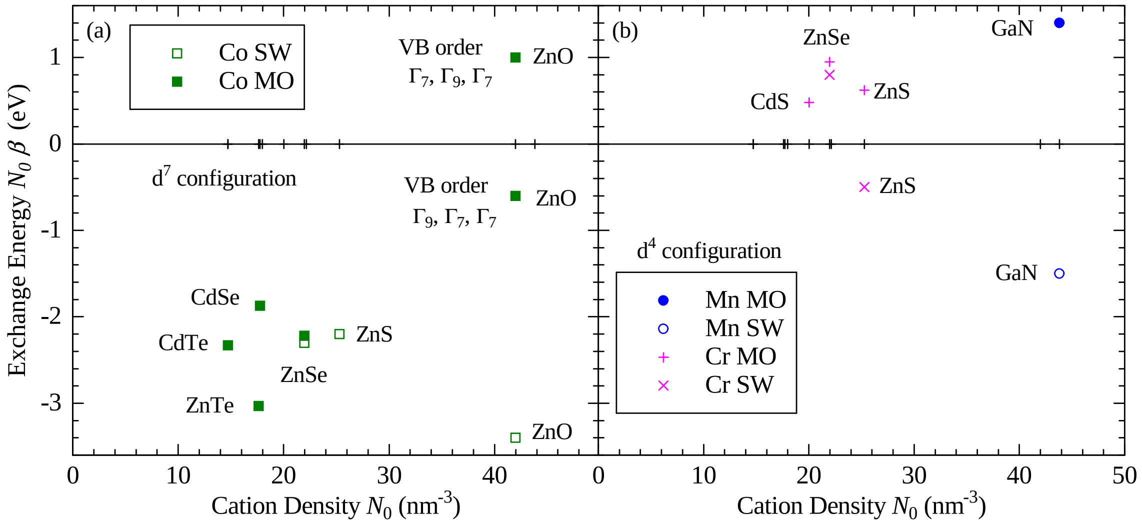

Figure 6.4: Exchange energy $N_0\beta$ for magnetic ions with d^7 (a) and d^4 (b) configuration, versus cation density N_0. Full symbols - magnetooptical determination (MO). Empty symbols - determination based on Schrieffer-Wolf theory, Eq. (6.1) or on analogical calculations, with parameters determined from theory or x-ray spectroscopy (SW). Corresponding values of $N_0\beta$ are given in Tables 6.1, 6.2, 6.3, and 6.4.

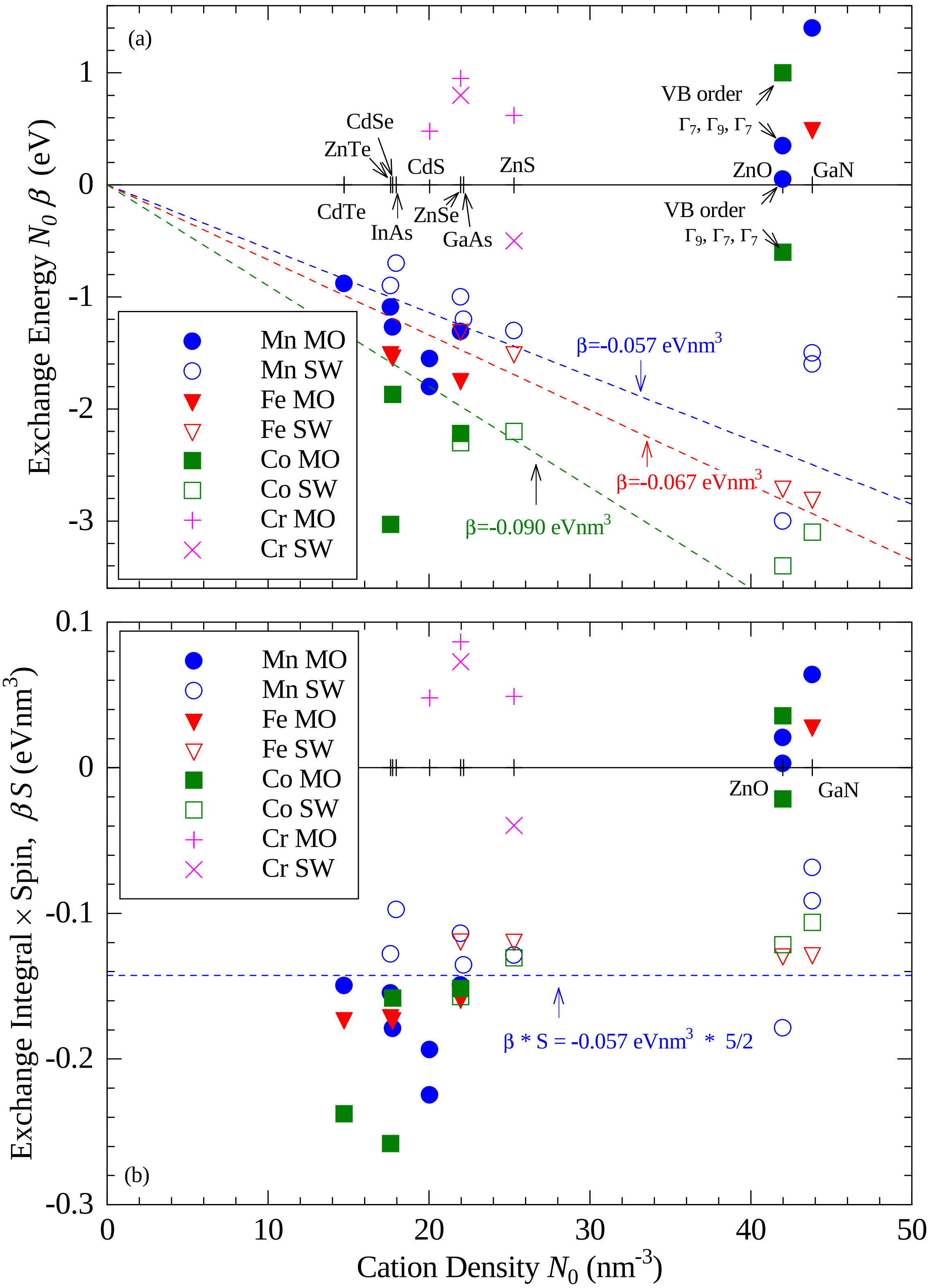

Figure 6.5: Exchange Energy $N_0\beta$ vs cation density N_0. Full symbols - magnetooptical determination (MO). Empty symbols - determination based on Eq. (6.1) or on analogical calculations, with parameters determined from theory or x-ray spectroscopy (SW). Corresponding values of $N_0\beta$ are given in Tables 6.1, 6.2, 6.3 and 6.4. Cation density for each semiconductor is calculated using lattice constant a_0 from Ref. 11 ($N_0 = 4/a_0^3$).

In the first, classical group, we observe two trends : a first trend is an increase of $N_0|\beta|$ when the spin of magnetic ions decreases, so $N_0|\beta|$ is the smallest for Mn^{2+} ($S = 5/2$), larger for Fe^{2+} ($S = 2$) and the largest for Co^{2+} ($S = 3/2$). Consequently, the spin splitting which depends on $N_0|\beta| \cdot S$ remains almost constant at saturated magnetization. A second trend is an increase of $N_0|\beta|$ with N_0, which simply means that β remains constant. It is shown in Fig. 6.5 by a dashed lines. Both trends can be approximately describe as $\beta \cdot S \approx const.$ Theoretical and x-ray spectroscopy results on ZnO and GaN based DMS continue this trends. Without any doubts magnetooptical results on ZnO and GaN DMS do not continue the above trends.

Failure of the virtual crystal approximation for wide gap DMS

We have shown, that our new results cannot be explained using previous models. Now, we will try to explain what is the difference between *p-d* coupling observed and derived from magnetooptics and x-ray spectroscopy. The results of x-ray spectroscopy, which were presented here, allow determination of the exchange energy. But they do not give the spin splitting of the bands. They do not give any direct information about behavior of carriers. Magnetooptical measurements of excitons allow us to observe the behavior of free carriers, and spin splitting of bands, but they do not give directly information about the exchange energy. Therefore the discrepancy between $N_0\beta$ determined from x-ray spectroscopy and from magnetooptics might means that the effect the *p-d* exchange interaction on the bands is different in wide gap DMS in comparison to classical DMS, where x-ray spectroscopy agrees with magnetooptics. An explanation of this new effect has been recently proposed by Dietl.[55]

Dietl remarked in Refs 55 and 36 that for an appropriately strong transition-metal potential, like the one expected for oxides and nitrides, the transition metal ion can bind a hole. This trend was already suggested by the experimental evidence of strong deviations from VCA in $Cd_{1-x}Mn_xS$[33] and by the analysis of *ab-initio* calculations.[57] A summation of infinite series of relevant self-energy diagrams demonstrates that in such a situation, the spin splitting of extended states involved in the optical transitions remains proportional to magnetization of the localized spins (see Fig. 6.6a), but the apparent exchange energy becomes significantly renormalized.[55] In fact, for the expected coupling strength, it is predicted that $-1 < \beta^{(\mathrm{app})}/\beta < 0$, as it is shown in Fig. 6.6(b). It means that the giant Zeeman splitting in wide gap DMS is governed by $\beta^{(\mathrm{app})}$, not by β.

This is exactly, what we observe experimentally in $Ga_{1-x}Fe_xN$ and $Ga_{1-x}Mn_xN$. Moreover, it can also explain our results related to $Zn_{1-x}Mn_xO$ and $Zn_{1-x}Co_xO$ (if we assume a reversed valence band ordering). This theory suggests also different behavior of free and bound excitons. This difference was observed in PL and reflectivity of $Zn_{1-x}Mn_xO$ (see Sec. 5.3.3).

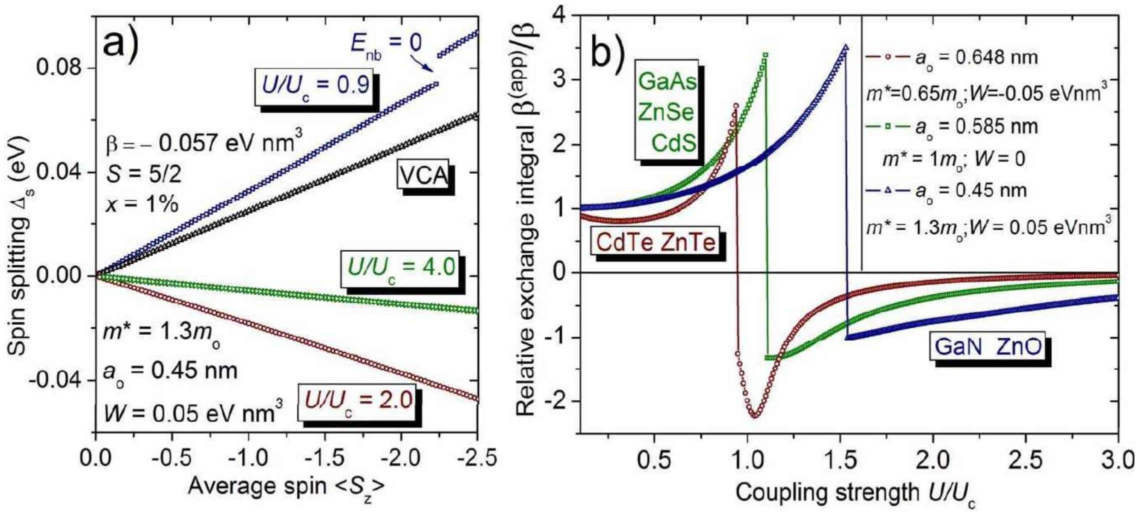

Figure 6.6: After T. Dietl, Ref. 55. Dependence of the band-edge spin splitting on the spin polarization, $\Delta_s(\langle\text{-}S_z\rangle)$ for three values of the coupling strength in comparison to the values expected within VCA and MFA, $\Delta_s^{VCA}(\langle\text{-}S_z\rangle)$ (a). Normalized apparent *p-d* exchange integral defined as $\Delta_s(\text{-}2.5)/\Delta_s^{VCA}(\text{-}2.5)$ for various combinations of the materials parameters (b).

In order to understand what happens beyond virtual approximation, a fruitful comparison can be made with the modification of the conduction band of GaAs induced by a slight doping with nitrogen.[161,162] When a hydrostatic pressure is applied, the nitrogen isoelectronic centers create localized states, which are observed in photoluminescence, but also extended states (the so-called E_+ states) to which the oscillator strength is transferred so that they are observed in reflectivity ; moreover, these optically active states exhibit an anticrossing with the localized states, and the strength of the anticrossing increases with the nitrogen density. As a result, the transition to these E_+ states exhibits a shift to *high energy* when the density of *low energy states* increases, as it is shown in Fig. 6.7. In a DMS with a large value of $N_0|\beta|$, only the transition metal impurities with the right spin orientation (antiparallel to the hole spin) are expected to form a localizing center[33,55] : hence the giant Zeeman shift in wide gap DMS can be understood as resulting from a similar anticrossing but in this case the density of relevant localized centers is additionally controlled by the field-induced orientation of the localized spins.

6.3 Accuracy of the model of excitonic giant Zeeman effect in wide gap DMS

The model presented in Chapter 4 and the analysis of the magnetooptical study of excitons presented in Chapter 5 are based on two important assumptions : (i) we can define constants ($N_0\alpha$ and $N_0\beta$), which describe proportionality of the giant Zeeman splitting to the magnetization, (ii) optical transitions observed in ZnO and

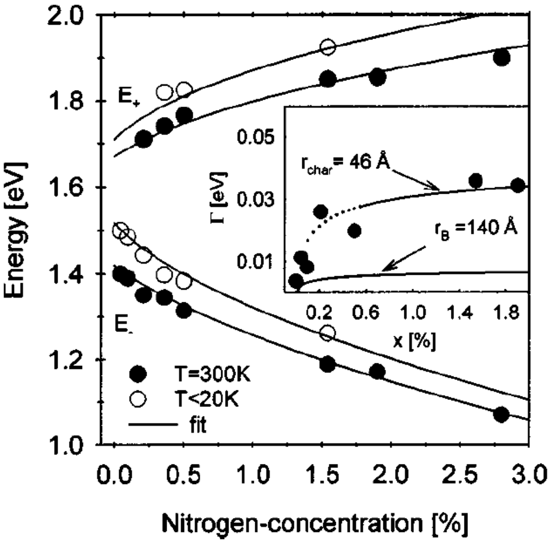

Figure 6.7: After Klar *et al.*, Ref. 162. The E_- and E_+ data obtained by fitting of the photomodulated reflectance spectra. The solid lines are a fit to a *kp* model. Inset : Comparison of the concentration dependence of the FWHM linewidth at 300 K with a statistical model.

GaN based DMSs have the same nature as optical transitions of ZnO and GaN (only Zeeman effect is enhanced). However, in the strong coupling regime (Sec. 6.2.3), these assumptions are not evident any more.

Proportionality of the giant Zeeman splitting to the magnetization

Works of Gubarew[31] and Nawrocki *et al.*[32] showed significant deviations from the proportionality of the giant Zeeman splitting at saturation to the Mn concentration in $\mathrm{Cd}_{1-x}\mathrm{Mn}_x\mathrm{S}$. Proportionality is expected in model based on virtual crystal approximation. Thus the observation gives an evidence that this approximation is not valid (see also Ref. 33) This indicates, that magnetooptical effects in ZnO and GaN based DMS might also be nonlinear as a function of the magnetization. Despite this, we systematically observe (Chapter 5) a linear increase of the giant Zeeman splitting at saturation when we increase concentration of magnetic ions. Also the temperature and magnetic field dependence of the giant Zeeman splitting can be well explained assuming that it is proportional to the magnetization. Therefore, we show that it is reasonable to parameterize the observed proportionality using effective parameters similar to classical exchange integrals $N_0\alpha$ and $N_0\beta$. Our experimental results are supported by works of Śliwa and Dietl,[127] and Dietl,[55] who find that *s*,*p*-*d* exchange interactions in strong coupling regime results in splitting of bands, which is approximately proportional to the magnetization. The nature of this splitting is different than in previously studied DMS, but it can be described using effective hamiltonian similar to (4.2) and (4.3). As a result a new effective hamiltonian describing the giant Zeeman effect in wide gap DMS can be given by[55,127]

$$H_{s-d}^{(\mathrm{app})} = -N_0\alpha^{(\mathrm{app})} x_{eff} \langle \vec{\mathbf{S}} \rangle \cdot \vec{s}_e, \tag{6.2}$$

for the conduction band electron, and

$$H_{p-d}^{(\mathrm{app})} = -N_0\beta^{(\mathrm{app})} x_{eff} \langle \vec{\mathbf{S}} \rangle \cdot \vec{s}_h, \tag{6.3}$$

for the valence band hole, where x_{eff} denotes the free magnetic ion content, $N_0\alpha^{(\mathrm{app})}$ the apparent exchange constant for the conduction band, $N_0\beta x^{(\mathrm{app})}$ the apparent exchange constant for the valence band, $\langle\vec{\mathbf{S}}\rangle$ the mean spin of the free magnetic ions and $\vec{s}_e$ and $\vec{s}_h$ are the spin of the electron and hole, respectively.

One should be very careful using effective hamiltonians (6.2) and (6.3), because the limit of this approach is not yet defined. It is tested only for very diluted samples. Further optical an theoretical study is still needed.

Nature of near band gap optical transitions in wide gap DMS

A strong coupling between magnetic ions and holes in wide gap DMSs significantly affects valence band edge. As a result, we cannot be sure if exciton and polariton models can be still used to describe near band gap optical effects. When density of states and effective mass change due to *s*,*p*-*d* exchange interactions,[55] we expect that also the interaction between electron and hole within exciton is affected. Moreover, effective mass approximation it not correct for description of potential with large gradient. Now, we will analyze consequences of these problems for the description of giant Zeeman effect observed experimentally in wide gap DMS.

Reflectivity is mainly sensitive on optical transitions with a large oscillator strength. Near the energy gap of semiconductor, band-to-band absorption is very strong, therefore only a high density of localized states can significantly affects optical spectra. Hence, in the limit of low concentrations of magnetic ions, we observe only transitions between states with a high density (transitions between delocalized states). Experimentally, the transitions observed in diluted ZnO and GaN based DMSs are very similar to that observed in pure ZnO and GaN. We observed typical excitonic effects such as, (i) series of excited states (see $\mathrm{Zn}_{1-x}\mathrm{Mn}_x\mathrm{O}$, sec. 5.3), (ii) classical Zeeman effect (see exciton C in $\mathrm{Ga}_{1-x}\mathrm{Fe}_x\mathrm{N}$, sec. 5.5), (iii) effect of electron-hole exchange interaction (see $\mathrm{Zn}_{1-x}\mathrm{Co}_x\mathrm{O}$ and $\mathrm{Zn}_{1-x}\mathrm{Mn}_x\mathrm{O}$, sections 5.2 and 5.3). Moreover, reflectivity spectra near energy gap of ZnO and GaN based DMS can be well described by the polariton model developed for the description of pure ZnO and GaN. Basing on this results we are convinced, that in the very diluted materials, we observe excitonic transitions.

Semenov *et al.*[103] have shown, that magnetooptically determined band parameters (Δ_1, Δ_2, and Δ_3) of $\mathrm{Cd}_{1-x}\mathrm{Mn}_x\mathrm{S}$ systematically evolve with Mn concentration. We expect similar effects in wide gap DMS. Experimentally, it is not clear, because of our limited precision. However, samples with higher concentration of magnetic ions ($x = 2.6\%$ in $\mathrm{Zn}_{1-x}\mathrm{Mn}_x\mathrm{O}$, sec 5.3.2) cannot be so well described as diluted $\mathrm{Zn}_{1-x}\mathrm{Mn}_x\mathrm{O}$ or $\mathrm{Zn}_{1-x}\mathrm{Co}_x\mathrm{O}$ samples. It means, that studying properties of ZnO by doping it with magnetic ions, can be risky, and parameters determined using this technique should be used with caution.

7

Conclusions

This work is devoted to the magnetooptical study of the exchange interactions between magnetic ions and delocalized carriers in a new group of materials : wide gap diluted magnetic semiconductors, such as ZnO and GaN doped with Mn, Fe, and Co.

Our samples are epitaxial layers grown on sapphire substrates using epitaxial methods, such as MBE and MOVPE. Several characterization techniques were crucial for the optimization of the crystal quality of our samples and for the determination of the magnetic ion content. We adapted our standard optical setups for polarization resolved, wide spectral range (IR-VIS-UV) magneto-spectroscopy including reflectivity, transmission and photoluminescence measurements.

Infrared spectroscopy of intra-ionic absorption and photoluminescence was important for the characterization of the magnetic ions introduced into our samples. The study of the intensity of characteristic absorption lines allowed us to check the concentration of magnetic ions with a particular charge state : Co^{2+} and Mn^{3+}. Magneto-absorption and magneto-photoluminescence allowed us to determine parameters governing the magnetic properties of Co^{2+} and to verify them in a direct way, by the observation of the occupancy of various spin sublevels. The magnetic properties of Co^{2+} and Mn^{3+} in wide gap DMS are very different from the properties of Mn in classical DMS, where the magnetization is given by a Brillouin function. We summarized the results from the literature and ours, on the ground state of various magnetic ions in wurtzite semiconductors, and we discussed the impact of the anisotropy (zero field splitting) on the magnetic properties. Such a good understanding of the magnetic behavior of our samples was crucial for the interpretation of results obtained by exciton spectroscopy.

We presented the classical description of wurtzite DMS, and we argued that it cannot be directly used for the interpretation of the giant Zeeman splitting in wide gap DMS. Instead of the previous model based on intra-band transitions, we developed a description based on excitons including electron-hole exchange. We improved also the model describing near band gap reflectivity spectra. Continuing the idea of Stępniewski *et al.*,[113] we combined the polariton model developed by Lagois[111] with the model of dielectric function developed by Tanguy.[115] As a result, we obtained a realistic, experimentally confirmed, analytic description of the reflectivity spectra in a wide range around the well resolved exciton lines.

Qualitative observations of the effect of *s*,*p*-*d* exchange interactions in wide gap DMS have been realized by several experimental groups before our study, but it was not enough quantitative to demonstrate a significant difference between the valence band of classical DMS and wide gap DMS. Our magnetooptical spectroscopy of excitons brings quantitative results : values of exchange integrals, which appear to be very different from values expected from theory or from the analysis of x-ray spectroscopy. At this moment, the only reasonable explication of our results is the interpretation proposed by T. Dietl, that wide gap DMS are in a strong coupling regime of the *s*,*p*-*d* exchange interactions, so that the direct influence of magnetic ions is the formation of bound states near the valence band edge. Then, these bound states are coupled to delocalized states, and induce a weak splitting very similar to the giant Zeeman effect observed in classical DMS. However the nature of this splitting is very different. Although it is not proportional to the *p*-*d* exchange integral β, it can be describe by another, phenomenological quantity, which can be labeled $\beta^{(\mathrm{app})}$ and which follows other material trends when compared to β.

We expect that this new effect of the *p*-*d* exchange interaction on the valence band, induces many new magnetic and magnetooptical phenomena, which were not included in our model. In this context, it is interesting to carefully check the points where our interpretation of experimental data fails in order to determine subjects for a future study :

- The most promising one seems to be the exploration of the hypothetical bound states which probably could be observed by photoluminescence, near band-gap absorption or MCD.
- Interesting nonlinearities related to the creation of an impurity band, could be obtained from reflectivity measurements of samples with a high concentration of magnetic ions.
- At this moment, the reflectivity spectra are well reproduced within the exciton-polariton model, but a complete model of the exciton formed from the perturbed valence band states has to be build and checked experimentally. Further increase of the optical quality of the layers can open wide gap DMS on new experimental techniques such as time resolved spectroscopy.
- A natural consequence is to use wide band gap DMS in heterostructures : quantum wells, wires and dots (actually, this is in progress in our labs).
- If we think about carrier mediated ferromagnetism, we are still waiting for techniques of doping with a high concentration of holes, which could make breakthrough in the domain. If this is not possible, a study of the coupling between secondary ferromagnetic phases and band carriers, could be interesting from the point of view of potential applications.

Although achievement of carrier mediated ferromagnetism in wide gap DMS appears to be difficult task, we are convinced that these materials are worth of further magnetooptical and theoretical study.

List of Figures

List of Tables

List of Samples

Label	Material	x	Growth	Growers	Figures
♯Z176	ZnO	0%	MBE	CRHEA	Figs. 5.1, 5.2, 5.3
♯Z158	$Zn_{1-x}Co_xO$	0.1%	MBE	CRHEA	Fig. 5.2
♯Z159	$Zn_{1-x}Co_xO$	0.4%	MBE	CRHEA	Figs. 5.2, 5.3, 5.5, 5.6
♯Z227	$Zn_{1-x}Co_xO$	0.5%	MBE	CRHEA	Fig. 5.2
♯Z219c	$Zn_{1-x}Co_xO$	2%	MBE	CRHEA	Figs. 3.1, 3.3, 5.2
♯Z217	$Zn_{1-x}Co_xO$	4.5%	MBE	CRHEA	Fig. 3.4
♯Z440	$Zn_{1-x}Mn_xO$	0.14%	MBE	CRHEA	Figs. 5.9, 5.16
♯Z435	$Zn_{1-x}Mn_xO$	0.6%	MBE	CRHEA	Figs. 5.9, 5.16, 5.17
♯Z441	$Zn_{1-x}Mn_xO$	1.4%	MBE	CRHEA	Fig. 5.9
♯Z434	$Zn_{1-x}Mn_xO$	2.6%	MBE	CRHEA	Figs. 5.9, 5.11, 5.12, 5.13
♯160606-2	$Zn_{1-x}Mn_xO$	1.1%	MOCVD	GEMC	Figs. 5.9, 5.15
♯1207	$Zn_{1-x}Mn_xO$	2.5%	MOCVD	GEMC	Figs. 5.18, 5.19
♯E787	$Ga_{1-x}Mn_xN$	0.01%	MBE	Institut Néel	Figs. 5.21
♯E766	$Ga_{1-x}Mn_xN$	0.5%	MBE	Institut Néel	Figs. 5.21, 5.22, 5.23, 5.25
♯E364c	$Ga_{1-x}Mn_xN$	1.2%	MBE	Institut Néel	Fig. 5.24
♯G0117	$Ga_{1-x}Mn_xN$		MOVPE	U. Göttingen	Fig. 3.7
♯590	GaN	0%	MOVPE	JKU	Figs. 5.27, 5.28
♯588	$Ga_{1-x}Fe_xN$	0.11%	MOVPE	JKU	Figs. 2.3, 5.30
♯647	$Ga_{1-x}Fe_xN$	0.15%	MOVPE	JKU	Figs. 2.3, 5.29, 5.30
♯589	$Ga_{1-x}Fe_xN$	0.21%	MOVPE	JKU	Figs. 2.3, 5.31, 5.32

Table 1: List of samples, which were important for this work.
CRHEA : Christiane Deparis and Christian Morhain from Centre de Recherches sur l'Hétéroépitaxie et ses Applications in Valbonne, France
GEMC : Ekaterina Chikoidze and Yves Dumont from Groupe d'Etude de la Matière Condensée, Meudon, Fance
U. Göttingen : Jan Zenneck from Georg-August Universität Göttingen, Germany
Institut Néel : Eirini Sarigiannidou and Henri Mariette from Institut Néel, équipe CNRS-CEA-UJF "Nanophysique et semiconducteurs", Grenoble, France
JKU : Andrea Navarro-Quezada, Matthias Wegsheider, and Alberta Bonnani from Institute for Semiconductor and Solid State Physics, Johannes Kepler University, Linz, Austria.

Bibliography

[1] H. Ohno, H. Munekata, T. Penney, S. von Molnár, and L. L. Chang, *Magnetotransport properties of p-type (In,Mn)As diluted magnetic III-V semiconductors*, Phys. Rev. Lett. **68**, 2664 (1992).

[2] H. Ohno, A. Shen, F. Matsukura, A. Oiwa, A. Endo, S. Katsumoto, and Y. Iye, *(Ga,Mn)As : A new diluted magnetic semiconductor based on GaAs*, Appl. Phys. Lett. **69**, 363 (1996).

[3] D. Ferrand, J. Cibert, A. Wasiela, C. Bourgognon, S. Tatarenko, G. Fishman, T. Andrearczyk, J. Jaroszyński, S. Koleśnik, T. Dietl, B. Barbara, and D. Dufeu, *Carrier-induced ferromagnetism in* $p - Zn_{1-x}Mn_xTe$, Phys. Rev. B **63**, 085201 (2001).

[4] A. Haury, A. Wasiela, A. Arnoult, J. Cibert, S. Tatarenko, T. Dietl, and Y. Merle d'Aubigné, *Observation of a Ferromagnetic Transition Induced by Two-Dimensional Hole Gas in Modulation-Doped CdMnTe Quantum Wells*, Phys. Rev. Lett. **79**, 511 (1997).

[5] H. Ohno, D. Chiba, F. Matsukura, T. Omiya, E. Abe, T. Dietl, Y. Ohno, and K. Ohtani, *Electric-Field Control of Ferromagnetism*, Nature **408**, 944 (2000).

[6] H. Boukari, P. Kossacki, M. Bertolini, D. Ferrand, J. Cibert, S. Tatarenko, A. Wasiela, J. A. Gaj, and T. Dietl, *Light and Electric Field Control of Ferromagnetism in Magnetic Quantum Structures*, Phys. Rev. Lett. **88**, 207204 (2002).

[7] P. Kossacki, W. Pacuski, W. Maslana, J. A. Gaj, M. Bertolini, D. Ferrand, S. Tatarenko, and J. Cibert, *Spin Engineering of Carrier-Induced Magnetic Ordering in (Cd,Mn)Te Quantum Wells*, Physica E **21**, 943 (2004).

[8] M. Sawicki, F. Matsukura, A. Idziaszek, T. Dietl, G. M. Schott, C. Ruester, C. Gould, G. Karczewski, G. Schmidt, and L. W. Molenkamp, *Temperature dependent magnetic anisotropy in (Ga,Mn)As layers*, Phys. Rev. B **70**, 245325 (2004).

[9] T. Dietl, H. Ohno, F. Matsukura, J. Cibert, and D. Ferrand, *Zener model description of ferromanetism in zinc-blende magnetic semiconductors*, Science **287**, 1019 (2000).

[10] K. Sato and H. Katayama-Yoshida, *Material Design for Transparent Ferromagnets with ZnO-Based Magnetic Semiconductors*, Jpn. J. Appl. Phys., Part 2, **39**, L555 (2000).

[11] T. Dietl, H. Ohno, and F. Matsukura, *Hole-mediated ferromagnetism in tetrahedrally coordinated semiconductors*, Phys. Rev. B **63**, 195205 (2001).

[12] J. Blinowski, P. Kacman, and T. Dietl, *Kinetic exchange vs. room temperature ferromagnetism in diluted magnetic semiconductors*, Mat. Res. Soc. Symp. Proc. 690 ; arXiv : cond-mat/0201012 (2002).

[13] N. A. Spaldin, *Search for ferromagnetism in transition-metal-doped piezoelectric ZnO*, Phys. Rev. B **69**, 125201 (2004).

[14] K. Ueda, H. Tabata, and T. Kawai, *Magnetic and electric properties of transition-metal-doped ZnO films*, Appl. Phys. Lett. **79**, 988 (2001).

[15] M. L. Reed, N. A. El-Masry, H. H. Stadelmaier, M. K. Ritums, M. J. Reed, C. A. Parker, J. C. Roberts, and S. M. Bedair, *Room temperature ferromagnetic properties of (Ga, Mn)N*, Appl. Phys. Lett. **79**, 3473 (2001).

[16] S. Sonoda, S. Shimizu, T. Sasaki, Y. Yamamoto, and H. Hori, *Molecular beam epitaxy of wurtzite (Ga,Mn)N films on sapphire (0 0 0 1) showing the ferromagnetic behaviour at room temperature*, Journal of Crystal Growth **237-239**, 1328 (2002).

[17] G. T. Thaler, M. E. Overberg, B. Gila, R. Frazier, C. R. Abernathy, S. J. Pearton, J. S. Lee, S. Y. Lee, Y. D. Park, Z. G. Khim, J. Kim, and F. Ren, *Magnetic properties of n-GaMnN thin films*, Appl. Phys. Lett. **80**, 3964 (2002).

[18] S.-W. Lim, D.-K. Hwang, and J.-M. Myoung, *Observation of optical properties related to room-temperature ferromagnetism in co-sputtered* $Zn_{1-x}Co_xO$ *thin films*, Solid State Commun. **125**, 231 (2003).

[19] K. Rode, A. Anane, R. Mattana, J.-P. Contour, O. Durand, and R. LeBourgeois, *Magnetic semiconductors based on cobalt substituted ZnO*, J. Appl. Phys. **93**, 7676 (2003).

[20] S. Ramachandran, A. Tiwari, and J. Narayan, $Zn_{0.9}Co_{0.1}O$*-based diluted magnetic semiconducting thin films*, Appl. Phys. Lett. **84**, 5255 (2004).

[21] A. C. Tuan, J. D. Bryan, A. B. Pakhomov, V. Shutthanandan, S. Thevuthasan, D. E. McCready, D. Gaspar, M. H. Engelhard, J. W. Rogers, Jr., K. Krishnan, D. R. Gamelin, and S. A. Chambers, *Epitaxial growth and properties of cobalt-doped ZnO on alpha-*Al_2O_3 *single-crystal substrates*, Phys. Rev. B **70**, 054424 (2004).

[22] K. R. Kittilstved, N. S. Norberg, and D. R. Gamelin, *Chemical Manipulation of High-*T_C *Ferromagnetism in ZnO Diluted Magnetic Semiconductors*, Phys. Rev. Lett. **94**, 147209 (2005).

[23] M. Venkatesan, C. B. Fitzgerald, J. G. Lunney, and J. M. D. Coey, *Anisotropic Ferromagnetism in Substituted Zinc Oxide*, Phys. Rev. Lett. **93**, 177206 (2004).

[24] K. Ando, H. Saito, V. Zayets, and M. C. Debnath, *Optical properties and functions of dilute magnetic semiconductors*, J. Phys. Cond. Matter. **16**, S5541 (2004).

[25] T. Dietl, *Self-organized growth controlled by charge states of magnetic impurities*, Nature Materials **5**, 673 (2006).

[26] T. Dietl, *Origin of ferromagnetic response in diluted magnetic semiconductors and oxides*, J. Phys. : Condens. Matter **19**, 165204 (2007).

[27] The editors of Science, *So Much More to Know*, Science **309**, 78 (2005).

[28] J. K. Furdyna, *Diluted magnetic semiconductors*, J. Appl. Phys. **64**, R29 (1988).

[29] A. H. Morrish, *The physical principles of magnetism* (John Wiley and Sons, Inc., New York, 1965).

[30] T. G. Dargam, R. B. Capaz, and B. Koiller, *Critical Analysis of the Virtual Crystal Approximation*, Brazilian Journal of Physics **27/A**, 299 (1997).

[31] S. I. Gubarev, Zh. Eksp. Teor. Fiz **80**, 1174 (1983).

[32] M. Nawrocki, J. P. Lascaray, D. Coquillat, and M. Demianiuk, *Ion-Carrier Exchange Interaction in CdMnS*, in Diluted Magnetic (Semimagnetic) Semiconductors, edited by S. von Molnar, R. Aggarwal and J. K. Furdyna, Mat. Res. Soc. Symp. Proc. **89**, 65 (1987).

[33] C. Benoit à la Guillaume, D. Scalbert, and T. Dietl, *Wigner-Seitz approach to spin splitting*, Phys. Rev. B **46**, 9853 (1992).

[34] W. Pacuski, D. Ferrand, J. Cibert, C. Deparis, J. A. Gaj, P. Kossacki, and C. Morhain, *Effect of the s,p-d exchange interaction on the excitons in* $Zn_{1-x}Co_xO$ *epilayers*, Phys. Rev. B **73**, 035214 (2006).

[35] W. Pacuski, D. Ferrand, J. Cibert, J. A. Gaj, A. Golnik, P. Kossacki, S. Marcet, E. Sarigiannidou, and H. Mariette, *Excitonic giant Zeeman effect in* $GaN{:}Mn^{3+}$, Phys. Rev. B **76**, 165304 (2007).

[36] W. Pacuski, P. Kossacki, D. Ferrand, A. Golnik, J. Cibert, M. Wegscheider, A. Navarro-Quezada, A. Bonanni, M. Kiecana, M. Sawicki, and T. Dietl, *Observation of Strong-Coupling Effects in a Diluted Magnetic Semiconductor* $Ga_{1-x}Fe_xN$, Phys. Rev. Lett. **100**, 037204 (2008).

[37] W. Pacuski, D. Ferrand, J. Cibert, C. Deparis, P. Kossacki, and C. Morhain, *Magneto-optical spectroscopy of (Zn,Co)O epilayers*, Phys. Status Solidi B **243**, 863 (2006).

[38] W. Pacuski, D. Ferrand, P. Kossacki, S. Marcet, J. Cibert, J. Gaj, and A. Golnik, *Excitonic Giant Zeeman Effect in Wide Gap Diluted Magnetic Semiconductors Based on ZnO and GaN*, Acta Phys. Pol. A **110**, 303 (2006).

[39] E. Przeździecka, E.Kamińska, M. Kiecana, M. Sawicki, Ł. Kłopotowski, W. Pacuski, and J. Kossut, *Magneto-optical properties of the diluted magnetic semiconductor p-type ZnMnO*, Solid State Commun. **139**, 541 (2006).

[40] S. Marcet, W. Pacuski, , E. Sarigiannidou, F. Wilhelm, D. Ferrand, S. Kuroda, R. M. Galera, E. Gheeraert, J. Cibert, A. Rogalev, H. Mariette, and P. Kossacki, *Intrinsic magnetism in wurtzite (Ga,Mn)N*, Phys. Status Solidi C **3**, 4062 (2006).

[41] K. Ando, H. Saito, Z. Jin, T. Fukumura, M. Kawasaki, Y. Matsumoto, and H. Koinuma, *Magneto-optical properties of ZnO-based diluted magnetic semiconductors*, J. Appl. Phys. **89**, 7284 (2001).

[42] K. Ando, H. Saito, Z. Jin, T. Fukumura, M. Kawasaki, Y. Matsumoto, and H. Koinuma, *Large magneto-optical effect in an oxide diluted magnetic semiconductor* $Zn_{1-x}Co_xO$, Appl. Phys. Lett. **78**, 2700 (2001).

[43] K. Ando, *Magneto-optical study of ZnO based diluted magnetic semiconductors*, 7th Symposium PASPS 2001 , condmat/0208010 (2002).

[44] D. A. Schwartz, N. S. Norberg, Q. P. Nguyen, J. M. Parker, and D. R. Gamelin, *Magnetic Quantum Dots : Synthesis, Spectroscopy, and Magnetism of* Co^{2+}*- and* Ni^{2+}*-Doped ZnO Nanocrystals*, J. Am. Chem. Soc. **125**, 13205 (2003).

[45] K. R. Kittilstved, J. Zhao, W. K. Liu, J. D. Bryan, D. A. Schwartz, and D. R. Gamelin, *Magnetic circular dichroism of ferromagnetic* Co^{2+}*-doped ZnO*, Appl. Phys. Lett. **89**, 062510 (2006).

[46] K. Ando, *Magneto-optical studies of s,p-d exchange interactions in GaN :Mn with room-temperature ferromagnetism*, Appl. Phys. Lett. **82**, 100 (2003).

[47] S. Marcet, D. Ferrand, D. Halley, S. Kuroda, H. Mariette, E. Gheeraert, F. J. Teran, M. L. Sadowski, R. M. Galera, and J. Cibert, *Magneto-optical spectroscopy of* $(Ga, Mn)N$ *epilayers*, Phys. Rev. B **74**, 125201 (2006).

[48] P. Koidl, *Optical absorption of* Co^{2+} *in ZnO*, Phys. Rev. B **15**, 2493 (1977).

[49] R. Pappalardo, D. L. Wood, and R. C. Linares Jr, *Optical Absorption Study of Co-Doped Oxide Systems. II*, J. Chem. Phys. **35**, 2041 (1961).

[50] R. S. Anderson, *Lattice-Vibration Effects in the Spectra of ZnO:Ni and ZnO:Co*, Phys. Rev. **164**, 398 (1967).

[51] H.-J. Schulz and M. Thiede, *Optical spectroscopy of* $3d^7$ *and* $3d^8$ *impurity configurations in a wide-gap semiconductor (ZnO:Co,Ni,Cu)*, Phys. Rev. B **35**, 18 (1987).

[52] A. Wolos, A. Wysmolek, M. Kaminska, A. Twardowski, M. Bockowski, I. Grzegory, S. Porowski, and M. Potemski, *Neutral Mn acceptor in bulk GaN in high magnetic fields*, Phys. Rev. B **70**, 245202 (2004).

[53] E. Malguth, A. Hoffmann, W. Gehlhoff, O. Gelhausen, M. R. Phillips, and X. Xu, *Structural and electronic properties of* Fe^{3+} *and* Fe^{2+} *centers in GaN from optical and EPR experiments*, Phys. Rev. B **74**, 165202 (2006).

[54] E. Malguth, A. Hoffmann, and X. Xu, *Internal* $^5E- >^5 T_2$ *transition of* Fe^{2+} *in GaN*, Phys. Rev. B **74**, 165201 (2006).

[55] T. Dietl, *Hole states in wide band-gap diluted magnetic semiconductors and oxides*, Phys.Rev. B **77**, 085208 (2008).

[56] M. Abolfath, T. Jungwirth, J. Brum, and A. H. MacDonald, *Theory of magnetic anisotropy in* $III_{1-x}Mn_xV$ *ferromagnets*, Phys. Rev. B **63**, 054418 (2001).

[57] R. Bouzerar, G. Bouzerar, and T. Ziman, *Non-perturbative* $V - J_{pd}$ *model and ferromagnetism in dilute magnets*, Europhysics Letters (EPL) **78**, 67003 (5pp) (2007).

[58] F. Popescu, C. Şen, E. Dagotto, and A. Moreo, *The Crossover from Impurity to Valence Band in Diluted Magnetic Semiconductors : The Role of the Coulomb Attraction by Acceptor*, arXiv : cond-mat/0705.0309 (2007).

[59] P. Y. Yu and M. Cardona, *Fundamentals of Semiconductors - Physics and Materials Properties* (Springer, 1995).

[60] E. Chikoidze, Y. Dumont, H. von Bardeleben, W. Pacuski, and O. Gorochova, *$Zn_{1-x}Mn_xO$: A typical member of the II-VI :Mn DMS family*, Superlattices and Microstructures **42**, 176 (2007).

[61] E. Sarigiannidou, F. Wilhelm, E. Monroy, R. M. Galera, E. Bellet-Amalric, A. Rogalev, J. Goulon, J. Cibert, and H. Mariette, *Intrinsic ferromagnetism in wurtzite (Ga,Mn)N semiconductor*, Phys. Rev. B **74**, 041306 (2006).

[62] A. Bonanni, M. Kiecana, C. Simbrunner, T. Li, M. Sawicki, M. Wegscheider, M. Quast, H. Przybylińska, A. Navarro-Quezada, R. Jakieła, A. Wolos, W. Jantsch, and T. Dietl, *Paramagnetic GaN :Fe and ferromagnetic (Ga,Fe)N : The relationship between structural, electronic, and magnetic properties*, Phys. Rev. B **75**, 125210 (2007).

[63] J. Gaj, R. Planel, and G. Fishman, *Relation of Magnetooptical Properties of Free Excitons to Spin Alignment of Mn^{++} ions in $Cd_{1-x}Mn_xTe$*, Solid State Commun. **29**, 435 (1979).

[64] R. M. Macfarlane and J. C. Vial, *Saturation spectroscopy and fluorescence in ZnO:Co^{2+}*, Mater. Sci. Forum **10-12**, 845 (1986).

[65] R. Heitz, A. Hoffmann, and I. Broser, *Fe^{3+} center in ZnO*, Phys. Rev. B **45**, 8977 (1992).

[66] T. Hoshina, *Electron Spin Resonance of Co^{2+} in CdSe*, J. Phys. Soc. Jpn. **21**, 1608 (1966).

[67] A. Lewicki, A. I. Schindler, I. Miotkowski, B. C. Crooker, and J. K. Furdyna, *Specific heat of $Cd_{1-x}Co_xS$ and $Cd_{1-x}Co_xSe$ at low temperatures*, Phys. Rev. B **43**, 5713 (1991).

[68] F. Hamdani, J. P. Lascaray, D. Coquillat, A. K. Bhattacharjee, M. Nawrocki, and Z. Golacki, *Magnetoreflectance and magnetization of the Co-based wurtzite-structure diluted magnetic semiconductor $Cd_{1-x}Co_xSe$*, Phys. Rev. B **45**, 13298 (1992).

[69] C. Testelin, C. Rigaux, A. Mauger, A. Mycielski, and C. Julien, *Dynamic Jahn-Teller effect on the far-infrared spectrum of Fe^{2+} in $Cd_{1-x}Fe_xTe$ compounds*, Phys. Rev. B **46**, 2183 (1992).

[70] C. Testelin, C. Rigaux, A. Mauger, A. Mycielski, and M. Guillot, *Magnetism of Fe^{2+} ions in $Cd_{1-x}Fe_xTe$ compounds*, Phys. Rev. B **46**, 2193 (1992).

[71] Y. Shapira, S. Foner, D. H. Ridgley, K. Dwight, and A. Wold, *Technical saturation and magnetization steps in diluted magnetic semiconductors : Predictions and observations*, Phys. Rev. B **30**, 4021 (1984).

[72] R. M. Macfarlane, *Perturbation Methods in the Calculation of Zeeman Interactions and Magnetic Dipole Line Strengths for d^3 Trigonal-Crystal Spectra*, Phys. Rev. B **1**, 989 (1970).

[73] E. Chikoidze, H. J. V. Bardeleben, Y. Dumont, P. Galtier, and J. L. Cantin, *Magnetic interactions in $Zn_{1-x}Mn_xO$ studied by electron paramagnetic resonance spectroscopy*, J. Appl. Phys. **97**, 10D316 (2005).

[74] P. Sati, C. Deparis, C. Morhain, S. Schafer, and A. Stepanov, *Antiferromagnetic Interactions in Single Crystalline $Zn_{1-x}Co_xO$ Thin Films*, Phys. Rev. Lett. **98**, 137204 (2007).

[75] N. Jedrecy, H. J. V. Bardeleben, Y. Zheng, and J. L. Cantin, *Electron paramagnetic resonance study of $Zn_{1-x}Co_xO$: A predicted high-temperature ferromagnetic semiconductor*, Phys. Rev. B **69**, R041308 (2004).

[76] P. Sati, R. Hayn, R. Kuzian, S. Régnier, S. Schäfer, A. Stepanov, C. Morhain, C. Deparis, M. Laügt, M. Goiran, and Z. Golacki, *Magnetic Anisotropy of Co^{2+} as Signature of Intrinsic Ferromagnetism in $ZnO\!:\!Co$*, Phys. Rev. Lett. **96**, 017203 (2006).

[77] D. Ferrand, S. Marcet, W. Pacuski, E. Gheeraert, P. Kossacki, J. A. Gaj, J. Cibert, C. Deparis, H. Mariette, and C. Morhain, *Spin Carrier Exchange Interactions in (Ga,Mn)N and (Zn,Co)O Wide Band Gap Diluted Magnetic Semiconductor Epilayers*, J. Superconductivity **18**, 15 (2005).

[78] T. Mizokawa, T. Nambu, A. Fujimori, T. Fukumura, and M. Kawasaki, *Electronic structure of the oxide-diluted magnetic semiconductor $Zn_{1-x}Mn_xO$*, Phys. Rev. B **65**, 085209 (2002).

[79] Z.-W. Jin, Y.-Z. Yoo, T. Sekiguchi, T. Chikyow, H. Ofuchi, H. Fujioka, M. Oshima, and H. Koinuma, *Blue and ultraviolet cathodoluminescence from Mn-doped epitaxial ZnO thin films*, Appl. Phys. Lett. **83**, 39 (2003).

[80] N. Norberg, K. Kittilstved, J. Amonette, R. Kukkadapu, D. Schwartz, and D. Gamelin, *Synthesis of Colloidal Mn^{2+} :ZnO Quantum Dots and High-T_C Ferromagnetic Nanocrystalline Thin Films*, J. Am. Chem. Soc. **126**, 9387 (2004).

[81] N. Norberg, G. M. Dalpian, J. R. Chelikowsky, and D. Gamelin, *Pinned Magnetic Impurity Levels in Doped Quantum Dots*, arXiv : cond-mat/0608734 (2006).

[82] J. Zenneck, T. Niermann, D. Mai, M. Roever, M. Kocan, J. Malindretos, M. Seibt, A. Rizzi, N. Kaluza, and H. Hardtdegen, *Intra-atomic photoluminescence at 1.41 eV of substitutional Mn in GaMnN of high optical quality*, J. Appl. Phys. **101**, 063504 (2007).

[83] P. Sati and A. Stepanov, private communication .

[84] R. Heitz, P. Thurian, I. Loa, L. Eckey, A. Hoffmann, I. Broser, K. Pressel, B. K. Meyer, and E. N. Mokhov, *Zeeman spectroscopy of the Fe^{3+} center in GaN*, Appl. Phys. Lett. **67**, 2822 (1995).

[85] M. I. Darby, *Tables of the Brillouin function and of the related function for the spontaneous magnetization*, British Journal of Applied Physics **18**, 1415 (1967).

[86] A. Abragam and M. H. L. Pryce, *Theory of the Nuclear Hyperfine Structure of Paramagnetic Resonance Spectra in Crystals*, Proceedings of the Royal Society of London. Series A, Mathematical and Physical Sciences **205**, 135 (1951).

[87] X. Gratens, V. Bindilatti, J. N. F. Oliveira, Y. Shapira, S. Foner, Z. Golacki, and T. E. Haas, *Magnetization steps in $Zn_{1-x}Mn_xO$: Four largest exchange constants and single-ion anisotropy*, Phys. Rev. B **69**, 125209 (2004).

[88] J. A. Gaj, W. Grieshaber, C. Bodin-Deshayes, J. Cibert, G. Feuillet, Y. M. D'Aubigné, and A. Wasiela, *Magneto-optical study of interface mixing in the CdTe-(Cd,Mn)Te system*, Phys. Rev. B **50**, 5512 (1994).

[89] M. Julier, J. Campo, B. Gil, J. P. Lascaray, and S. Nakamura, *Determination of the spin-exchange interaction constant in wurtzite GaN*, Phys. Rev. B **57**, R6791 (1998).

[90] B. Gil and A. Alemu, *Optical Anisotropy of Excitons in Strained GaN Epilayers Grown Along the* $<10\bar{1}0>$ *Direction*, Phys. Rev. B **56**, 12446 (1997).

[91] W. R. L. Lambrecht, A. V. Rodina, S. Limpijumnong, B. Segall, and B. K. Meyer, *Valence-band ordering and magneto-optic exciton fine structure in ZnO*, Phys. Rev. B **65**, 075207 (2002).

[92] J. L. Birman, *Polarization of Fluorescence in CdS and ZnS Single Crystals*, Phys. Rev. Lett. **2**, 157 (1959).

[93] R. Stępniewski, M. Potemski, A. Wysmołek, K. Pakuła, J. M. Baranowski, J. Łusakowski, I. Grzegory, S. Porowski, G. Martinez, and P. Wyder, *Symmetry of excitons in GaN*, Phys. Rev. B **60**, 4438 (1999).

[94] B. Gil, *Comment on "Influence of biaxial strains on the vibrational and exciton energies in ZnO" [J. Appl. Phys. 96, 289 (2004)]*, J. Appl. Phys. **98**, 086114 (2005).

[95] D. W. Langer, R. N. Euwema, K. Era, and T. Koda, *Spin Exchange in Excitons, the Quasicubic Model and Deformation Potentials in II-VI Compounds*, Phys. Rev. B **2**, 4005 (1970).

[96] D. C. Reynolds, D. C. Look, B. Jogai, C. W. Litton, G. Cantwell, and W. C. Harsch, *Valence-band ordering in ZnO*, Phys. Rev. B **60**, 2340 (1999).

[97] B. Gil, A. Lusson, V. Sallet, S.-A. Said-Hassani, R. Triboulet, and P. Bigenwald, *Strain-Fields Effects and Reversal of the Nature of the Fundamental Valence Band of ZnO Epilayers*, Jpn. J. Appl. Phys. **40**, L 1089 (2001).

[98] B. Gil, *Oscillator strengths of A, B, and C excitons in ZnO films*, Phys. Rev. B **64**, 201310 (2001).

[99] T. Gruber, G. M. Prinz, C. Kirchner, R. Kling, F. Reuss, W. Limmer, and A. Waag, *Influences of biaxial strains on the vibrational and exciton energies in ZnO*, J. Appl. Phys. **96**, 289 (2004).

[100] D. G. Thomas, *The exciton spectrum of zinc oxide*, J. Phys. Chem. Solids **15**, 86 (1960).

[101] M. Arciszewska and M. Nawrocki, *Determination of the band structure parameters of* $Cd_{0.95}Mn_{0.05}Se$ *from magnetoabsorption measurements*, J. Phys. Chem. Solids **47**, 309 (1986).

[102] M. Herbich, W. Mac, A. Twardowski, K. Ando, Y. Shapira, and M. Demianiuk, *Magnetization and exciton spectroscopy of the diluted magnetic semiconductor* $Cd_{1-x}Cr_xS$, Phys. Rev. B **58**, 1912 (1998).

[103] Y. G. Semenov, V. G. Abramishvili, A. V. Komarov, and S. M. Ryabchenko, *Magneto-optical investigations of diluted* $Cd_{1-x}Mn_xS$ *magnetic semiconductors in the B-exciton region*, Phys. Rev. B **56**, 1868 (1997).

[104] B. Gil, O. Briot, and R.-L. Aulombard, *Valence-band physics and the optical properties of GaN epilayers grown onto sapphire with wurtzite symmetry*, Phys. Rev. B **52**, R17028 (1995).

[105] R. L. Aggarwal, S. N. Jasperson, J. Stankiewicz, Y. Shapira, S. Foner, B. Khazai, and A. Wold, *Magnetoreflectance at the band edge in* $Cd_{1-x}Mn_xSe$, Phys. Rev. B **28**, 6907 (1983).

[106] M. Nawrocki, F. Hamdani, J. P. Lascaray, Z. Golacki, and J. Deportes, *Ion-carrier electron exchange constants for CdCoSe semimagnetic semiconductor*, Solid State Commun. **77**, 111 (1991).

[107] A. Twardowski, K. Pakula, I. Perez, P. Wise, and J. E. Crow, *Magnetoreflectance and magnetization of the semimagnetic semiconductor* $Cd_{1-x}Fe_xSe$, Phys. Rev. B **42**, 7567 (1990).

[108] W. Y. Yu, A. Twardowski, L. P. Fu, A. Petrou, and B. T. Jonker, *Magnetoanisotropy in* $Zn_{1-x}Mn_xSe$ *strained epilayers*, Phys. Rev. B **51**, 9722 (1995).

[109] J. M. Luttinger, *Quantum Theory of Cyclotron Resonance in Semiconductors : General Theory*, Phys. Rev. **102**, 1030 (1956).

[110] J. Lagois, *Depth-dependent eigenenergies and damping of excitonic polaritons near a semiconductor surface*, Phys. Rev. B **23**, 5511 (1981).

[111] J. Lagois, *Dielectric theory of interacting excitonic resonances*, Phys. Rev. B **16**, 1699 (1977).

[112] J. J. Hopfield and D. G. Thomas, *Theoretical and Experimental Effects of Spatial Dispersion on the Optical Properties of Crystals*, Phys. Rev. **132**, 563 (1963).

[113] R. Stępniewski, K. P. Korona, A. Wysmołek, J. M. Baranowski, K. Pakuła, M. Potemski, G. Martinez, I. Grzegory, and S. Porowski, *Polariton effects in reflectance and emission spectra of homoepitaxial GaN*, Phys. Rev. B **56**, 15151 (1997).

[114] R. J. Elliot, *Intensity of optical absorption by excitons*, Phys. Rev. **108**, 1384 (1957).

[115] C. Tanguy, *Optical Dispersion by Wannier Excitons*, Phys. Rev. Lett. **75**, 4090 (1995).

[116] R. Le Toullec, N. Piccioli, and J. C. Chervin, *Optical properties of the band-edge exciton in GaSe crystals at 10 K*, Phys. Rev. B **22**, 6162 (1980).

[117] K. Kornitzer, T. Ebner, M. Grehl, K. Thonke, R. Sauer, C. Kirchner, V. Schwegler, M. Kamp, M. Leszczynski, I. Grzegory, and S. Porowski, *High-Resolution Photoluminescence and Reflectance Spectra of Homoepitaxial GaN Layers*, Phys. Stat. Sol. B **216**, 5 (1999).

[118] B. Sermage, S. Petiot, C. Tanguy, L. S. Dang, and R. André, $Cd_{0.88}Zn_{0.12}Te$ *group index measurements near the exciton energy at low temperature*, J. Appl. Phys. **83**, 7903 (1998).

[119] B. Segall, *Intrinsic Absorption "Edge" in II-VI Semiconducting Compounds with the Wurtzite Structure*, Phys. Rev. **163**, 769 (1967).

[120] K. Hümmer, *Interband Magnetoreflection of ZnO*, Phys. Status Solidi **56**, 249 (1973).

[121] G. Blattner, G. Kurtze, G. Schmieder, and C. Klingshirn, *Influence of magnetic fields up to 20 T on excitons and polaritons in CdS and ZnO*, Phys. Rev. B **25**, 7413 (1982).

[122] S. H. Liu, *Exchange Interaction between Conduction Electrons and Magnetic Shell Electrons in Rare-Earth Metals*, Phys. Rev. **121**, 451 (1961).

[123] J. Okabayashi, K. Ono, M. Mizuguchi, M. Oshima, S. S. Gupta, D. D. Sarma, T. Mizokawa, A. Fujimori, M. Yuri, C. T. Chen, T. Fukumura, M. Kawasaki, and H. Koinuma, *X-ray absorption spectroscopy of transition-metal doped diluted magnetic semiconductors* $Zn_{1-x}Mn_xO$, J. Appl. Phys. **95**, 3573 (2004).

[124] S. Lee, M. Dobrowolska, and J. K. Furdyna, *Effect of spin-dependent* Mn^{2+} *internal transitions in* $CdSe/Zn_{1-x}Mn_xSe$ *magnetic semiconductor quantum dot systems*, Phys. Rev. B **72**, 075320 (2005).

[125] J. Campo, M. Julier, D. Coquillat, J. P. Lascaray, D. Scalbert, and O. Briot, *Zeeman splittings of excitonic transitions at the* Γ *point in wurtzite GaN : A magnetoreflectance investigation*, Phys. Rev. B **56**, R7108 (1997).

[126] A. Wolos, M. Palczewska, Z. Wilamowski, M. Kaminska, A. Twardowski, M. Bockowski, I. Grzegory, and S. Porowski, $S-d$ *exchange interaction in GaN:Mn studied by electron paramagnetic resonance*, Appl. Phys. Lett. **83**, 5428 (2003).

[127] C. Sliwa and T. Dietl, *Apparent s-d exchange interaction in III-V diluted magnetic semiconductors*, arXiv : cond-mat/0707.3542 (2007).

[128] W. Mac, N. T. Khoi, A. Twardowski, J. A. Gaj, and M. Demianiuk, *Ferromagnetic p-d exchange in* $Zn_{1-x}Cr_xSe$ *diluted magnetic semiconductor*, Phys. Rev. Lett. **71**, 2327 (1993).

[129] J. Blinowski and P. Kacman, *On the Kinetic Exchange in* A^{III} B^{V} *Diluted Magnetic Semiconductors*, Acta Phys. Pol. A **100**, 343 (2001).

[130] A. K. Bhattacharjee, *Chromium-based diluted magnetic semiconductors*, Phys. Rev. B **49**, 13987 (1994).

[131] J. I. Hwang, Y. Ishida, M. Kobayashi, H. Hirata, K. Takubo, T. Mizokawa, A. Fujimori, J. Okamoto, K. Mamiya, Y. Saito, Y. Muramatsu, H. Ott, A. Tanaka, T. Kondo, and H. Munekata, *High-energy spectroscopic study of the III-V nitride-based diluted magnetic semiconductor* $Ga_{1-x}Mn_xN$, Phys. Rev. B **72**, 085216 (2005).

[132] A. Titov, X. Biquard, D. Halley, S. Kuroda, E. Bellet-Amalric, H. Mariette, J. Cibert, A. E. Merad, Merad, M. B. Kanoun, E. Kulatov, and Y. A. Uspenskii, *X-ray absorption near-edge structure and valence state of Mn in (Ga,Mn)N*, Phys. Rev. B **72**, 115209 (2005).

[133] J. Gosk, M. Zajac, A. Wolos, K. Kaminska, A. Twardowski, I. Grzegory, M. Bockowski, and S. Porowski, *Magnetic anisotropy of bulk GaN:Mn single crystals codoped with Mg acceptors*, Phys. Rev. B **71**, 094432 (2005).

[134] N. Syrbu, I. Tiginyanu, V. Ursaki, V. Zalamai, V. Popa, S. Hubbard, and D. Pavlidis, *Free Excitons in Strained MOCVD-Grown GaN Layers*, MRS Internet J. Nitride Semicond. Res. **8**, 1 (2003).

[135] A. Golnik, W. Mac, K. Pakula, R. Stepniewski, C. Testelin, and J. Gaj, *Low field excitonic Zeeman splittings in gallium nitride*, Solid State Commun. **124**, 89 (2002).

[136] A. V. Komarov, V. I. Sugakov, G. V. Vertsimakha, W. Zaleszczyk, G. Karczewski, and T. Wojtowicz, *Magnetic field dependence of exciton linewidth in quantum wells made of semimagnetic semiconductors : comparison of theory and experiment*, J. Phys. : Condens. Matter **18**, 7401 (2006).

[137] P. Kacman, *Spin interactions in diluted magnetic semiconductors and magnetic semiconductor structures*, Semicond. Sci. Technol. **16**, R25 (2001).

[138] J. A. Gaj, *Diluted Magnetic Semiconductors* (Institute of Experimental Physics, Warsaw University, Warsaw and Linz, 1999).

[139] A. Twardowski, P. Swiderski, M. von Ortenberg, and R. Pauthenet, *Magnetoabsorption and Magnetization of* $Zn_{1-x}Mn_xTe$ *Mixed Crystals*, Solid State Commun. **50**, 509 (1984).

[140] A. Twardowski, P. Swiderski, M. von Ortenberg, and R. Pauthenet, *Magnetization and Exchange Constants in* $Zn_{1-x}Mn_xSe$, Solid State Commun. **51**, 849 (1984).

[141] C. Testelin, C. Rigaux, A. Mycielski, M. Menant, and M. Guillot, *Exchange interactions in CdFeTe semimagnetic semiconductors*, Solid State Commun. **78**, 659 (1991).

[142] D. Scalbert, M. Guillot, A. Mauger, J. A. Gaj, J. Cernogora, C. Benoit à la Guillaume, and A. Mycielski, *High field magnetization and exchange integrals in* $Cd_{1-x}Fe_xSe$, Solid State Commun. **76**, 977 (1990).

[143] C. Testelin, J. B. Prost, M. Menant, M. Zielinski, and A. Mycielski, *Magnetization and exchange interactions in* $Zn_{1-x}Fe_xTe$ *diluted magnetic semiconductors*, Solid State Commun. **113**, 695 (2000).

[144] H. Alawadhi, I. Miotkowski, V. Souw, M. McElfresh, A. K. Ramdas, and S. Miotkowska, *Excitonic Zeeman effect in the zinc-blende II-VI diluted magnetic semiconductors* $Cd_{1-x}Y_xTe$ *(Y = Mn, Co, and Fe)*, Phys. Rev. B **63**, 155201 (2001).

[145] M. Zielinski, C. Rigaux, A. Lemaître, A. Mycielski, and J. Deportes, *Exchange interactions and magnetism of* Co^{2+} *in* $Zn_{1-x}Co_xTe$, Phys. Rev. B **53**, 674 (1996).

[146] X. Liu, A. Petrou, B. T. Jonker, J. J. Krebs, G. A. Prinz, and J. Warnock, *Magnetoreflectivity study of excitons in ZnCoSe*, J. Appl. Phys. **67**, 4796 (1990).

[147] W. Mac, A. Twardowski, and M. Demianiuk, *s,p-d exchange interaction in Cr-based diluted magnetic semiconductors*, Phys. Rev. B **54**, 5528 (1996).

[148] R. C. Myers, M. Poggio, N. P. Stern, A. C. Gossard, and D. D. Awschalom, *Antiferromagnetic s-d Exchange Coupling in GaMnAs*, Phys. Rev. Lett. **95**, 017204 (2005).

[149] J. Szczytko, W. Mac, A. Twardowski, F. Matsukura, and H. Ohno, *Antiferromagnetic* $p-d$ *exchange in ferromagnetic* $Ga_{1-x}Mn_xAs$ *epilayers*, Phys. Rev. B **59**, 12935 (1999).

[150] R. Lang, A. Winter, H. Pascher, H. Krenn, X. Liu, and J. K. Furdyna, *Polar Kerr effect studies of* $Ga_{1-x}Mn_xAs$ *epitaxial films*, Phys. Rev. B **72**, 024430 (2005).

[151] B. E. Larson, K. C. Hass, H. Ehrenreich, and A. E. Carlsson, *Theory of exchange interactions and chemical trends in diluted magnetic semiconductors*, Phys. Rev. B **37**, 4137 (1988).

[152] J. R. Schrieffer and P. A. Wolff, *Relation between the Anderson and Kondo Hamiltonians*, Phys. Rev. **149**, 491 (1966).

[153] J. R. Schrieffer, *The Kondo Effect—The Link Between Magnetic and Nonmagnetic Impurities in Metals ?*, J. Appl. Phys. **38**, 1143 (1967).

[154] A. K. Bhattacharjee, *Interaction between band electrons and transition-metal ions in diluted magnetic semiconductors*, Phys. Rev. B **46**, 5266 (1992).

[155] J. Blinowski and P. Kacman, *Kinetic exchange in diluted magnetic semiconductors*, Phys. Rev. B **46**, 12298 (1992).

[156] T. Mizokawa and A. Fujimori, $p-d$ *exchange interaction for* 3*d transition-metal impurities in II-VI semiconductors*, Phys. Rev. B **56**, 6669 (1997).

[157] T. Graf, S. T. B. Goennenwein, and M. S. Brandt, *Prospects for Carrier-Mediated Ferromagnetism in GaN*, Phys. Status Solidi B **239**, 277 (2003).

[158] T. Mizokawa and A. Fujimori, *Configuration-interaction description of transition-metal impurities in II-VI semiconductors*, Phys. Rev. B **48**, 14150 (1993).

[159] J. Okabayashi, A. Kimura, O. Rader, T. Mizokawa, A. Fujimori, T. Hayashi, and M. Tanaka, *Core-level photoemission study of* $Ga_{1-x}Mn_xAs$, Phys. Rev. B **58**, R4211 (1998).

[160] J. Okabayashi, T. Mizokawa, D. D. Sarma, A. Fujimori, T. Slupinski, A. Oiwa, and H. Munekata, *Electronic structure of* $In_{1-x}Mn_xAs$ *studied by photoemission spectroscopy : Comparison with* $Ga_{1-x}Mn_xAs$, Phys. Rev. B **65**, 161203 (2002).

[161] W. Shan, W. Walukiewicz, J. W. Ager, E. E. Haller, J. F. Geisz, D. J. Friedman, J. M. Olson, and S. R. Kurtz, *Band Anticrossing in GaInNAs Alloys*, Phys. Rev. Lett. **82**, 1221 (1999).

[162] P. J. Klar, H. Grüning, W. Heimbrodt, J. Koch, F. Höhnsdorf, W. Stolz, P. M. A. Vicente, and J. Camassel, *From N isoelectronic impurities to N-induced bands in the* GaN_xAs_{1-x} *alloy*, Appl. Phys. Lett. **76**, 3439 (2000).

Résumé

Ce travail porte sur la spectroscopie magnéto-optique de semi-conducteurs magnétiques dilués (DMS) : ZnO et GaN dopés manganèse, fer et cobalt. Par rapport aux semiconducteurs plus usuels du domaine (GaAs, CdTe...), es deux semi-conducteurs hôtes, ZnO et GaN, ont une grande bande interdite, une structure wurtzite, une faible interaction spin - orbite et une forte interaction d'échange excitonique entre trous et électrons. En présence de champ magnétique, les ions magnétiques induisent un effet Zeeman géant dont l'interprétation est complexe : les excitons s'anti-croisent et leurs énergies de transition et leurs forces d'oscillateur sont fortement influencées par l'effet Zeeman géant. On a mesuré expérimentalement le splitting Zeeman géant des excitons A et B, sur des couches epitaxiées sur saphir (0001) et avec une propagation de la lumière parallèle a l'axe c du cristal et au champ magnétique (configuration Faraday). Le splitting Zeeman géant diminue avec la température et augmente non linéairement avec le champ magnétique, en accord avec l'aimantation calculée des spins isolés. Une analyse quantitative nous a permis d'analyser les propriétés magnétiques et de mesurer les intégrales d'échange pour l'ensemble des matériaux étudiés. Pour des ions avec une configuration d^5 (Mn^{2+} et Fe^{3+}), l'aimantation suit une fonction de Brillouin $B_{5/2}$, mais pour les configurations d^7 et d^4 (Co^{2+} ou Mn^{3+}) l'interaction spin-orbite et le champ cristallin trigonal induisent une aimantation anisotrope, en accord avec l'analyse des transitions internes des ions mesurées en spectroscopie infrarouge. Pour $Ga_{1-x}Mn_xN$ et $Ga_{1-x}Fe_xN$, nous avons trouvé un signe positif pour l'intégrale d'échange entre trous et spins localisés (β). Dans ZnO, le signe du couplage spin-orbite qui définit la structure de la bande de valence, a été longtemps débattu. En supposant une symétrie de la bande de valence correspondant à une interaction spin-orbite Δ_2 positive (Γ_9, Γ_7, Γ_7), nous trouvons un signe négatif de β pour $Zn_{1-x}Co_xO$ et β est proche de zéro pour $Zn_{1-x}Mn_xO$. Toutefois, dans l'hypothèse d'un couplage spin-orbite Δ_2 négatif, nous trouvons un signe positif de β. Les signes et les valeurs des intégrales d'échange déterminés par nos mesures magnéto-optiques nes suivent pas la tendance générale des DMS et ne peuvent pas être expliqués par les modèles basés sur l'approximation du cristal virtuel. Ceci suggère que l'échange *p-d* dans les DMS à large bande interdite, est dans un régime de couplage fort, si bien que la nature du splitting Zeeman géant observé est différente de celle des semi-conducteurs magnétiques dilués classiques.

Mots-clés: Semi-conducteur magnétique dilué, semi-conducteur à large bande interdite, électronique de spin, spectroscopie magnéto-optique, exciton, interaction échange, effet Zeeman géant, ZnO, GaN, manganese, fer, cobalt.

Abstract

This work presents a magnetooptical study of diluted magnetic semiconductors (DMS) based on ZnO and GaN, doped with manganese, iron, and cobalt. Both host materials, ZnO and GaN, are wide band gap semiconductors with a wurtzite structure, a weak spin-orbit coupling and a strong electron-hole exchange interaction within the excitons. In the presence of a magnetic field, the magnetic ions induce in such materials a giant Zeeman effect with a complex behavior : excitons anti-cross, and not only the transition energies, but also the oscillator strengths are strongly affected by the giant Zeeman effect. On thin epitaxial layers grown on (0001) sapphire, we observed the giant Zeeman splitting of the A and B excitons, which are optically active in the Faraday configuration when the propagating light is parallel to the c-axis. The Zeeman splitting decreases with the temperature and increases non-linearly with the magnetic field, demonstrating a dependence on the magnetization of the localized spins. A quantitative analysis allows us to discuss the detailed behavior of the magnetization and to estimate the *p-d* exchange integral β for the studied wide bandgap DMS. For the d^5 electronic configuration (Mn^{2+} and Fe^{3+}) the magnetization follows a Brillouin function $B_{5/2}$, whereas, for d^7 or d^4 of Co^{2+} and Mn^{3+} respectively, the spin orbit coupling and the trigonal crystal field lead to an anisotropic magnetization, consistent with that deduced independently from the analysis of intra-ionic optical transitions. We find a positive sign of β for $Ga_{1-x}Mn_xN$ and $Ga_{1-x}Fe_xN$. In ZnO, the sign of the spin-orbit interaction, which determines the structure of the valence band, has been a matter of debate. Assuming that the valence band ordering in ZnO is Γ_9, Γ_7, Γ_7 (this corresponds to usual, positive sign of the spin-orbit coupling), we find β to be negative for $Zn_{1-x}Co_xO$ and to be close to zero in $Zn_{1-x}Mn_xO$. However, assuming the reversed valence band ordering, we find β to be positive in both ZnO based DMS. The sign and the value of *p-d* exchange integrals determined from our magnetooptical measurements do not follow material trends in DMS and cannot be explained by models based on the virtual crystal approximation. This suggests that the *p-d* coupling in wide gap DMS is in the strong coupling regime, so that the nature of the observed giant Zeeman splitting is different from that in classical diluted magnetic semiconductors.

Keywords: Diluted magnetic semiconductor, wide band gap semiconductor, spintronics, magnetooptical spectroscopy, exciton, exchange interaction, giant Zeeman effect, ZnO, GaN, manganese, iron, cobalt.